1995

Experimental and analytical investigation of the bubble nucleation characteristics in subcooled flow

Michael D. Cartwright

Recommended Citation

Cartwright, Michael D., "Experimental and analytical investigation of the bubble nucleation characteristics in subcooled flow" (1995). Thesis. Rochester Institute of Technology. Accessed from

"Experimental and Analytical Investigation
of the
Bubble Nucleation Characteristics in Subcooled Flow"

by

Michael D. Cartwright

A Thesis Submitted
in
Partial Fulfillment
of the
Requirements for the

MASTER OF SCIENCE

in

Mechanical Engineering

Approved by:

Professor Glaudia Pavi
Thesis Advisor

Professor R. J. Hefner

Professor Alan Nye

Professor Charles W. Harris
Department Head

DEPARTMENT OF MECHANICAL ENGINEERING
COLLEGE OF ENGINEERING
ROCHESTER INSTITUTE OF TECHNOLOGY
JUNE 1995

PERMISSION TO REPRODUCE:

Thesis Title: "Experimental and Analytical Investigation of the Bubble Nucleation Characteristics in Subcooled Flow"

I, Michael Cartwright, hereby grant permission to the Wallace Memorial Library, of the Rochester Institute of Technology to reproduce my thesis in whole or part. Any reproduction can not be used for commercial use or profit.

June 5, 1995

FORWARD:

I would like to express my appreciation and thanks to the following people: Wendi for her patience and understanding over the past year when I couldn't always be there for her, Viktor "God" Mizo for all of the help and cooperation he has given me over the past few months, Dr. Kandlikar for all of the guidance, and support I have received from him, Tom Locke for his time, and patience during the test section refinements, Andy Hayes for all of the time he spent teaching me how to use just about every piece of equipment in the Thermo Lab, at least twice, Todd Geib and Joe Scippo for their time and help on the ThermoNet model, and a special thanks to my mom for the support, encouragement, and everything else she has done for me over the past five years, I couldn't have done it without her.

ABSTRACT:

An experimental and analytical study of bubble nucleation characteristics for a polished aluminum surface under subcooled flow boiling of water is conducted. A high magnification (up to 1350X) microscope and an atomic force magnifier were used to visualize the aluminum surface to determine a range of cavity sizes on the heater surface as well as gain insight into the shape of the cavity. A high-speed camera was incorporated to study the actual bubble nucleation from these cavities.

A review of existing theoretical models available in literature to predict bubble nucleation characteristics in flow boiling is also presented. A new bubble nucleation model is proposed which uses experimentally determined bubble geometry and results from computational fluid dynamics (CFD) modeling.

Experimental data was collected through the use of the high-speed flow visualization system available in RIT's Thermal Fluid Laboratory. The data is obtained to study the effects of subcooling, flow rate, and wall superheat on the nucleation characteristics of different size cavities. This data is also compared with existing models as well as the one proposed in this investigation.

TABLE OF CONTENTS

LIST OF FIGURES:

LIST OF TABLES:

NOMENCLATURE:

A_{lv} - liquid-vapor surface area

A_{sl} - solid-liquid surface area

A_{sv} - solid-vapor surface area

b - bubble height

D_h - hydraulic diameter of flow channel, 4WH/2(W + H)

g - specific Gibbs function

h - convective heat transfer coefficient

h_{lv} - latent heat of vaporization per unit mass

H - height of flow channel

k - thermal conductivity

m - mass

m_l - mass of liquid

m_v - mass of vapor

m_T - total mass of system

P - Pressure

q - total heat transfer

r - radius

r_b - bubble radius

r_c - cavity radius

r_{crit} - critical cavity radius

r_e - bubble radius at a equilibrium state

r_{min} - minimum cavity radius required for nucleation

r_{max} - maximum cavity radius required for nucleation

R - cavity mouth radius

R - ideal gas constant on a per unit mass basis

Re - Reynolds number, $\rho u_m D_h/\mu_l$

Re_D . Reynolds number for flow in a circular tube

s - specific entropy

T - temperature

T_{BULK}- bulk water temperature

T_{SAT} - saturation temperature

T_{SURF}- surface temperature

Tw - wall temperature

u_m - mean velocity in flow channel

U - internal energy

ν - specific volume

V - volume

y_s - height of stagnation streamline

Greek Letters

α - thermal diffusivity

β - bubble contact angle

δ_t - thermal boundary layer

$\Delta\psi$ - change in system availability

γ - one half the idealized cavity cone angle

μ - viscosity

μ - chemical potential

μ_{ve} - vapor chemical potential at equilibrium state

θ_a - contact angle of advancing liquid

θ - angular elevation from the horizontal axis passing through the center of the bubble

θ - liquid contact angle

ρ - density

σ - interfacial tension

σ_{lv} - liquid-vapor interfacial tension

σ_{sl} - solid-liquid interfacial tension

ψ - availability function/available free energy

ψ_o - initial availability of a system

ψ_i - interface availability

ψ_l - liquid availability

ψ_v - vapor bubble availability

Subscripts

a - advancing

BULK - bulk of liquid

COND - conduction

CONV - convection

e - equilibrium state

g - gas

l - liquid

ONB - onset of nucleate boiling

s - stagnation

SAT - saturation

SURF - surface

v - vapor

w - wall

1. INTRODUCTION:

Nucleate flow boiling plays a vital role in many of today's technological applications. The current trend of most electronic equipment manufactures is to get as much circuitry in as small of a package as possible. This trend has lead to many problems related to the cooling of the more compact circuitry, and has brought about a need to find new techniques in which to remove heat generated from confined spaces. The high heat transfer coefficient associated with nucleate flow boiling has made its use increasingly attractive in the thermal control of such devices. Nucleate flow boiling also has two important applications in the nuclear power industry. The first being the primary means of transporting heat given off by the reactor core to the steam lines which feed the power producing steam turbines. The second application of nucleate boiling is using it as an integral part of accident scenarios requiring rapid cooling of reactor cores.

It is now well known that nucleate boiling is initiated over pre-existing cavities. When the proper thermal conditions are met, these cavities are nucleated. In the case of a superimposed flow, the fluid motion alters the thermal characteristics in the region surrounding the cavities. The work presented in this thesis focuses on the nucleation characteristics of cavities under subcooled flow conditions. The study includes a theoretical model development and its confirmation using experimental data obtained in the course of the investigation.

2. OBJECTIVE OF CURRENT STUDIES:

The objective of the current work is to obtain a better understanding of the nucleation characteristics of a polished aluminum surface subjected to flowing subcooled water near atmospheric conditions. Specifically the following issues will be addressed.

- Conduct a review of literature to obtain a better understanding of the nucleation characteristics in pool boiling.
- Review the existing literature on models used for predicting bubble nucleation characteristics in flow boiling.
- Complete a detailed study of the heater surface attributes using both a high magnification microscope and atomic force magnifier.
- Propose a new model for nucleation under flow boiling conditions considering the correct bubble shape (truncated sphere) and results from CFD analysis.
- Obtain experimental data to study the initiation of nucleation as a function of cavity radius, degree of subcooling, and flow velocity.
- Validate the proposed model using experimental data.

3. LITERATURE REVIEW:

The objective of this section is two fold, the first is to initially develop a basic understanding of the bubble nucleation process, and the second is, to review the existing models from literature used to predict the size range of active nucleation sites.

3.1 Bubble Embryo Stability Criteria

Bubble formation, or nucleation can be classified into two separate categories, homogeneous and heterogeneous nucleation. Homogeneous is when a bubble nucleation occurs completely within a liquid as shown in Fig. 3.1. Heterogeneous is nucleation at an interface between a metastable phase (non-equilibrium condition where vapor is supercooled below its equilibrium saturation temperature or liquid is superheated above its equilibrium saturation temperature) and another, usually solid, phase that it contacts. Since the work included in this paper deals solely with heterogeneous nucleation, only the heterogeneous nucleation process will be discussed in detail.

Fig. 3.2 shows a system in which a truncated bubble embryo has grown on the lower surface of the chamber. Fig. 3.3 shows an embryo at an idealized liquid-solid interface with the vapor volume, the solid-vapor surface area and the liquid-vapor surface area defined as:

$$V_v = \frac{\pi r^3}{3}\left(2 + 3\cos\theta - \cos^3\theta\right) \tag{3.1}$$

$$A_{lv} = 2\pi r^2 (1 + \cos\theta) \tag{3.2}$$

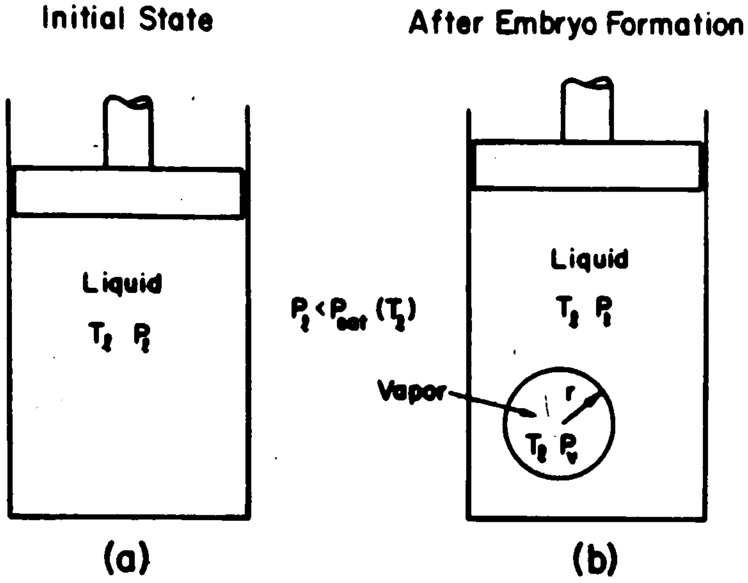

Figure 3.1 System model considered in the thermodynamic analysis of an embryo bubble formation by homogeneous nucleation.

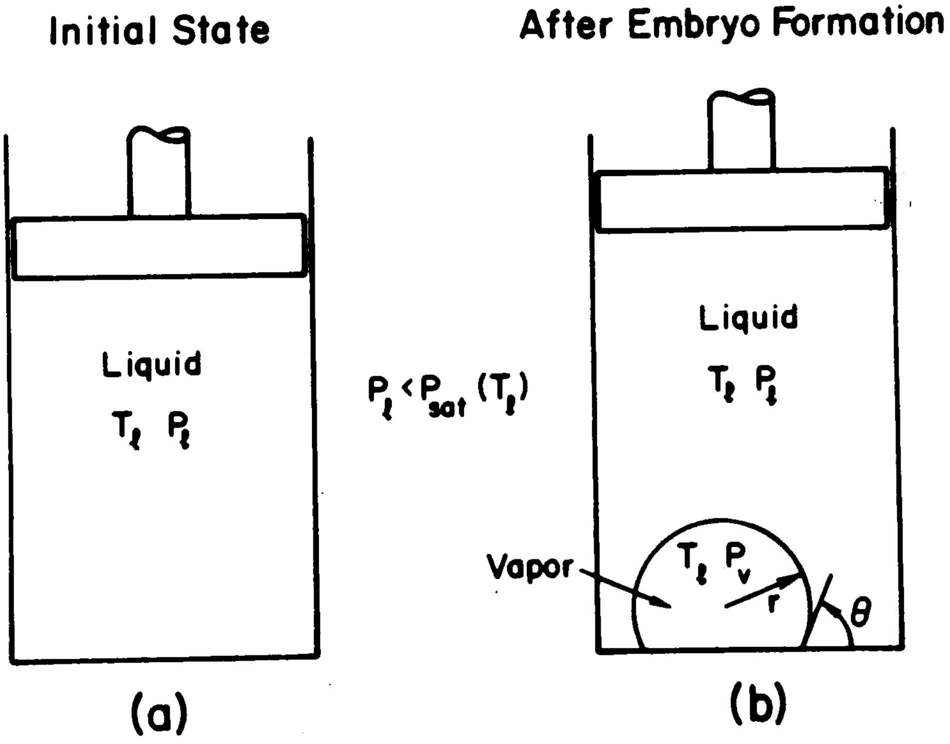

Figure 3.2 System model considered in the thermodynamic analysis of an embryo bubble formation by heterogeneous nucleation.

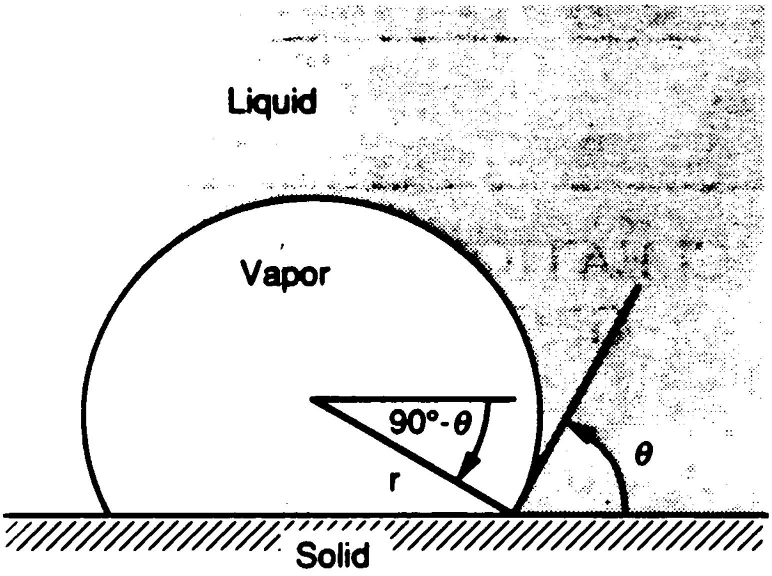

Figure 3.3 An embryo vapor bubble formed at an idealized liquid-solid interface.

$$A_{sv} = 2\pi r^2(1-\cos\theta) \tag{3.3}$$

where θ is the contact angle and r is the spherical cap radius. In order to determine whether the embryo is stable or unstable, and if unstable whether it will collapse or grow, we consider the bubble embryo shown in Fig. 3.2.

At equilibrium saturation conditions the temperature of the vapor and liquid must be the same, and the chemical potential in the two phases must also be equal.

$$\mu_l = \mu_{ve} \tag{3.4}$$

Through the use of the Young-Laplace equation:

$$P_v = P_l + \frac{2\sigma}{r_e} \tag{3.5}$$

it can be seen that the pressure in the vapor bubble will be higher due to the curvature and surface tension. Integrating the Gibbs-Duhem equation

$$d\mu = -sdT + vdP$$

for the vapor at a constant temperature from $P = P_{SAT}(T_l)$ to a pressure P_{ve} and using the ideal gas law ($v = RT_l/P$) gives:

$$\mu_{lv} = \mu_{SAT,v} + RT_l \ln\left[\frac{P_{ve}}{P_{SAT}(T_l)}\right] \tag{3.6}$$

For the liquid phase, since the liquid is virtually incompressible, v is taken to be constant and equal to the value for saturated liquid at T_l, $v = v_l$. Evaluation of the integral from P_{SAT} to P_l yields.

$$\mu_l = \mu_{SAT,l} + v_l[P_l - P_{SAT}(T_l)] \tag{3.7}$$

Substituting Eqs. (3.6) and (3.7) into (3.4) and using the fact that $\mu_{SAT,v} = \mu_{SAT,l}$, the following relation can be derived.

$$P_{ve} = P_{SAT}(T_l)\exp\left\{\frac{v_l\left[P_l - P_{SAT}(T_l)\right]}{RT_l}\right\} \qquad (3.8)$$

Substituting the above equation into Eq. (3.5) results in an equation for the critical bubble radius, r_e that will support a bubble in equilibrium with the surrounding superheated liquid at temperature T_l and pressure P_l.

$$r_e = \frac{2\sigma}{P_{SAT}(T_l)\exp\left\{\frac{v_l\left[P_l - P_{SAT}(T_l)\right]}{RT_l}\right\} - P_l} \qquad (3.9)$$

From Eqs (3.6) and (3.8) the equilibrium pressure can be approximated by:

$$P_{ve} = P_{SAT}(T_l)\exp\left\{\frac{-2v_l\rho}{r_e RT_l}\right\} \qquad (3.10)$$

The conditions necessary for a bubble embryo to be in equilibrium have now been defined, the next step will be to determine whether the embryo can attain a stable equilibrium. In order to determine the stability of the system shown Fig. 3.2, the availability function ψ for the system must be considered.

$$\psi = U - T_l s + P_l v \qquad (3.11)$$

ψ is usually associated with the maximum (reversible) work that can be extracted from the system to bring it entirely to an equilibrium reference state at P_l and T_l. Through basic thermodynamic consideration, bubble equilibrium requires that $d\psi = 0$, and ψ must be a minimum for stable equilibrium. Prior to embryo formation the availability of supersaturated liquid is:

$$\psi_o = (m_l + m_v)g_l(T_l, P_l) \qquad (3.12)$$

Upon completion of the embryo formation the total availability will be the sum of the vapor bubble, liquid and interfacial availability

$$\psi = \psi_v + \psi_l + \psi_i \tag{3.13}$$

where the three terms on the right are defined as:

$$\psi_l = (m_T - m_v)g_l(T_l,P_l) \tag{3.14}$$

$$\psi_v = m_v[g_v(T_l,P_v)+(P_l - P_v)v_v \tag{3.15}$$

$$\psi_i = \sigma_{lv} + \sigma_{sv}A_{sv} + (A_{sl})_f\sigma_{sl} \tag{3.16}$$

Combining Eqs. (3.12) through (3.16) with (3.2) and (3.3), using the fact that

$$(A_{sl})_i-(A_{sl})_f = A_{sv} \tag{3.17}$$

and Young's equation (resulting from a force balance along the interline),

$$\sigma_{sv} - \sigma_{sl} = \sigma_{lv}\cos\theta \tag{3.18}$$

the following equation relating the change of system availability $\Delta\psi$ during the formation of the embryo can be defined:

$$\begin{aligned}\Delta\psi = \psi - \psi_o &= m_v\left[g_v(T_l,P_v) - gl(T_l,P_v)\right] + (P_l - P_v)V_v \\ &+4\pi r^2\sigma_{lv}\left[\frac{1}{2}(1+\cos\theta) + \frac{1}{4}\cos\theta\left(1-\cos^2\theta\right)\right]\end{aligned} \tag{3.19}$$

For the equilibrium condition where $r = r_e$ Eq. (3.19) reduces to:

$$\Delta\psi_e = \frac{4}{3}\pi r_e^2\sigma_{lv}\left[\frac{1}{2} + \frac{3}{4}\cos\theta - \frac{1}{4}\cos^3\theta\right] \tag{3.20}$$

Eq (3.20) can then be used to derive the following Taylor series expansion for $\Delta\psi$ about the equilibrium condition $r = r_e$.

$$\Delta\psi = \frac{4}{3}\pi r_e^2\sigma_{lv}F - \left(\frac{4\pi\sigma_{lv}F}{3}\right)\left(2 + \frac{P_l}{P_{ve}}\right)\left(r - r_e\right)^2 + \ldots \tag{3.21}$$

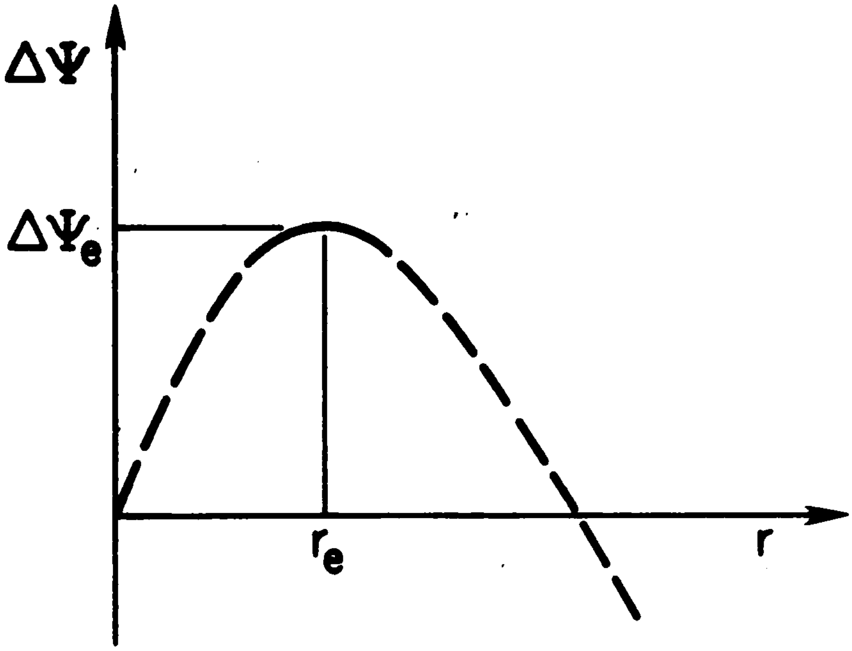

Figure 3.4 Variation of the system availability with bubble radius for a vapor bubble spontaneously formed at a solid-liquid interface.

where

$$F = F(\theta) = \frac{2 + 3\cos\theta - \cos^3\theta}{4} \tag{3.22}$$

A plot of $\Delta\psi$ from Eq. (3.21) versus radius r is shown in Fig. 3.4 on the previous page. As can be seen from this plot a maximum occurs at $r = r_e$, since $\Delta\psi$ must be at a minimum for stable equilibrium, it is clear that at equilibrium conditions the embryo is unstable. Thus, if an embryo is formed in a metastable liquid with $r < r_e$, the bubble will most likely collapse. However, if $r > r_e$, it will spontaneously grow.

3.2 Vapor Entrapment

For homogeneous nucleation the same analysis as described in section 3.1 can be completed. The results will be almost the same as Eq (3.22), only $\Delta\psi$ will no longer be dependent on F, a resultant of the embryo contact angle:

$$\Delta\psi = \frac{4}{3}\pi r_e^2 \sigma_{lv} - \left(\frac{4\pi\sigma_{lv}}{3}\right)\left(2 + \frac{P_l}{P_{ve}}\right)(r - r_e)^2 + \ldots \tag{3.23}$$

From both experimental testing and Eq (3.23) the superheat required for homogeneous nucleation at atmospheric conditions is observed to be often extremely high. However, since the heterogeneous model is independent of the contact angle, lower required superheat could be achieved. For a liquid which completely wets the surface ($\theta = 0°$), F = 1 and no reduction in availability is achieved. If the surface is completely non-wetting ($\theta = 180°$) then F = 0, which would suggest that the required superheat for nucleation is zero. For most solid-liquid systems θ lies in the range of 0° to 90°, corresponding to values of F in the range of 1.0 to 0.5. Although this reduces the required superheat, it is still not enough to explain for the significantly lower superheat found in practical situations as compared with those required in homogeneous nucleation. For example, the analysis completed in section 3.1 would suggest wall superheat in the range of 300°C for boiling water in a metal pot. However, from experimental results it is known that superheats on the order of only 10-15°C are typically required. The reason for nucleation at these lower temperatures is due to the presence of trapped vapor found in cavities on the metal surface.

Unlike the smooth surface analysis described in the previous section, most real surfaces contain some cavities, crevices, scratches or other irregularities. If the surface is not completely wetted, vapor will be trapped in these cavities allowing for vaporization at relatively low temperatures. Bankoff (1958) described the relationship between contact angle and cone angle which determines whether or not vapor will be trapped. Fig. 3.5 illustrates Bankoff's theory on the entrapment of vapor for a liquid passing over a gas filled cavity.

For a liquid sheet passing over the cavity the contact angle with the downward slope tends to be maintained as the liquid begins to fill the cavity. As seen in Fig. 3.5, the liquid front will be convex, thus if the contact angle is greater then 2γ, the convex portion of the front will strike the opposite wall before the contact line reaches the bottom of the cavity. The conditions for entrapment of gas by the advancing liquid front can therefore be stated as:

$$\theta_a > 2\gamma \tag{3.24}$$

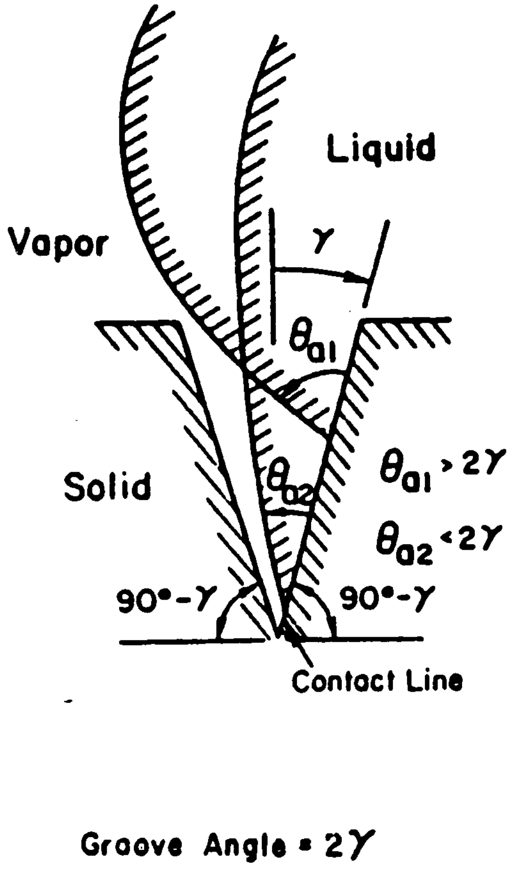

Figure 3.5 Schematic representation of vapor entrapment in a cavity due to the motion of a passing liquid front.

Now that the mechanisms leading to the entrapment of vapor have been defined it is important to understand how the entrapped vapor grows within the cavity. To do this the cavity will be idealized as conical with a mouth radius of R and cone angle of 2γ. The vapor embryo will also be idealized as portion of a sphere with a single radius of curvature, r. Fig. 3.6 illustrates the embryo growth for three separate ranges of contact angles. Fig. 3.6a corresponds to a highly wetting liquid ($\theta < \gamma < 90°$). In this case the embryo starts at a small value and continues to grow steadily as it leaves the mouth of the cavity. In general it will be unlikely to observe this situation because as stated previously, vapor entrapment does not occur unless $\theta > 2\gamma$.

For contact angles in the range of $2\gamma < \theta \leq 90°$, the radius r initially increases as it moves up the cavity to the mouth (Fig. 3.6b). Once the vapor interface leaves the mouth the radius decreases and then begins to increase again.

The third cavity range, $\theta > (90° + \gamma)$, is shown in Fig 3.6c. In this case the radius of curvature while inside the cavity is taken to be negative. As the interface approaches the mouth 1/r becomes smaller and R/r becomes less negative. Once the interface turns the corner at the mouth, the radius of curvature becomes positive and continues to grow. R/r eventually reaches a maximum and then begins to decrease towards zero. The qualitative variation of R/r verses embryo volume is shown in Fig 3.6d for all three cases.

From section 3.1 it is known that in order for an embryo to grow past its equilibrium size additional superheat must be added. Combining the information gained in section 3.1 with the Claysius-Clapeyron and Younge-Laplace equations while approximating P_{ve} -P_l as $P_{SAT}(T_l)$ - P_l, the conditions for the cavity to be active can be stated as

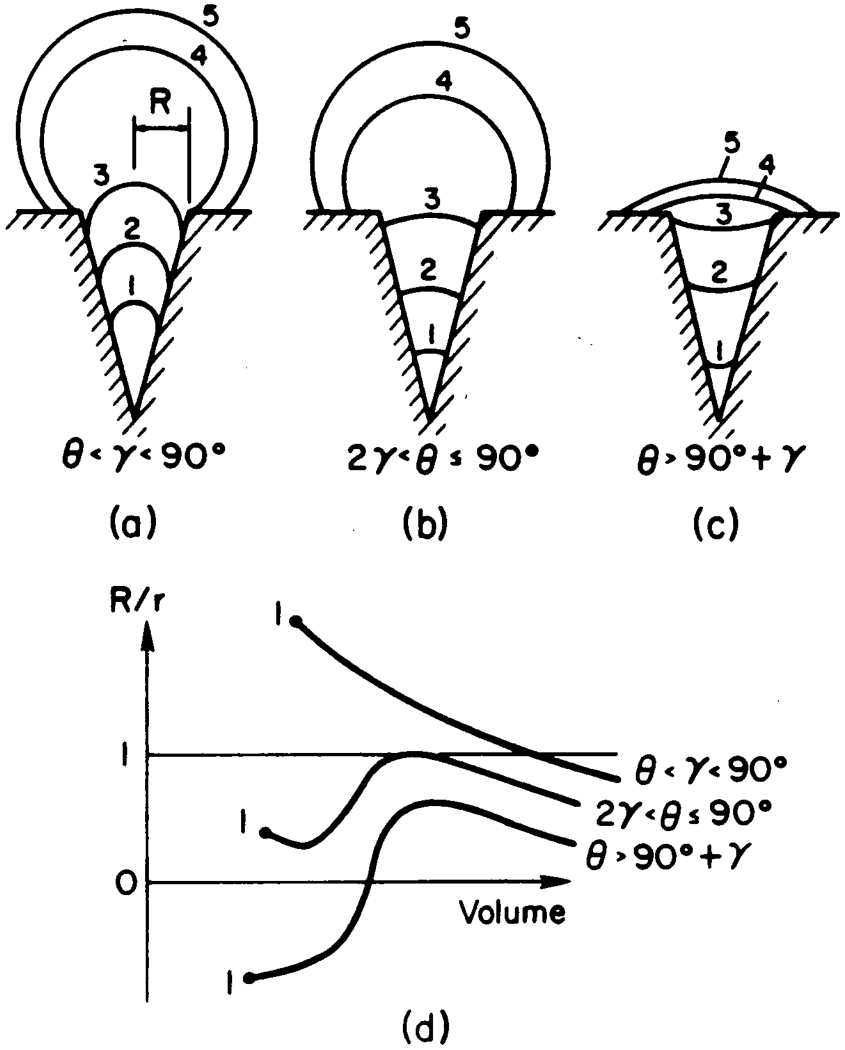

Figure 3.6 Variation of bubble radius as the bubble grows within and out of an idealized surface cavity.

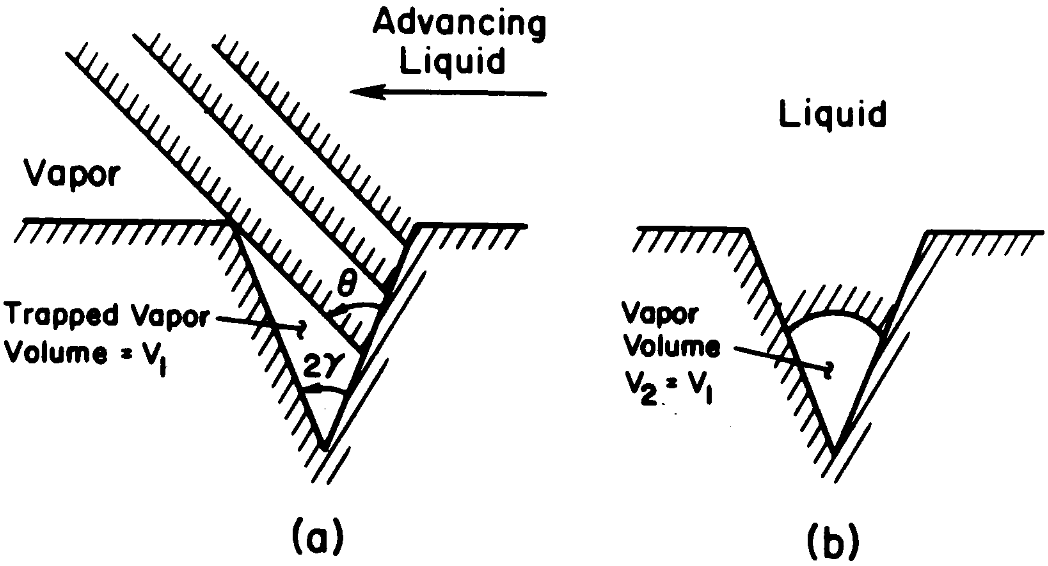

Figure 3.7 Idealized model of vapor trapping process used to estimate initial radius of embryo vapor bubble in a cavity.

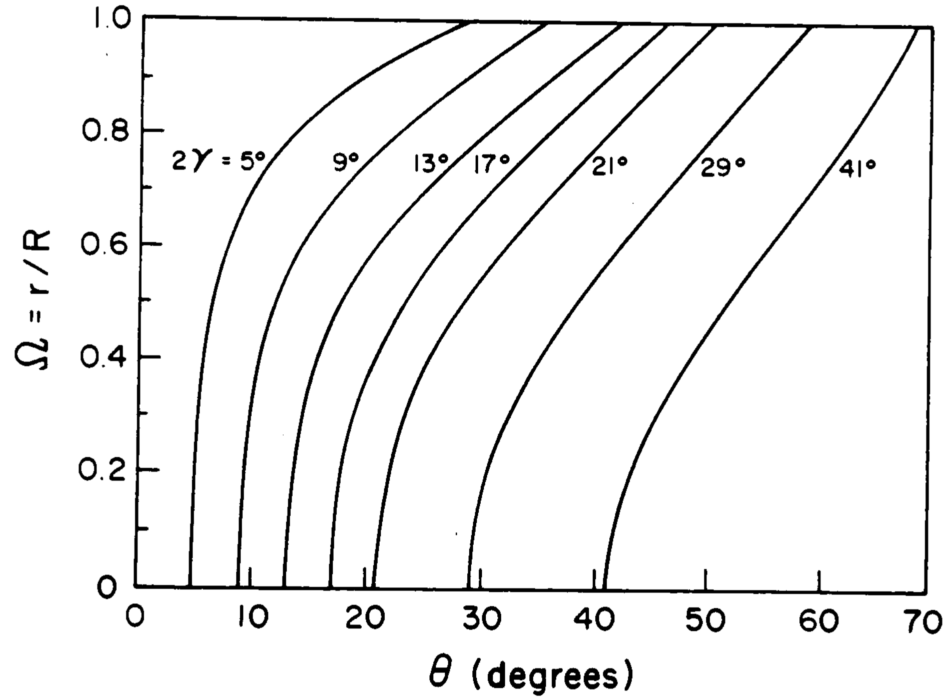

Figure 3.8 Variation of the initial radius of the vapor embryo with the cavity cone angle and contact angle as predicted by the model of Lorenz et al.(1974).

$$T_l - T_{SAT}(P_l) > \frac{2\sigma T_{SAT}(P_l) v_{lv}}{h_{lv} r_{\min}} \tag{3.25}$$

In many real systems $r_{\min}$ is the initial embryo size. A model to predict the initial radius has been developed by Lorenz et al. (1974). In this model a conical cavity of radius R and cone angle 2γ (Fig. 3.7) is considered. As shown in the figure, a flat liquid front passes over a cavity. The vapor volume V_1 initially trapped by the liquid front will be the same as the readjusted volume V_2 in Fig. 3.7b. The magnitude of r and hence r/R can be determined by geometry alone if θ and 2γ are known using Fig. 3.8. The condition for the site to be active can then be specified from Eq. 3.25 and r/R(θ,2γ) determined from Fig. 3.8.

$$T_{l_e} - T_{SAT}(P_l) > \frac{2\sigma T_{SAT}(P_l) \upsilon_{lv}}{h_{lv} R \frac{r}{R}(\theta, 2\gamma)} \qquad \text{for } R/r > 1 \tag{3.26}$$

3.3 Criteria for Onset of Nucleation

In the previous section when dealing with embryo growth, it has always been assumed that a uniform superheat temperature existed in the liquid surrounding the cavity. In real systems, particularly those dealing with subcooled flow, this is not true; instead, a thermal boundary layer exists between the surface and subcooled flow. A model proposed by Hsu (1962) provides considerable insight into the effects of subcooling, pressure, and physical properties in determining the size range of surface cavities that will be active.

The system considered in Hsu's model is shown in Fig. 3.9. In this model it was assumed that a truncated bubble is sitting at the mouth of the cavity. The bubble is

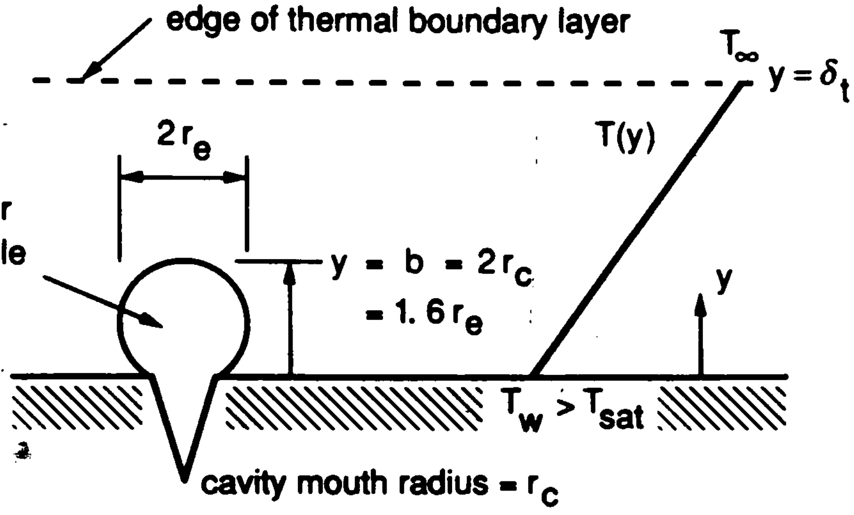

Figure 3.9 Representation of a bubble in Hsu's (1964) nucleation model.

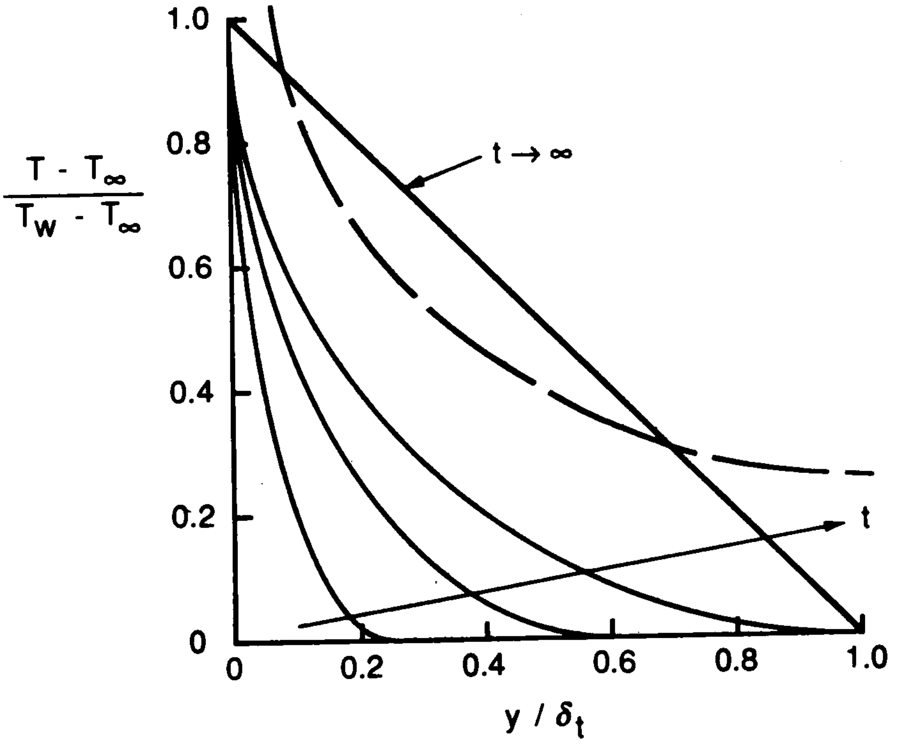

Figure 3.10 Transient temperature profile near surface.

assumed to be formed from the vapor left behind inside the cavity after the release of a preceding bubble. At the beginning of the bubble nucleation cycle, bulk liquid at a lower temperature replaces the void left by the departing bubble. Over time this liquid warms up through the transient-conduction process and the thermal boundary layer grows. The time elapsed between the release of two consecutive bubbles is defined as the waiting period.

However, because of the turbulence in the bulk fluid the boundary layer cannot grow indefinitely. Hsu (1962) suggested that beyond a certain limiting thickness, δ_t, eddy diffusivity would be so strong that the temperature would be held essentially at T_{BULK}. Assuming a constant surface temperature and thermal boundary layer thickness, a one-dimensional transient model for heat transfer from the wall to the liquid will have the following governing equation.

$$\frac{\partial\theta}{\partial t} = \alpha\frac{\partial^2\theta}{\partial y^2} \tag{3.27}$$

where $\theta = T - T_{BULK}$ and the boundary and initial conditions are

$$\theta = 0 \quad \text{at } t = 0 \tag{3.28}$$

$$\theta = 0 \quad \text{at } y = \delta_t \tag{3.29}$$

for t > 0,

$$\theta = \theta_w = T_w - T_{BULK} \quad \text{at } y = 0 \tag{3.30}$$

The solution for this differential equation is given by

$$\frac{\theta}{\theta_w} = \alpha\frac{\delta t - y}{\delta t} + \frac{2}{\pi}\sum_{n=1}^{\infty}\frac{\cos n\pi}{n}\sin\left[n\pi\left(\frac{\delta t - y}{\delta t}\right)\right]e^{-n^2\pi^2(\alpha_l t/\delta_l^2)} \tag{3.31}$$

The qualitative behavior of the temperature profile predicted by this solution is shown in Fig 3.10. At the limiting steady state conditions it can be seen that a linear profile is approached between the wall and $y = \delta_t$.

In Hsu's model, a simple relationship between bubble height b, the radius of the bubble embryo r_e, and the mouth radius r_c was assumed:

$$b = 2r_c = 1.6\, r_e \tag{3.32}$$

Hsu (1962) postulated that the criteria for nucleation from this cavity is that the temperature of the liquid surrounding the top of the bubble embryo should exceed that necessary for the embryo to remain in equilibrium (Eq. 3.25). A convenient way of representing this criterion is shown in Fig 3.11. If the line representing the liquid temperature profile intersects the equilibrium bubble curve then nucleation occurs. The first nucleation site to become active corresponds to the point of tangency between the equilibrium bubble curve and liquid temperature profile as shown on the graph. The wall temperature corresponding to this point is $(T_W)_{ONB}$. Once the wall temperature goes above $(T_W)_{ONB}$ the two points of intersection will correspond to the minimum and maximum range of active cavity sizes.

As previously done (Eq. 3.25) by combining the Clausius-Clapeyron and Young-Laplace equations, while assuming P_{le} - P_l as $P_{SAT}(T_l)$ - P_l, an equation relating the equilibrium superheat and bubble radius can be derived as

$$T_{le} - T_{SAT}(P_l) = \frac{2\sigma T_{SAT}(P_l)}{\rho_v h_{lv} r_e} \tag{3.33}$$

An equation for the values of $r_{c,min}$ and $r_{c,max}$ can be determined by using the steady state linear temperature profile

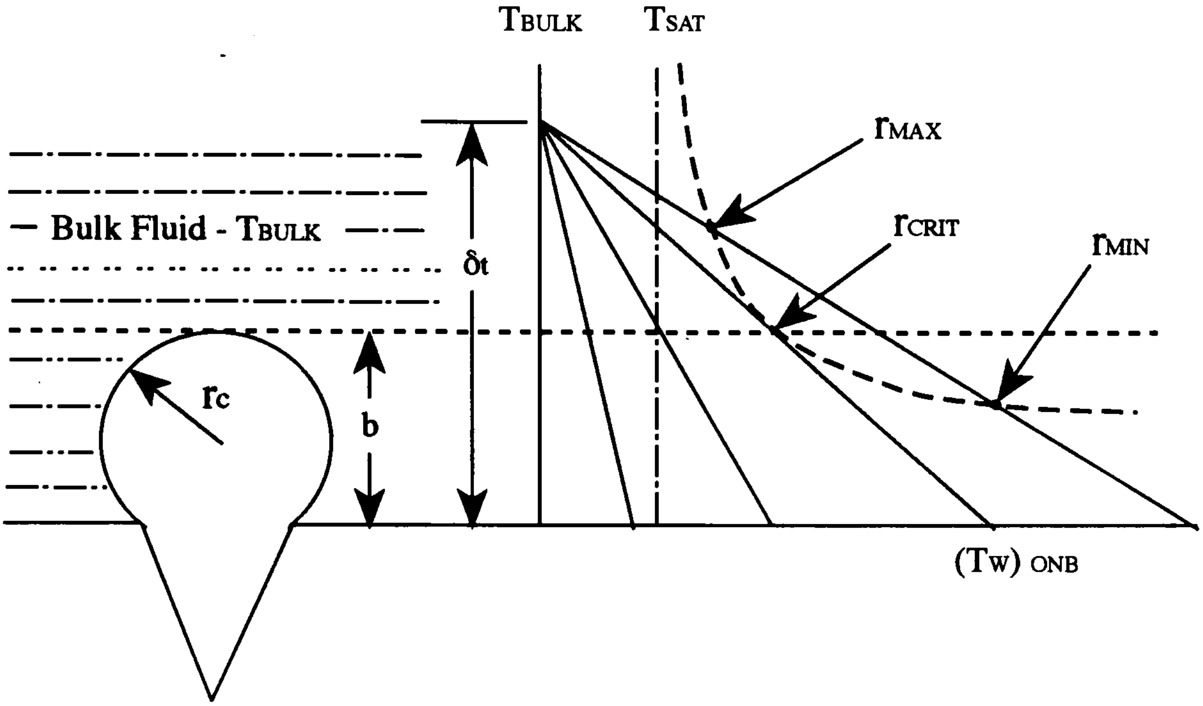

Figure 3.11 Criteria for the onset of nucleate boiling.

$$\theta = \theta_w - \frac{y}{\delta_t}\left(T_w - T_\infty\right) \tag{3.34}$$

and Eq. 3.33 rewritten as

$$\theta - \theta_{SAT} = \frac{2\sigma T_{SAT}(P_l)}{\rho_v h_{lv} r_c} \tag{3.35}$$

were $\theta = T_{le} - T_{BULK}$ and $\theta_{SAT} = T_{SAT}(P_l) - T_{BULK}$. Substituting Eq. (3.34) into (3.35) and setting y = b from Eq. (3.32) the following relationship can be found for the cavity radius

$$r_c^2 - \frac{\delta_t}{2}\left(1 - \frac{\theta_{SAT}}{\theta_w}\right) r_c + \frac{1.6\delta_t}{2}\left(\frac{\sigma T_{SAT}(P_l)}{\theta_w \rho_v h_{lv}}\right) = 0 \tag{3.36}$$

Hsu solved the above quadratic equation to find an equation for $r_{c,\min}$ and $r_{c,\max}$ as shown below in Eq. (3.37)

$$\left\{\begin{matrix} r_{c,\min} \\ r_{c,\max} \end{matrix}\right\} = \frac{\delta_t}{4}\left[\left(1 - \frac{\theta_{SAT}}{\theta_w}\right) \mp \sqrt{\left(1 - \frac{\theta_{SAT}}{\theta_w}\right)^2 - \frac{12.8\sigma T_{SAT}(P_l)}{\theta_w \rho_v h_{lv} \delta_t}}\right] \tag{3.37}$$

Another model was postulated by Bergles and Rohsenow (1964) in which a hemispherical bubble (Fig. 3.12) was used. In this case the height of the bubble, b, was assumed to be simply the radius of the cavity r_c. Substituting this into Eq. (3.34) and (3.35) the equation for $r_{c,\min}$ and $r_{c,\max}$ is

$$\left\{\begin{matrix} r_{c,\min} \\ r_{c,\max} \end{matrix}\right\} = \frac{\delta_t}{2}\left[\left(1 - \frac{\theta_{SAT}}{\theta_w}\right) \mp \sqrt{\left(1 - \frac{\theta_{SAT}}{\theta_w}\right)^2 - \frac{8\sigma T_{SAT}(P_l)}{\theta_w \rho_v h_{lv} \delta_t}}\right] \tag{3.38}$$

Davis and Anderson (1966) suggested a slightly different model. Instead of assuming the bubble height to be proportional to the cavity radius as in both of the previous models (Hsu, and Bergles and Rohsenow), they assumed that the bubble was a truncated sphere with contact angle as shown in Fig 3.13. In this case b is defined as

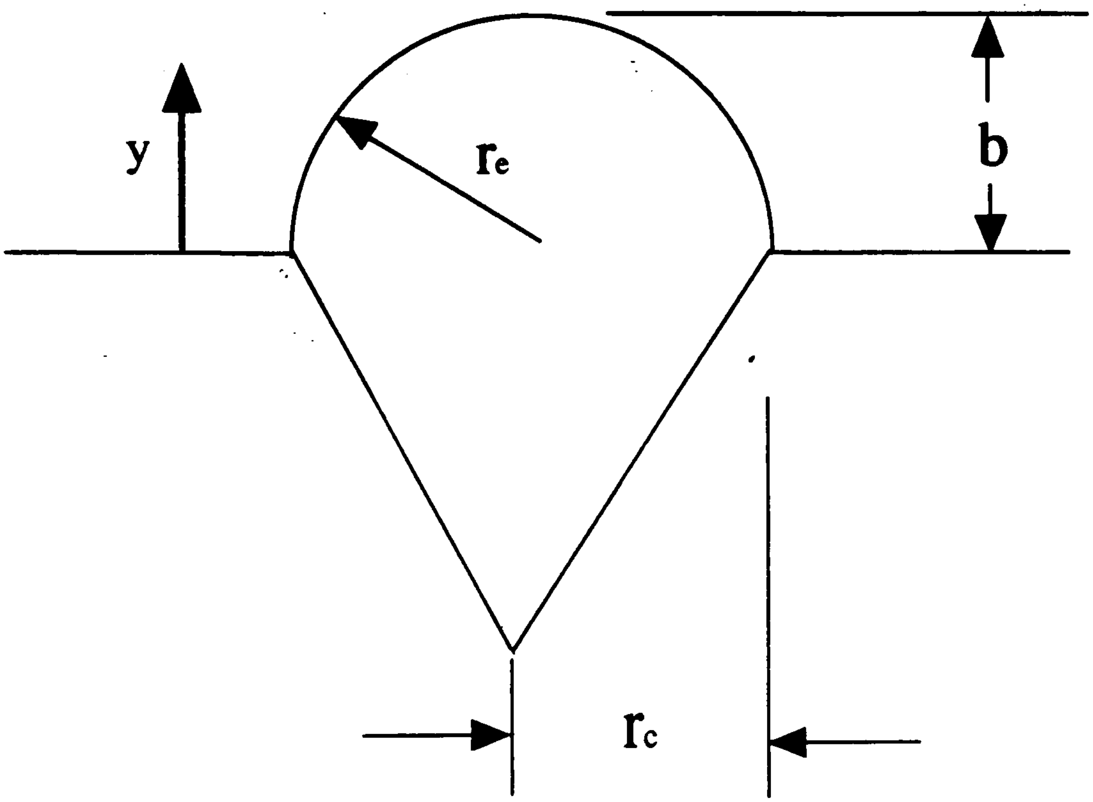

Figure 3.12 Representation of a bubble in Bergles and Rohsenow's (1964) nucleation model.

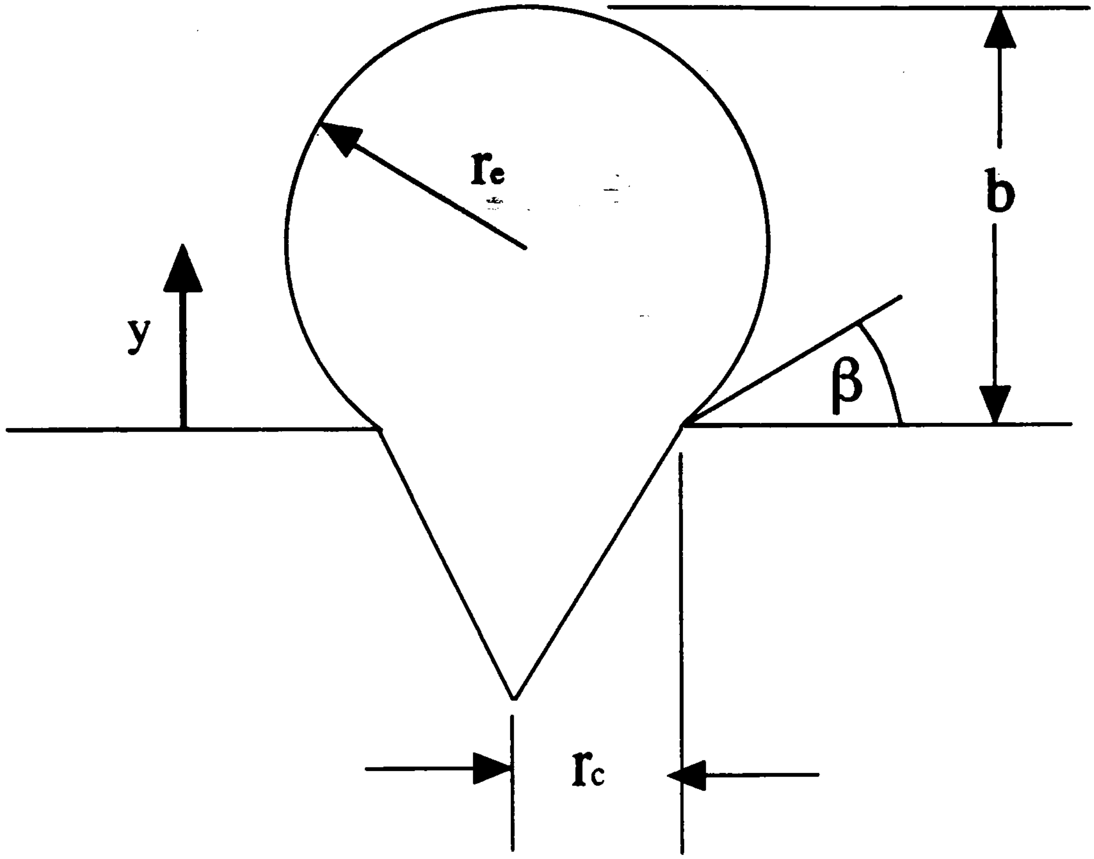

Figure 3.13 Representation of a bubble in Davis and Anderson's (1966) nucleation model.

$$b = \frac{r_c}{\sin\beta}\left(1 + \cos\beta\right) \tag{3.39}$$

For this model the resulting equation for $r_{c,\min}$ and $r_{c,\max}$ is shown below

$$\begin{Bmatrix} r_{c,\min} \\ r_{c,\max} \end{Bmatrix} = \frac{\delta_t \sin\beta}{2(1+\cos\beta)}\left[\left(1 - \frac{\theta_{SAT}}{\theta_w}\right) \mp \sqrt{\left(1 - \frac{\theta_{SAT}}{\theta_w}\right)^2 - \frac{8\sigma T_{SAT}(P_l)(1+\cos\beta)}{\theta_w \rho_v h_{lv} \delta_t \sin\beta}}\right] \tag{3.40}$$

A fourth nucleation model was presented by Kenning and Cooper (1965). In this investigation the flow pattern near a hemispherical vapor bubble nucleus in forced convection boiling heat transfer was modeled on a large scale by the flow past an air bubble. The experimental observations were used to deduce the surface temperature on the top of the bubble nuclei. The surface temperature was taken to correspond to that of the dividing stagnation streamline. The location of this streamline was determined experimentally and expressed as a function of the bubble Reynolds number (Fig. 3.14).

$$\frac{y}{r_c} = 0.54\left(1 - e^{\left(-\frac{\mathrm{Re}}{45}\right)}\right) \tag{3.41}$$

where

$$\mathrm{Re} = \frac{2 r_c u_r \rho_l}{\mu_l} \tag{3.42}$$

The importance of this concept is that the temperature at the top of the bubble will no longer correspond to the height b on the linear temperature profile as before, but instead it will correspond to the stagnation height y_s. Substituting y_s for y in Eq. 3.34 will then allow for the determination of the temperature at along the stagnation streamline

$$\theta = \theta_w - \frac{C_1 r_c}{\delta_t}(T_w - T_{BULK}) \tag{3.43}$$

where

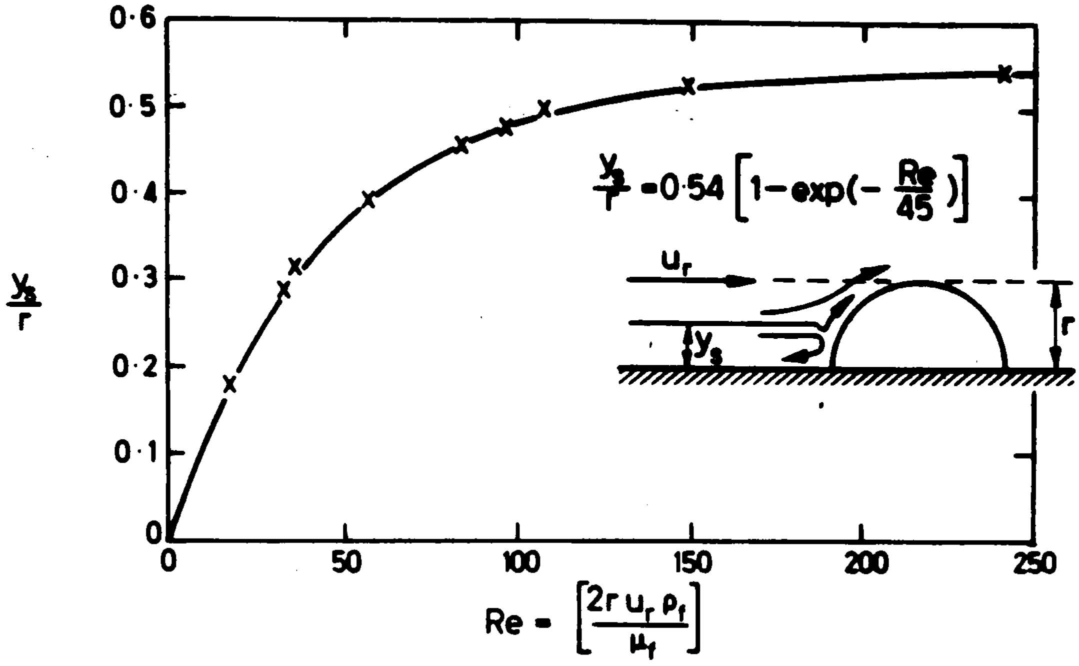

Figure 3.14 Representation of a bubble in Kenning and Cooper's (1965) nucleation model.

$$C_1 = 0.54\left(1 - e^{\left(-\frac{\mathrm{Re}}{45}\right)}\right) \tag{3.44}$$

Substituting Eq. (3.43) into (3.35) the following relationship can be found for the cavity radius.

$$r_c^2 - \frac{\delta_t}{C_1}\left(1 - \frac{\theta_{SAT}}{\theta_w}\right)r_c + \frac{\delta_t}{C_1}\left(\frac{2\sigma T_{SAT}(P_l)}{\theta_w \rho_v h_{lv}}\right) = 0 \tag{3.45}$$

Due to the complexity of the equation it was not readily possible to solve for a minimum and maximum radius without numerical techniques.

3.4 Comments on Literature Reviewed

The review of the basic papers presented in section 3.1 provides the foundation for theoretical development of nucleation criteria. The work on pool boiling and their extensions to flow boiling by previous investigators was based on some simplified assumptions regarding the bubble geometry. It is the intent of the present work to verify these assumptions and develop a more realistic model based on the experimental observations.

4. EXPERIMENTAL INVESTIGATION:

4.1. Experimental Setup

The experimental setup shown in Fig. 4.1 consisted of a constant temperature bath, flow meter, horizontal rectangular flow channel with attached aluminum heater, microscope, video recorder system, and temperature data acquisition unit.

The horizontal flow channel, made of 6061-T6 aluminum, had a 3x50 mm cross section, with a circular heater 9.4 mm in diameter placed in the center of the lower (50 mm side) wall. The heater was machined from aluminum 2024-T3 stock. The surface of the heater which is in contact with the flowing liquid (water) was polished on a cloth covered metallographic polishing wheel using 1μ particle size alumina in a water suspension resulting in a 1 μm surface finish. Four E-type thermocouples, with an accuracy of 0.1 °C, were placed along the length of the heater rod as shown in Fig. 4.2. They were bonded to the heater using Omega® CC High Temperature Cement which resists temperatures of up to 843°C, and is water, oil, and electrically resistant. The thermocouples were connected to a Keithley 740 System Scanning Thermometer which digitally displayed the temperature at each of the four thermocouples. A fifth thermocouple was attached to the thermometer to obtain the ambient air temperature in the vicinity of the test loop. The heater was insulated using a multi-layer fiberglass insulation and separated from the flow channel by a Torlon® bushing as shown in Fig. 4.3. In order to prevent leakage, the bushing was press fitted into the flow chamber as was the heater into the bushing. Both the top surface of the bushing and heater surface were flush with the lower face of the flow channel in an attempt to reduce flow instabilities. To

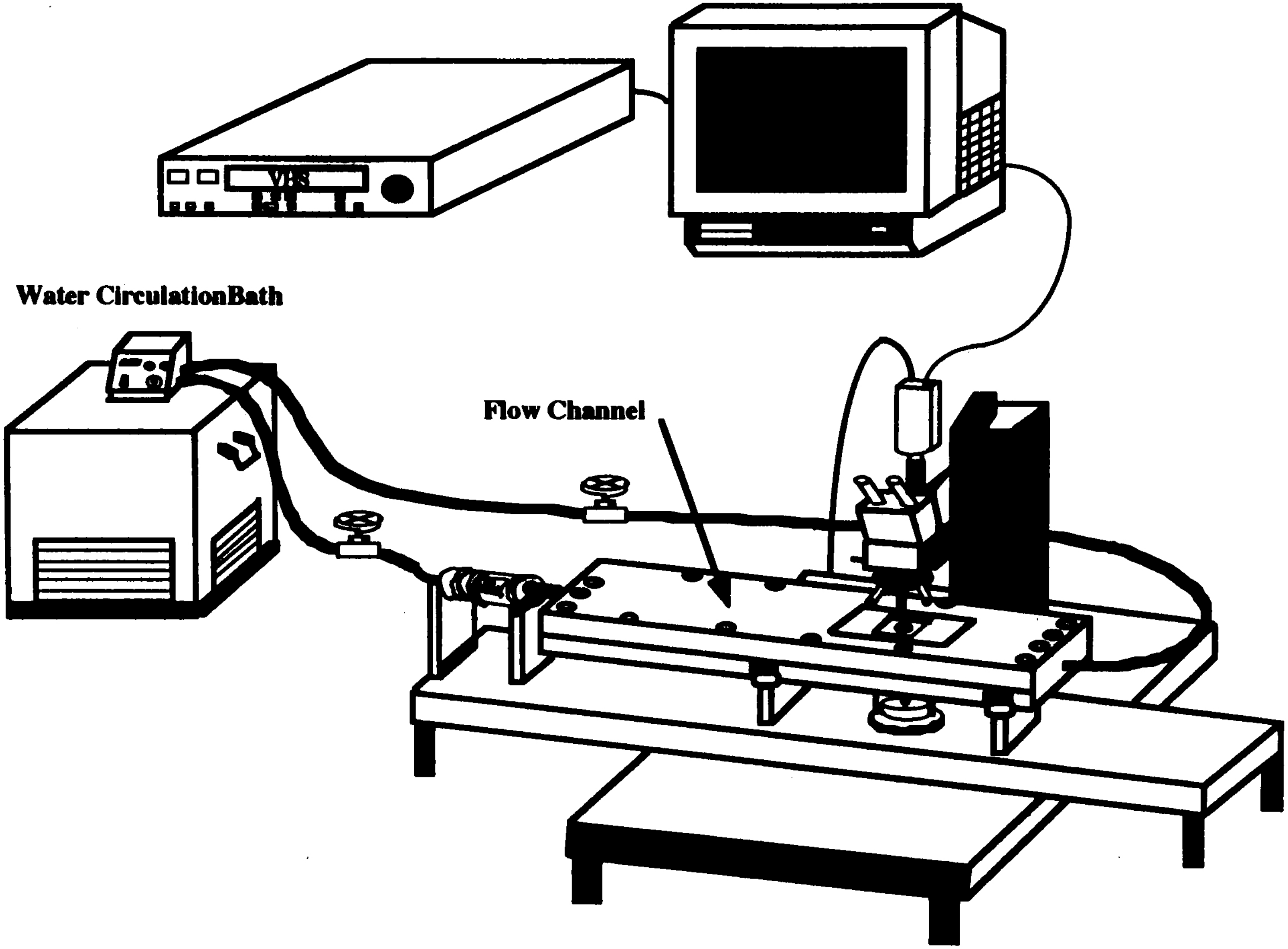

Figure 4.1 Experimental Flow Loop Setup

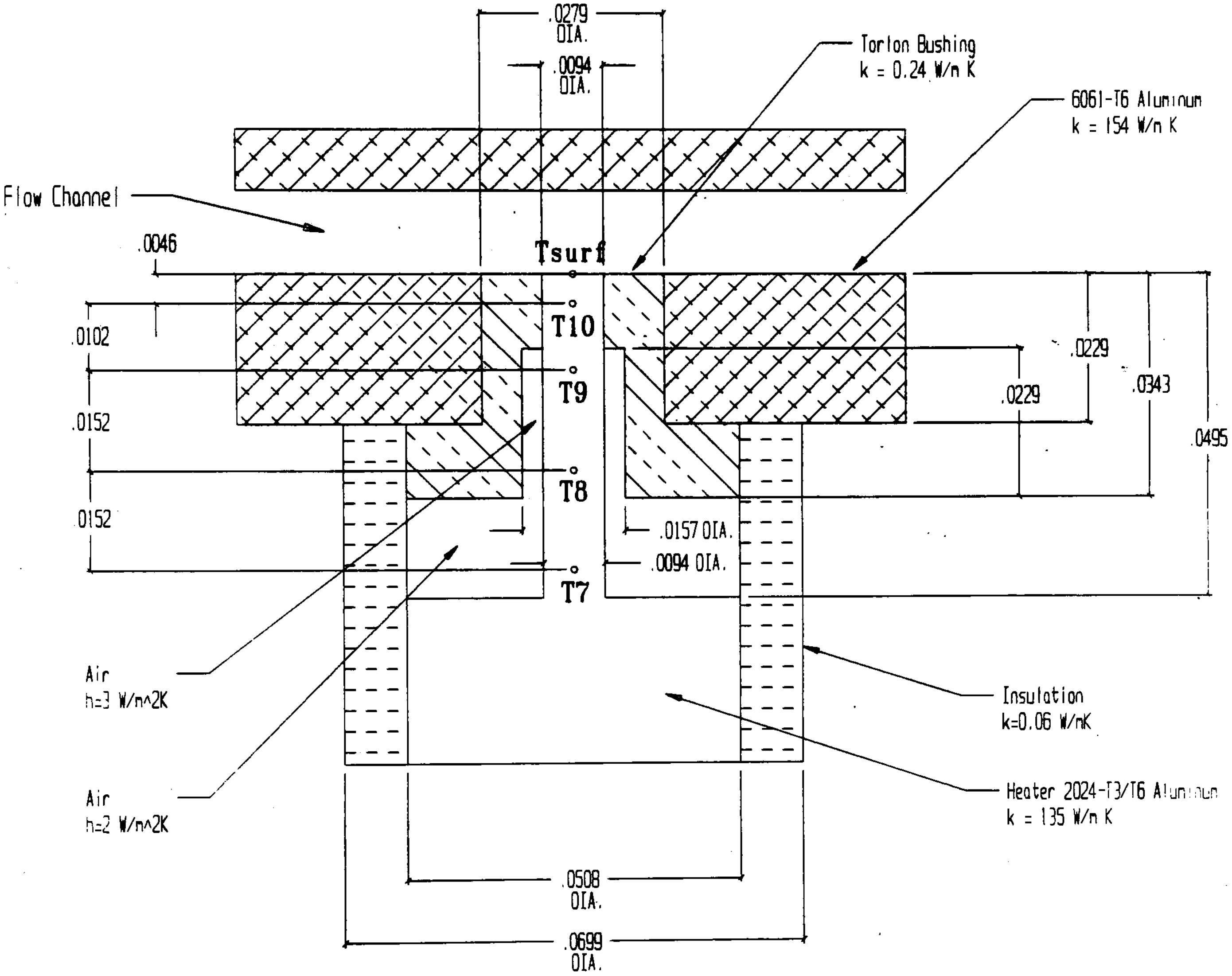

Figure 4.2 Heater cross section

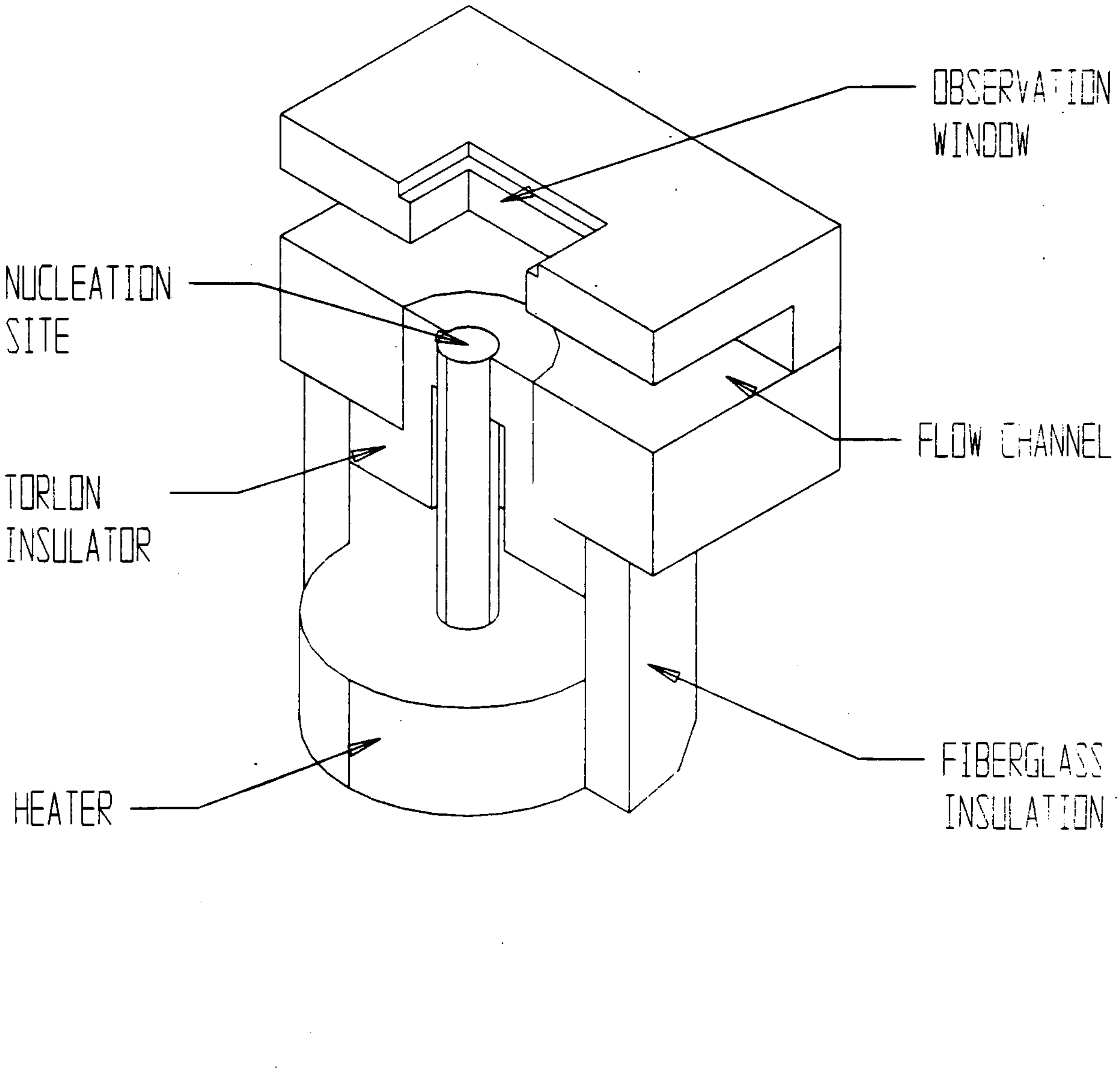

Figure 4.3 3-D View of the heater section.

ensure the two top thermocouples would not be pulled out of the heater when press fit into the bushing, a small channel was machined on the periphery of the heater rod to allow for adequate wire clearance between the heater and the bushing.

The aluminum rod was heated using a Watlow circumferencial electrical resistance heater wrapped around its base as shown in Fig. 4.3. The heater was connected to a voltage adjustable power supply capable of a maximum power output of 1500W.

The flow channel had a 50x50 mm window made of 1/4" thick polycarbonate located directly above the heater surface to allow for viewing (Fig. 4.2). A front surface silicon polished mirror was placed at 45° adjacent to the heater surface and parallel to the flow in order to allow for side viewing capabilities. To ensure viewing access to the base of nucleating bubbles, the mirror was embedded 1 mm into the bottom of the channel. The mirror was placed at a distance from the heated surface sufficient enough so as not to disrupt the flow field over the heater surface.

The length of the channel was 400 mm and the heater was placed 300 mm from the inlet in order to achieve a fully developed flow regime. The transition from the 1/2" inlet diameter to the 3x50 mm rectangular flow channel was smooth and gradual to achieve fully developed flow conditions.

The flow chamber was only one of many parts that made up the entire experimental test loop shown in Fig. 4.1. An MGW Laude RC20 constant temperature bath was utilized to ensure a uniform inlet water temperature. The bath could control the water temperature to within 0.1°C and had a total capacity of approximately four gallons. A variable flow pump was integrated into the constant temperature bath, and had a maximum pumping capacity in the range of 2 GPM for the experimental test loop configuration. The flow rate was measured using an Omega® FL-1503A rotameter calibrated for a maximum flow of 2.53 GPM. The meter measured percentage of the maximum flow in 2% increments which yielded an accuracy of ± 0.025 GPM. The constant temperature bath, the rotameter and flow chamber were connected by a 1/2" inside diameter high temperature hose.

The visual setup consisted of a Micromanipulator® HSDS-1 microscope equipped with a variable magnification eye piece and three Bausch & Lomb lenses. The microscope was also equipped with a special mount for video cameras. This allowed for simultaneous viewing of the surface by both the attached eye piece as well as a Sony Trinitron GVM 1300, 20" Monitor. All cavity and bubble size measurements were taken from the monitor. Since the image magnification was dependent on both the lens and the camera used. The resulting magnification for different combinations is listed in Table 4.1.

The first of the two cameras used was a Hitachi KP-C501, all Solid State color camera which had a recording speed of 30 frames per second (fps). This camera was used mostly to record slower growing bubbles, or when a higher quality picture was required. For viewing bubbles with fast growth rates, a high speed Kodak Ektapro 1000 Image Intensifying system was used. This camera had the capability to capture images at a rate as high as 6000 fps. The high speed camera had no mechanical shutter, rather an image intensifying system which electronically controlled aperture setting depending on the available lighting. This allowed for images to be captured without the use of a flash, liasrequired by many other high speed cameras. The high speed image could be played back at 30 fps and transfered to a normal VHS tape through a Panasonic AG-6300 video cassette recorder. This VCR had the capability to advance one frame at a time which is

Color Camera

Lens	Eyepiece	Magnification
2.25*0.04	1	60
	2	120
8*0.15	1	210
	2	420
25*0.31	1	675
	2	1350

High Speed Camera

Lens	Eyepiece	Magnification
2.25*0.04	1	20
	2	40
8*0.15	1	70
	2	140
25*0.31	1	215
	2	430

Table 4.1 Microscope Lens/Camera Combined Magnification

required when accurately determining the location of bubble nucleation sites and bubble growth rates.

4.2. Experimental Procedure

The fluid used in the experiments was distilled water. In order to clean the test loop from any impurities that may affect the results, water at or above 90°C was circulated through the system over a period of several hours and then drained. After draining the system, the inside of the tank of the constant temperature bath was thoroughly cleaned by physical means (wiping the inside with paper towels). Chemical additives for cleaning the system were not utilized since even slight traces of their presence would cause significant change in the physical properties of the water (especially in the surface tension values).

The system was then filled with new distilled water, which was circulated at temperatures in the range of 85-90°C for over five hours. This was done in order to remove any dissolved gasses from the water, otherwise known as degassing. Through this procedure, it was ensured that the observed bubbles are product of heterogeneous boiling at the heater surface, rather than from the degassing.

The surface tension values of the water used in the testing at temperatures between 20°C and 60°C were verified through the use of three basic experimental techniques: capillary rise test, a drainage technique method, and by method of direct pull. Refer to the results of the capillary rise test in the Appendix A. All tests resulted in surface tension values within 5% of the published values for pure water at the corresponding temperatures. This finding led to the conclusion that the published surface tension values could be used in the analysis supporting the current work.

Once the system was flushed and degassing was completed, the actual experimental procedure began. The first step was to set the constant temperature bath to a specified value within the range of 60-90°C and adjust the flow to a constant value in the range on 0.25-1.00 GPM. The system was allowed time to reach a steady state condition (approximately 1 hour). Once steady state was achieved, the heater power was turned on. The voltage and current were gradually increased based on the reading of the thermocouples until a temperature slightly lower than the water saturation temperature was achieved near the heater surface.

At this point the voltage was incrementally increased, each time allowing the thermocouple temperature readings to stabilize between the voltage increases. The constant temperature values were recorded and later processed using ThermoNet^{TM} to find the surface temperature and the heat transfer from the heater surface to the water (see ThermoNet^{TM} Analysis section). The voltage was increased by equal amounts until a wall superheat of approximately 14-16°C was achieved.

As the surface temperature approached the saturation temperature, the Hitachi color camera was employed to closely observe the heater surface and detect the onset of nucleation. Once active cavities were observed, the high speed Kodak camera was utilized to record the bubble nucleation, growth, and departure phenomena. Before the image could be recorded, the high speed Image Intensifying system required the tape to be conditioned through the Intensified Image Controller for proper operation when capturing images at high frame rates. The captured images were then transferred from the high speed tape to a normal VHS tape through a Panasonic AG-6300 VCR. This procedure was repeated often because when recording at frame rates of 1000 fps the tape could only store 30 seconds of images, and only 5 seconds when using 6000 fps.

Each recorded series had a unique session number which was used for matching it with a corresponding temperature distribution during later analysis. This information was recorded on a data sheet (Appendix D) which also contains information on liquid conditions (flow rate and temperature), lens magnification, and power supply output. The data sheets were sequentially numbered, and dated. A log of over 40 data sheets with more than 200 data sets was collected over the course of the experimental testing. The flow rate for each corresponding water temperature was varied between 10% and 40% of the maximum flow rate (0.25-1.00 GPM).

Since only a small portion of the heated surface could be observed in the field of view, the microscope was translated to numerous locations for each flow condition in order to scan the entire heater surface.

4.3. ThermoNet™ Analysis

4.3.1 ThermoNet™ Model

The temperature measurement obtained from the thermocouples gave a temperature distribution along the length of the aluminum heater rod, unfortunately the surface temperature was not known. In order to determine this temperature, ThermoNet™, a thermal network analysis software, was utilized.

The heater assembly system consisting of aluminum rod, Torlon bushing, and installation wrapping was discretized into the network of 66 nodes as well as numerous convection and conduction resistances as shown in Figs. 4.4 and 4.5. The values for the thermal resistances in the heater were calculated using the following equations

$$R_{COND} = L/kA_C \text{ (Axial)} \tag{4.1}$$

$$R_{COND} = \ln(r_2/r_1)/2kL \text{ (Radial)} \tag{4.2}$$

$$R_{CONV} = 1/hA_S \tag{4.3}$$

where A_C is the cross sectional area, A_S is the surface area and r_1 and r_2 are the inner and outer radius of a cylinder respectively.

A spread-sheet was formulated to calculate all the resistance values used in the model (Appendix B). VisualNet™ was used to create a visual nodal/resistance model as shown in Fig. 4.5. The node and resistance information created in VisualNet™ was transferred to ThermoNet™ where a steady state analysis was performed on the model.

The nodes 1, 6, 12, and 18 in Fig. 4.5 correspond to the four thermocouples with node 1 being the thermocouple (T7) located nearest to the base and node 18 being the thermocouple nearest to the surface. Other important nodes and resistances are node 21 which represented the heater surface, node 22 which represented the temperature of the flowing water and resistance 80 which was the combined boiling and convective resistance between the surface(21) and the flowing water (22). Node 39 represented the surface of the Torlon® bushing. Since no boiling occurred on the Torlon® surface, the resistance (130) between it and the flowing water (22) was purely a single phase convective resistance having no boiling component.

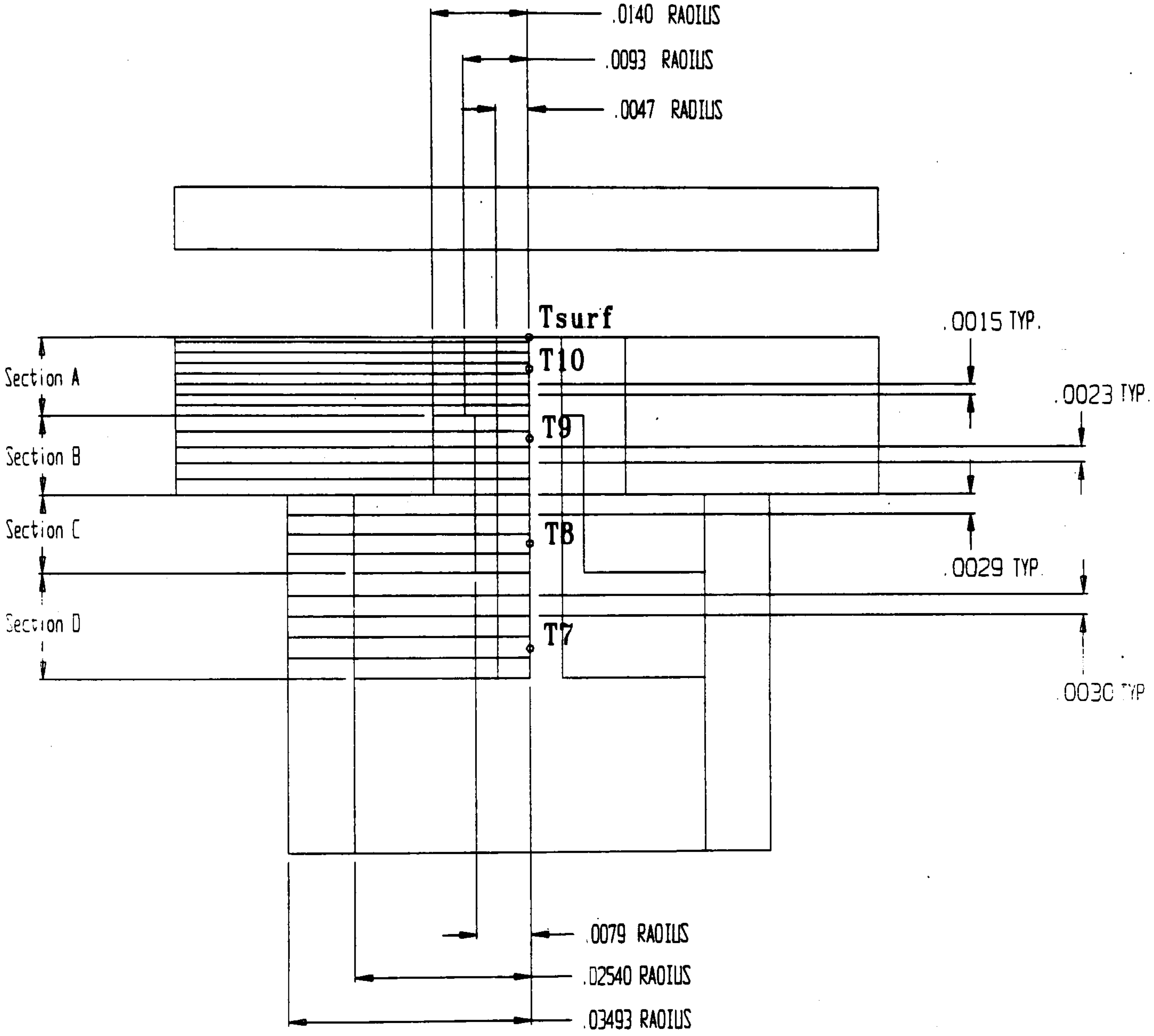

Figure 4.4 Disretisized heater

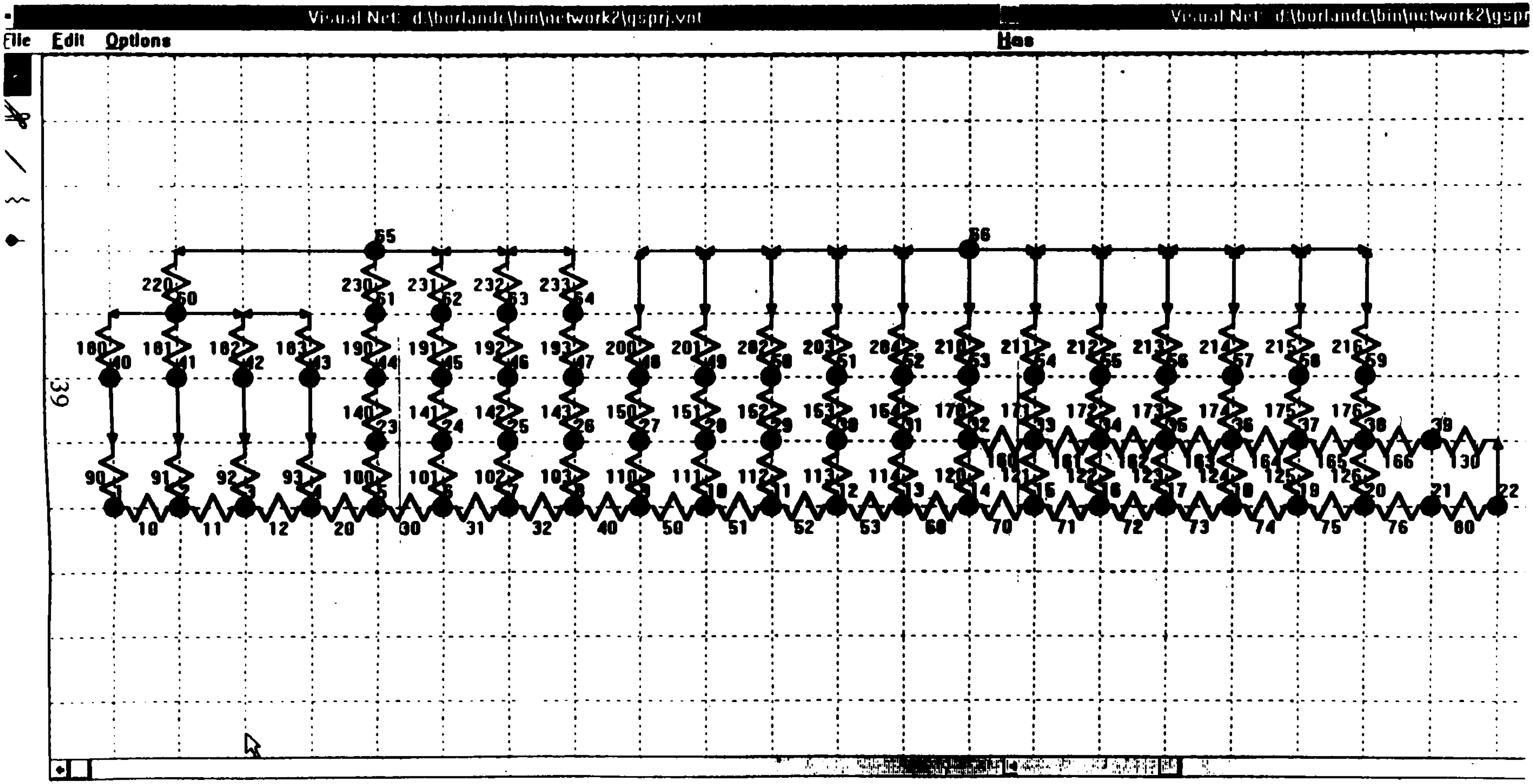

Figure 4.5 VisualNet Node/Resistor Setup

4.3.2 Analysis Procedure

In order to accurately calculate the heater surface temperature and heat transfer from the surface to the water, the temperature reading from T7 was entered into node 1 for heater temperature distribution at sub-boiling conditions, and the specified water temperature was entered into node 22. An initial guess for the convective heat transfer coefficient (h) was calculated using Gnielinski's correlation (1976)

$$Nu_D = \frac{(f/8)(\mathrm{Re}_D - 1000)\mathrm{Pr}}{1 + 12.7(f/8)^{1/2}(\mathrm{Pr}^{2/3} - 1)} = \frac{hD}{k} \tag{4.4}$$

where

$$f = (0.79 \ln \mathrm{Re}_D - 1.64)^{-2} \tag{4.5}$$

for a single-phase flow across a flat plate. This h value was then used to calculate resistances 80 and 130. At this point the steady state model was ready for analysis. After running the model, the calculated temperatures for nodes 6, 12, and 18 were compared with the corresponding thermocouple readings T8, T9, and T10. Adjusting resistance 80 by a small increment, a better match of the model temperatures to the thermocouple readings could be achieved. This process was continued until a satisfactory match was found between the calculated values and the thermocouple readings. Once a suitable match (less then 0.1°C error for each of the three temperature readings) was found for a given flow condition, the single-phase convective resistance was found. For subsequent heater temperature distributions at the same flow conditions the convective resistance was held constant for resistance 130, while resistance 80 was changed to take into account for the effects of additional heat transfer due to the onset of nucleate boiling. An iterative process was again employed to match the calculated node temperatures with the thermocouple readings, this time only changing the value of resistance 80.

Once a match was made between the calculated node temperatures and thermocouple readings, the total heat transferred from the heater surface (node 21) to the bulk water (node 23) could be found using a data viewing feature available in ThermoNet™. Substituting this value into the equation for convective heat transfer, and solving for h, the heat transfer coefficient can be determined.

$$q = hA_s(T_w - T_{BULK}) \tag{4.6}$$

Another important parameter that could be found experimentally was the thermal boundary layer. Assuming that the boundary layer was fully developed and a constant thickness the heat transferred by conduction from the heater surface through the boundary layer must be equal to the heat transferred to the bulk water.

$$q = \frac{kA_s(\Delta T)}{\delta_t} = hA_s(\Delta T) \tag{4.7}$$

By dividing like terms the thermal boundary layer is defined as:

$$\delta_t = \frac{k}{h} \tag{4.8}$$

4.4 Determination of Experimental Error

There were several sources of error associated with the experimental setup and the data collection techniques utilized.

- The bulk temperature of the liquid, T_w, could be controlled within 0.1°C in the constant temperature bath.

- The flow rate and the flow velocity were measured within accuracy of 1 % of the rotameter range which yielded an error of 0.025 GPM.
- The heater surface temperature, obtained from the ThermoNet model was accurate within 0.1°C.
- The thermocouple temperature readings, used in the ThermoNet analysis were accurate within 0.1°C.
- The bubble size visual measurements were accurate within 2 μm as a result of the monitor resolution.

5. THEORETICAL MODEL DEVELOPMENT

In the literature review, four models on bubble nucleation were discussed. Hsu's (1962) model assumed that the bubble height b would be defined by equation 3.32

$$b = 2r_c = 1.6r_e \tag{5.1}$$

Bergles and Rohsenow (1964) and Kenning and Cooper (1965) both assumed a hemispherical bubble. While Davis and Anderson (1966) suggested that the bubble height was a function of the contact angle, they did not incorporate the effects of the stagnation streamline as done in Kenning and Cooper's work. However, the assumptions for bubble geometry made in these models have not been verified and the numerical work used to determine the location of the stagnation streamline in Kenning and Cooper's work was based on large bubbles.

From experimental work done by Kandlikar and Stumm (1995) it is seen that the bubbles are not be hemispheric, but are rather of truncated spherical shape with different front and rear contact angles. For low flow rate the front and rear contact angles will be comparable, suggesting the bubble is almost a perfectly spherical truncated bubble. Also, when the bubbles are small, the two angles tend to be the same. Both phenomena were verified in preliminary experimentation and have lead to the postulation that the bubble is a truncated sphere with alike front and rear contact angles for bubbles smaller than 200 μm in diameter. Davis and Anderson (1966) used a similar assumption for the bubble geometry, but did not incorporate the effects of the stagnation streamline. The model which is proposed in this chapter will incorporate both the truncated sphere and the stagnation streamline analysis.

5.1 Location of the Stagnation Streamline

Kenning and Cooper (1965) experimentally determined the location of the stagnation stream line by studying flow past an air bubble. It is extremely difficult to conduct such experiments withh extremely small bubbles, thus computational fluid dynamic software (CFDS) was used instead. Due to the complexity involved with CFD modeling, this topic has been taken up by another graduate student at RIT, and is presented in its entirety in Ikenzi (1995). In Ikenzi's work, the software STAR CD was used to model a rectangular channel, 3mm x 50mm, corresponding to the actual bubble flow chamber with a bulk water temperature of 70°C. The channel was 300mm long with a bubble placed 200mm from the entrance on the center of the channel floor. The bubble was modeled as a truncated sphere with a contact angle of 46°. Multiple models were made for varying flow rates and bubble radii.

Fig. 5.1 shows shaded pressure contours along the surface of the bubble. As shown in the figure, the pressure over a small portion of the upper hemisphere on the front half of the bubble is significantly higher than anywhere else on the bubble surface. This area represents the location of the stagnation point and corresponding stagnation streamline. Using the numeric data files created by the software, the exact location of the stagnation point was determined and represented as θ, the angular elevation from the horizontal axis passing through the center of the sphere. Fig. 5.2 shows the angle θ, as well as the rest of the important bubble geometry used in the proposed model. The resulting locations of stagnation point from the various CFD models have been summarized in Table 5.1. From this data the height of the stagnation streamline y_s was

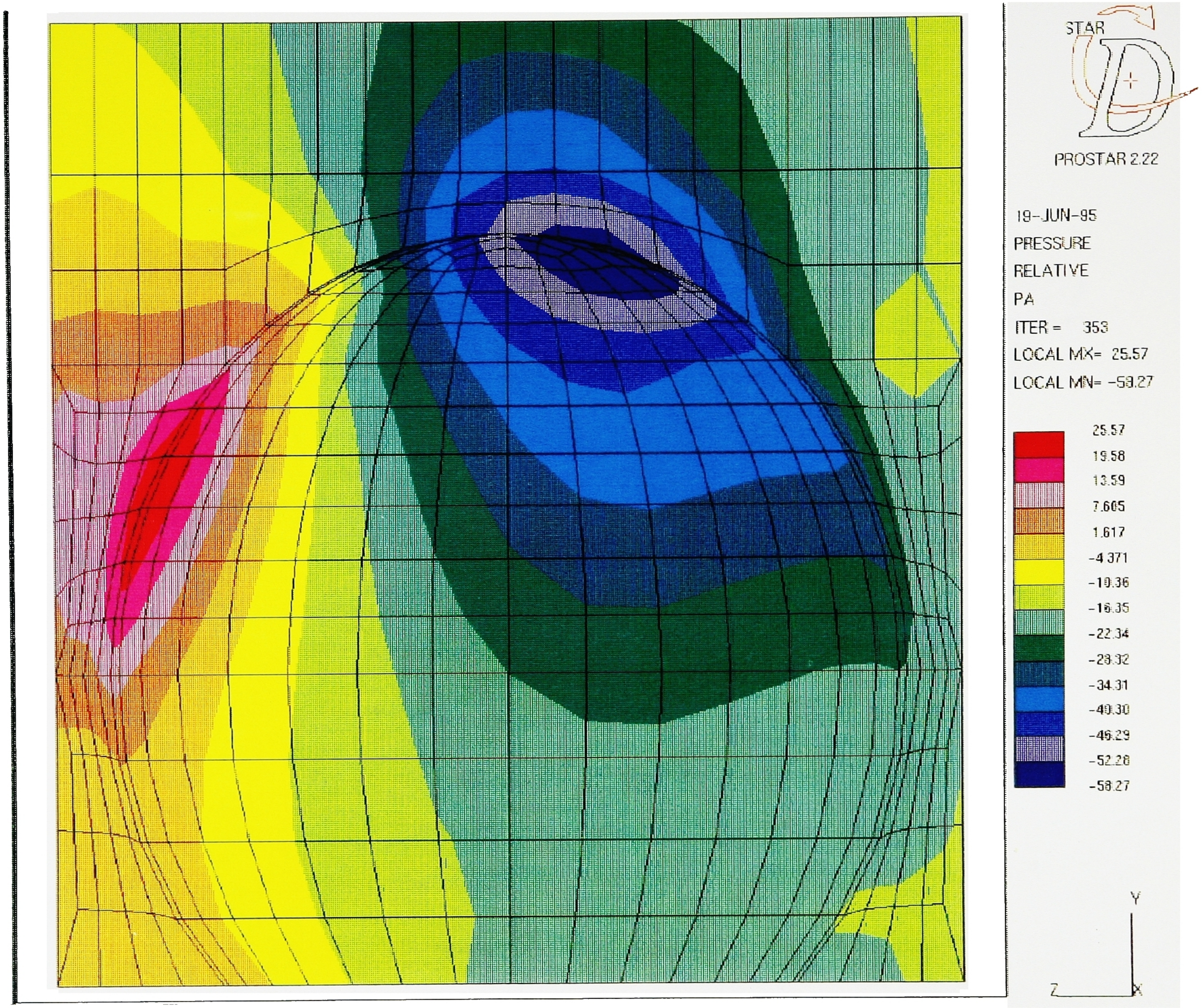

Figure 5.1 Pressure distribution across the surface of the bubble.

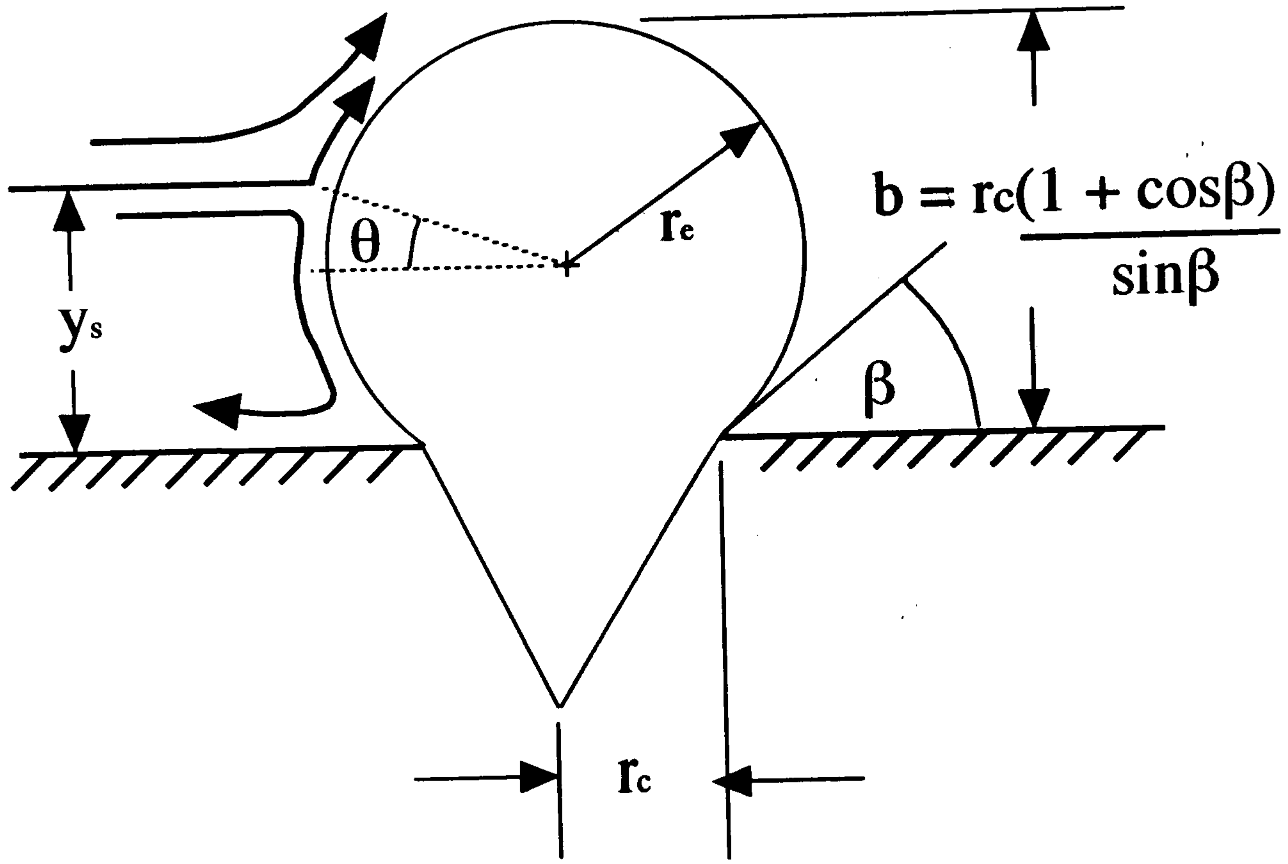

Figure 5.2 Representation of bubble in proposed stagnation/truncated nucleation model.

calculated and normalized by dividing by the bubble radius r_b. This information is also found in Table 5.1. For all of the different models the value for y_s/r_b was constant, resulting in the following relationship

$$\frac{y_s}{r_b} = 1.10 \tag{5.2}$$

5.2 Determination of Contact Angle

In section 4.1, Experimental Setup, the side viewing capabilities were discussed. Taking advantage of this feature, side views of nucleating bubbles were studied in depth. For this portion of the investigation the high-speed camera was used to capture images of the bubble profile. Figure 5.3 shows a typical bubble profiles captured by the video imaging system. In this figure it is apparent that the bubbles are almost perfectly spherical with front and rear contact angles measured to be 45°.

For this analysis the flow rate was varied in the range of 0.17 to 0.40 m/s with corresponding Reynolds numbers of 2027 to 4815. A plot of contact angle versus bubble angle has been constructed for all of the collected experimental data (Fig. 5.4). From this figure it is apparent that the contact angle increased with flow rate for water at 60°C. An important point that should not be ignored is that for many of the points, particularly at higher flow rates, the contact angle is actually the average value of the front and rear contact angles.

Table 5.1 Location of stagnation point using CFD

Bubble of 150 μ radius and contact angle, β = 46°C.

Inlet Velocity (m/s)	Re	θ (deg)	y_s (mm)	y_s/r
0.2	2381	23.74	0.165	1.1
0.4	4762	23.74	0.165	1.1
0.6	7143	23.74	0.165	1.1
0.8	9525	23.74	0.165	1.1
1	11906	23.74	0.165	1.1

Bubble of 75 μ radius and contact angle, β = 46°C.

Inlet Velocity (m/s)	Re	θ (deg)	y_s (mm)	y_s/r
0.2	2381	23.4	0.082	1.1
0.4	4762	23.4	0.082	1.1
0.6	7143	23.4	0.082	1.1
0.8	9525	23.4	0.082	1.1
1	11906	23.4	0.082	1.1

Bubble of 37.5 μ radius and contact angle, β = 46°C.

Inlet Velocity (m/s)	Re	θ (deg)	y_s (mm)	y_s/r
0.2	2381	23.4	0.082	1.1
0.4	4762	23.4	0.082	1.1
0.6	7143	23.4	0.082	1.1
0.8	9525	23.4	0.082	1.1
1	11906	23.4	0.082	1.1

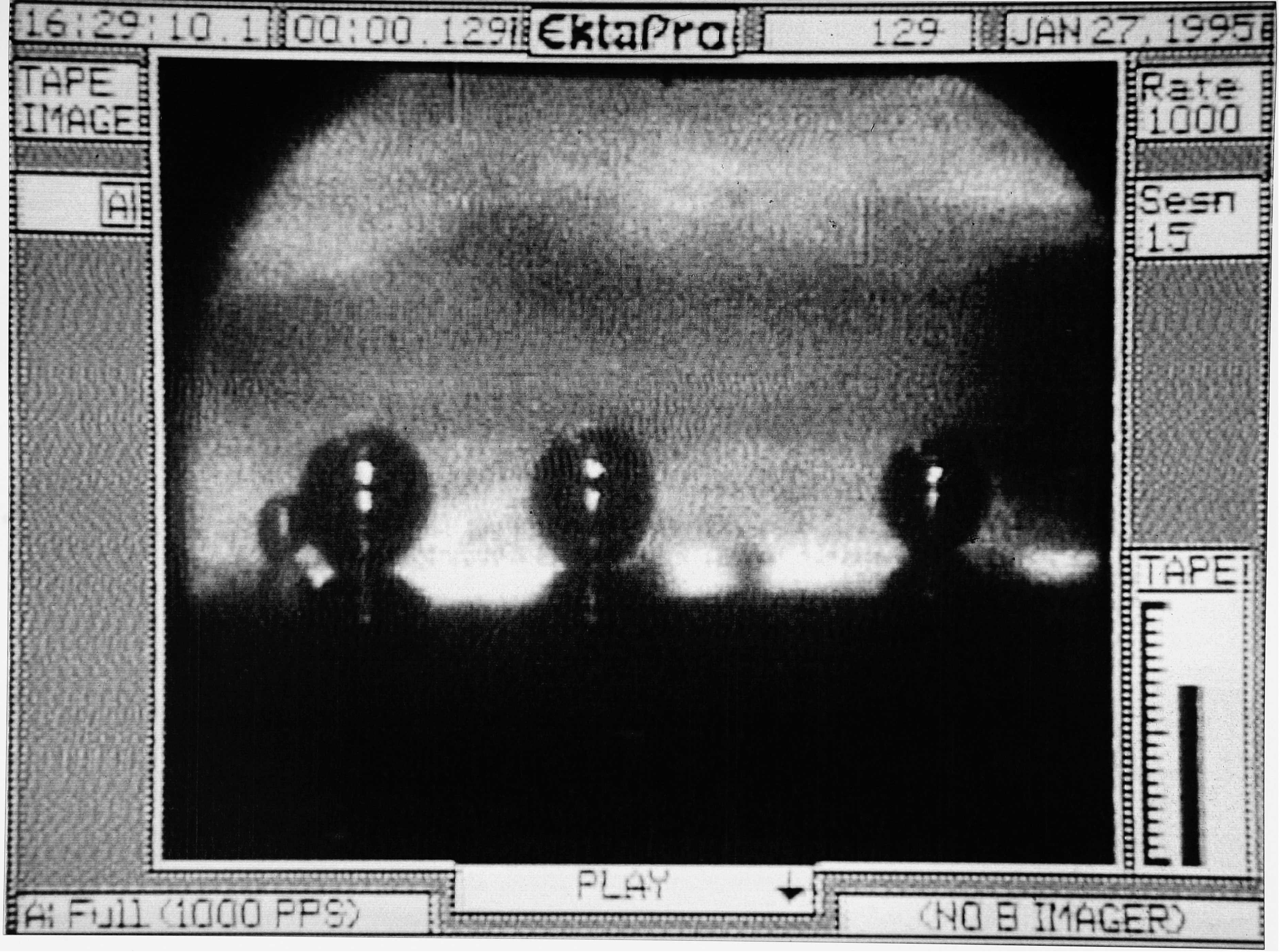

16:29:10.1 00:00.129 EktaPro 129 JAN 27, 1995

TAPE IMAGE

A

Rate 1000

Sesn 15

TAPE

PLAY

A: Full (1000 PPS)

(NO B IMAGER)

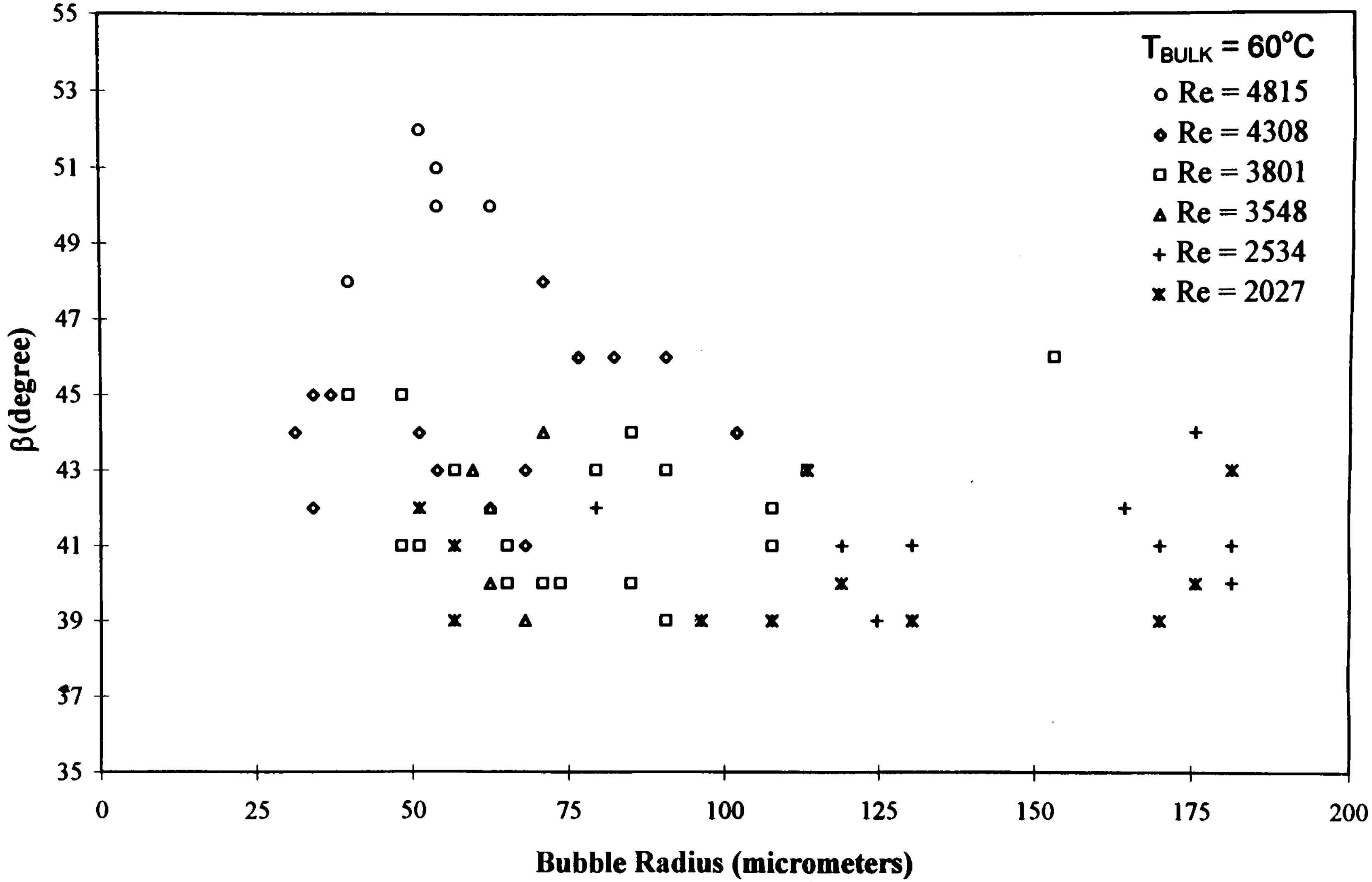

Figure 5.4 Experimental data of contact angle versus bubble radius.

Taking the average value for all of the data points at each Reynolds number allowed for the creation of Fig. 5.5. Using the curve fitting capabilities in Excel a linear equation was fit to the data points. The resulting equation was found:

$$\beta = 0.0029\,\mathrm{Re} + 33.242 \tag{5.3}$$

As seen in the Fig 5.5 the curve fit is not perfect, but does allow for a rough approximation of the contact angle as a function of flow rate. The data used in both Fig. 5.4 and 5.5 is presented in Appendix E.

5.3 Model Development

Determining the height of the stagnation stream line and bubble contact angle were an important starting point in the development of a model for predicting the criteria for bubble nucleation in subcooled flow. Using the same methodology as described in section 3.3 for Hsu's (1964) model, an equation for the maximum and minimum cavity radius required for nucleation can be determined.

Assuming a linear temperature profile the temperature of the liquid at a height corresponding to the stagnation streamline could be found using the following equation

$$\theta_s = \theta_w - \theta_w \frac{y_s}{\delta_t} \tag{5.4}$$

where $\theta_s = T_{STAG} - T_{BULK}$ and $\theta_w = T_w - T_{BULK}$. From basic geometry the radius of the bubble r_b can be related to the cavity radius r_c as follows:

$$r_b = \frac{r_c}{\sin\beta} \tag{5.5}$$

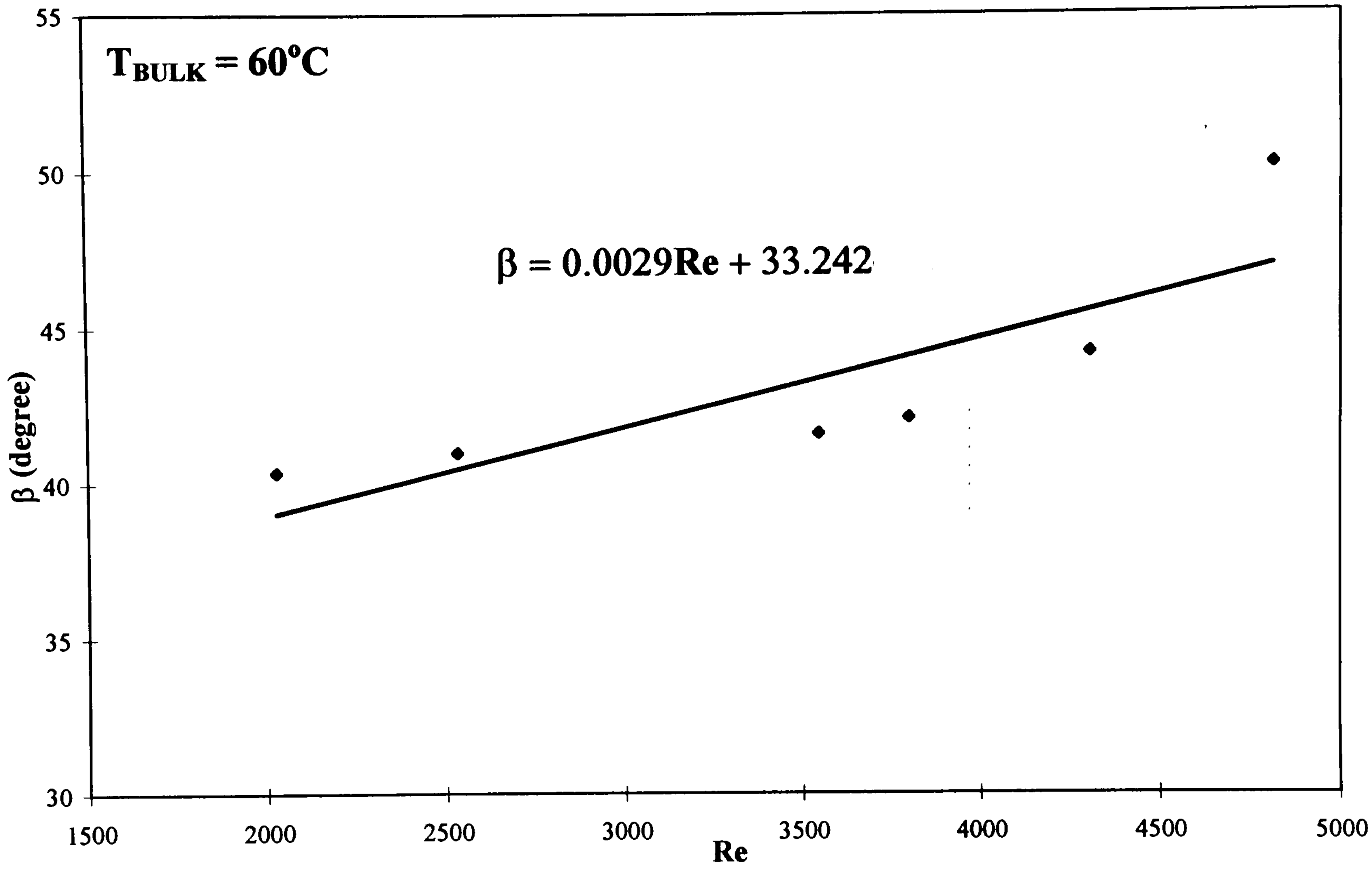

Figure 5.5 The averaged value of contact angle versus Reynolds number.

where β is defined by Eq. (5.3).

Combining Eq (5.5) with the Eq (5.2) the following equation for y_s can be determined.

$$y_s = \frac{1.1 r_c}{\sin\beta} \tag{5.6}$$

Using Eq. (3.35) from before, an equation relating the equilibrium superheat at the stagnation stream line and bubble radius can be derived as

$$\theta_s - \theta_{SAT} = \frac{2\sigma T_{SAT}(P_l)}{\rho_v h_{lv} r_e} \tag{5.7}$$

Substituting Eq. (5.4) and (5.6) into Eq.(5.7), the following relationship can be found for the cavity radius

$$r_c^{\,2} - \frac{\delta_t \sin\beta}{1.1}\left(1 - \frac{\theta_{SAT}}{\theta_w}\right) r_c + \frac{\delta_t \sin\beta}{1.1\theta_w}\left(\frac{2\sigma T_{SAT}(P_l)}{\rho_v h_{lv}}\right) = 0 \tag{5.8}$$

Solving this quadratic equation for $r_{c,\min}$ and $r_{c,\max}$ gives the following equations

$$\left\{\begin{matrix} r_{c,\max} \\ r_{c,\min} \end{matrix}\right\} = \frac{\delta_t \sin\beta}{2.2}\left[\left(1 - \frac{\theta_{SAT}}{\theta_w}\right) \pm \sqrt{\left(1 - \frac{\theta_{SAT}}{\theta_w}\right)^2 + \frac{9.2\sigma T_{SAT}(P_l)}{\theta_w \delta_t \rho_v h_{lv} \sin\beta}}\,\right] = 0 \tag{5.9}$$

6. SURFACE VISUALIZATION

Before an in-depth investigation into the initiation of nucleate boiling can be conducted, a visual study of the heater surface characteristics is warranted. There are two important reasons for doing this. First, as mentioned in the earlier literature review, in order to have heterogeneous nucleation occur at relatively low wall superheats (10 - 15 °C), vapor must be trapped within cavities located on the metal surface. Bankoff (1958) did studies on the entrapment of vapor in idealized conical cavities. From this work it was determined that the cavity cone angle 2γ (Fig 3.5) must be less then the contact angle of the fluid on the heater surface. From literature it is known that for water the contact angle will be between 20° and 100°, depending on the surface material and roughness. Bubble cavity profiles will be studied experimentally through the use of an atomic force magnifier to ensure the existence of cavities falling in this range.

The second reason for completing the visual study comes from the work discussed in section 3.3 on the criteria for the onset of nucleate boiling. In this section an analysis completed by Hsu (1962) is reviewed, resulting in the derivation of the following equation

$$\begin{Bmatrix} r_{c,\min} \\ r_{c,\max} \end{Bmatrix} = \frac{\delta_t}{4}\left[\left(1-\frac{\theta_{SAT}}{\theta_w}\right) \mp \sqrt{\left(1-\frac{\theta_{SAT}}{\theta_w}\right)^2 - \frac{12.8\sigma T_{SAT}(P_l)}{\theta_w \rho_v h_{lv} \delta_t}}\right] \tag{6.1}$$

The range of active cavities predicted by this equation is indicated in Fig 6.1 for conditions corresponding to a water bulk temperature of 75 °C and a thermal boundary layer thickness of 0.17 mm. From this plot it can be seen that for a typical wall superheat temperature of 9°C, only cavities in the range of 1 - 24 μ will be active. For this reason the surface needs to be studied to verify the existence of cavities in this size range.

6.1 Result of Surface Visualization

Using the atomic force magnifier in RIT's Material Science Laboratory, several cavity profiles were observed. As expected, none of the cavities were perfectly conical as in theory, but for the most part they had a conical shape to them. Many of the cavities that were studied had cone angles which fell into the range of 20 - 100°. This suggested that vapor would be entrapped allowing for nucleation at low superheat values.

A size range of cavity on the heater surface was determined by viewing the surface with a high magnification microscope and displaying the image on a video monitor through the use of a Hitachi video camera. Fig. 6.2 Shows a typical frame, transferred from video, of the heater surface seen from above. In this figure the surface is covered with many large spots, most of these are cavities or crevices. One cavity in particular is pointed out with an arrow. In this cavity a bubble was shown to nucleate and then depart in later frames. From this visual study it could be seen that on the heater surface cavities in the range of a few microns in diameter all the way up to several hundred microns were in existence. It is important to note that the mouth of the cavities , as seen in Fig. 6.2, were not perfectly round. In the case of these cavities an average value of several measurements was used.

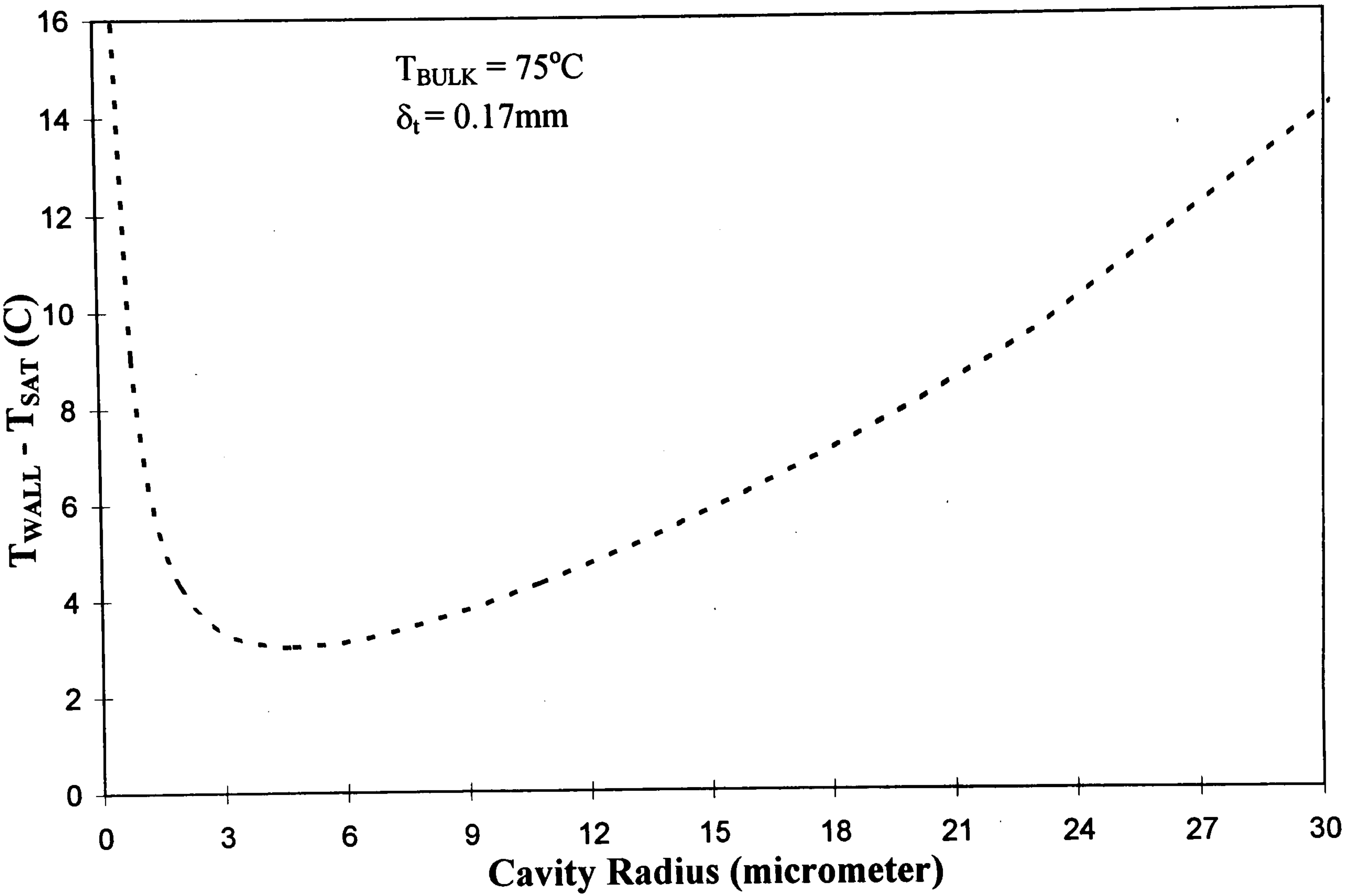

Figure 6.1 Prediction of the range of active cavities using Hsu's (1962) anlysis.

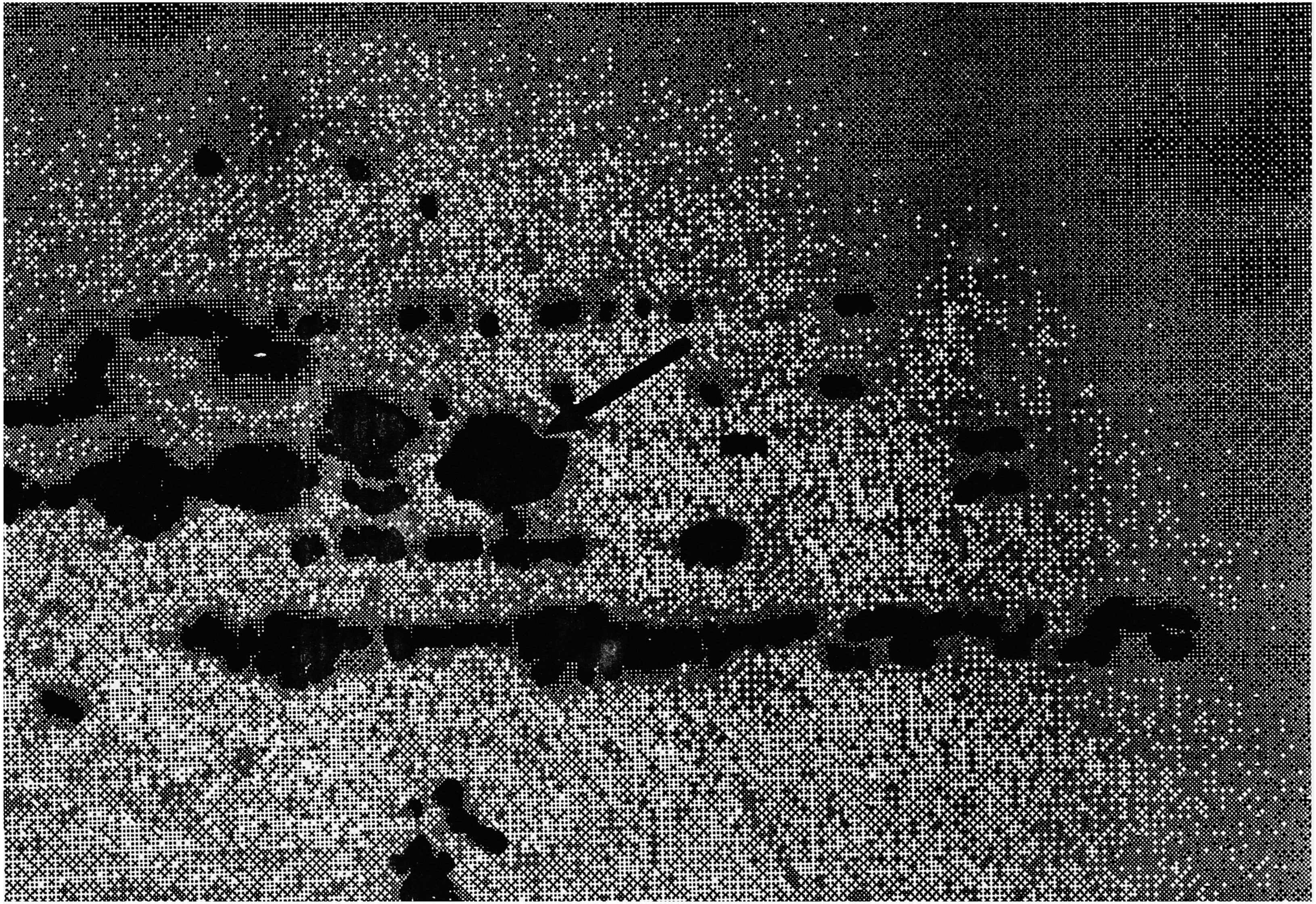

Figure 6.2 Top view of cavities on heater surface.

7. EXPERIMENTAL RESULTS AND DISCUSSION

In this investigation, the initiation of nucleation was identified through two techniques. The first one involved observing the change in heat transfer coefficient corresponding to the onset of nucleate boiling starting from the single phase non-boiling condition. This was accompanied by simultaneously recording the heater surface to visually capture nucleation activity using a high-speed camera.

7.1 Heat Transfer Coefficients in Subcooled Boiling

In this section, experimentally determined heat transfer coefficients for subcooled water in the range of 60 to 90 °C are presented and discussed in detail. The experimental heat transfer coefficient, h, is plotted against wall superheat, T_{SURF} - T_{SAT}, as shown in Figs. 7.1 through 7.5. The values for T_{SURF} and h were determined from experimental data using ThermoNet™ as discussed earlier in section 4.3. For the purpose of comparison all of the figures, with the exception of Fig. 7.1, use identically scaled axis where h varies from 3000 to 6000 W/m^2K and the wall superheat varies in the range from 0 to 16 °C.

Figure 7.1 shows two sets of heat transfer coefficient values which correspond to Reynolds numbers of 3801 and 5068. The temperature of the subcooled bulk fluid was 60°C. For the data set corresponding to Re = 5068 the initial value of the heat transfer coefficient was approximately constant at a little over 7000 W/m^2K until the wall superheat reached about 7°C. At this point of the heat transfer coefficient started to increase sharply to 9000 W/m^2K for a wall super heat of 11°C.

During the experimental data collection process the conditions at which bubbles began nucleating on the heater surface were noted. For the previously discussed data set the onset of nucleating boiling (ONB) corresponded to a wall superheat of about 11°C, the same point in which the heat transfer coefficient suddenly increased. This experimentally showed what theory predicts: the onset of nucleating boiling results in a sudden increase in the heat transfer coefficient.

For data set at the lower Reynolds number of 3801 in Fig. 7.1, the initial value for the heat transfer coefficient was lower, in the vicinity of 6000 W/m^{2}K. Though not as apparent as the previous data set, the value for h starts to increase in the region between 9 and 10 °C of wall superheat.

As in Fig. 7.1, two sets of data, corresponding to Reynolds numbers of 1467 and 2934 are presented in Fig 7.2. The bulk water temperature was 70 °C for both sets of data. For the data at the higher Reynolds number, h was initially constant at roughly 4600 W/m^{2}K. However, soon after a wall superheat of 9 °C is reached h quickly jumps to about 5500 W/m^{2}K. Similar to the previous figure, as the Reynolds number is lowered, the heat transfer coefficient also decreases. Unfortunately, for this set of data there is a large gap in the data between 5 and 11 °C which results in a bit of uncertainty. Although, the h value for the two points on either side of the gap is roughly the same, suggesting the heat transfer coefficient was constant across this gap. Assuming a constant h value across the gap in the data, at a wall superheat of 12 °C, h starts to increase, signaling the onset of nucleating boiling.

In the two previous figures, a trend between the required superheat for ONB and the flow rate begins to emerge. In both figures, the data sets with a lower Reynolds number required a higher superheat for ONB. In Fig. 7.1 at a Re = 5068 less than 7 °C of superheat is required for ONB, while for Re = 3801 almost 10 °C is needed. In Fig. 7.2 at Re = 2934 9 °C of superheat is required for ONB, while 12 °C is required for the lower Reynolds number of 1467.

The data sets presented in Figs. 7.3 through 7.5 were taken at the same flow rate (0.106 m/s) as the data set with Re = 1467 in Fig 7.2, (Re is different in the plots due to property variation with temperature) but for different bulk temperature. The data in Fig 7.3 corresponds to a Reynolds number of 1664 and a bulk water temperature of 80°C. Although this data falls in a limited temperature range, it is still consistent with the previously mentioned trend. Even though the data does not show the point at which h increases, it does show that at 11 °C of superheat, h is still constant, suggesting that the onset of nucleating boiling had not yet begun.

The experimental data in Fig. 7.4 is for Re = 1759 and T_{BULK} = 85°C. In this plot the initial data corresponding to the single phase region is a bit scarce. However, the data does show that between approximately 9 and 11 °C wall superheat, h abruptly begins to increase to nearly 5500 W/m^2K at a wall superheat of about 12°C. This again follows the previously mentioned trend.

Figure 7.5, the last in this series of plots, is for T_{BULK} = 90 °C and Re =1856. By comparison this plot is different than many of the previous ones. The value for h is initially in the vicinity of 4300 W/m^2K at a wall superheat of 2 °C and slowly decreases as the wall superheat is increased. At a wall superheat of about 15.6 °C h was equal to about 3800W/m^2K, a reduction of about 500 W/m^2K.

A trend between the required superheat for the onset of nucleate boiling and the bulk water Reynolds number has been observed in the data presented in Figs 7.1 - 7.4. This trend suggests that as the Reynolds number increases the required superheat for ONB decreases. Table 7.1 summarizes the data from the four figures which have lead to the observation of this trend.

Table 7.1 Required superheat for the onset of nucleating boiling.

T_{BULK} °C	u_m m/s	Re	$T_{SURF} - T_{SAT}$ °C
60	0.246	5068	7
60	0.319	3801	9 - 10
70	0.213	2934	9
70	0.106	1467	12
80	0.106	1664	≥ 11
85	0.106	1759	10 - 11

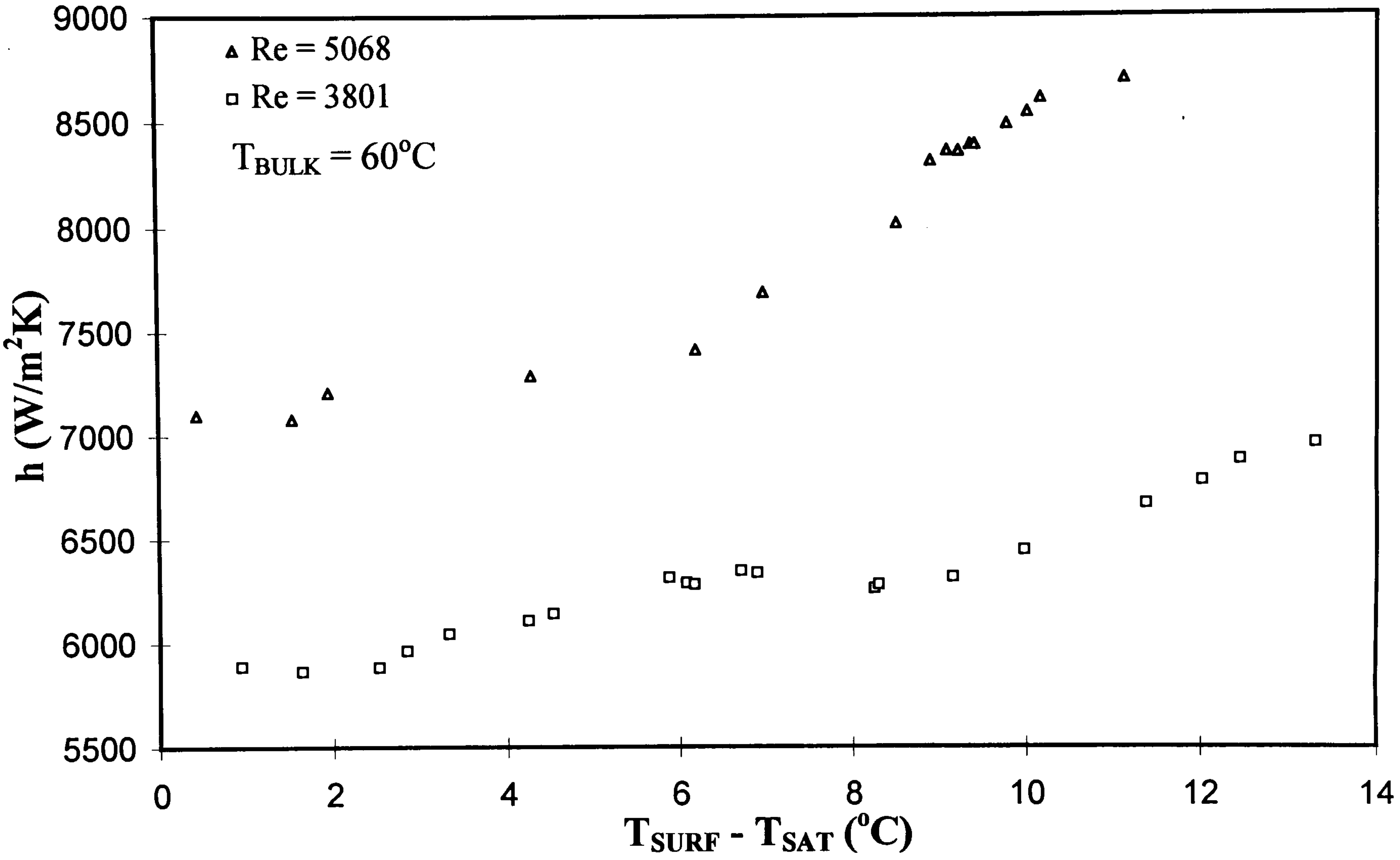

Figure 7.1 Experimentally determined heat transfer coefficient in subcooled flow boiling for TBULK = 60° and Re = 3801 & 5068.

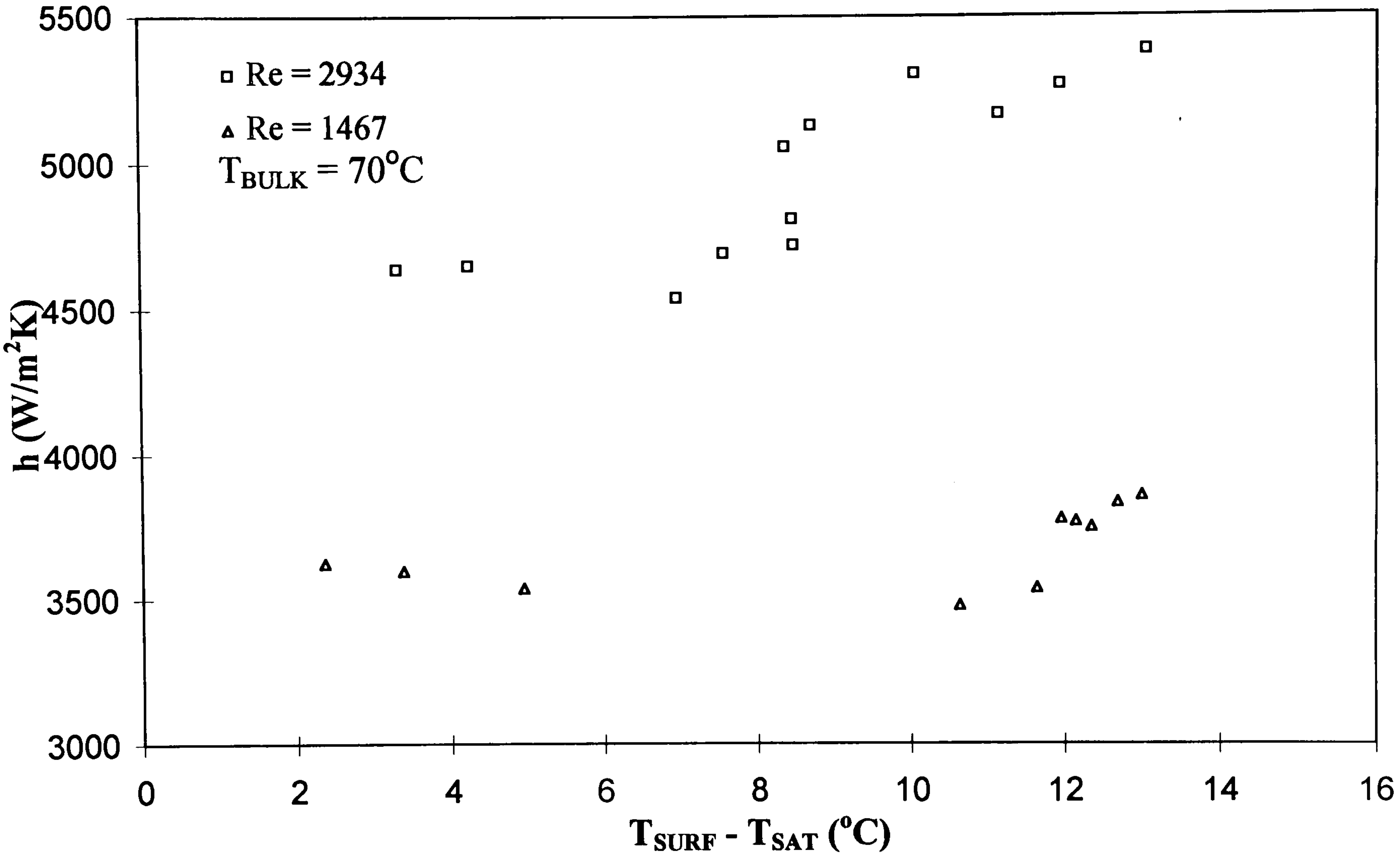

Figure 7.2 Experimentally determined heat transfer coefficient in subcooled flow boiling for TBULK = 70° and Re = 1467 & 2934

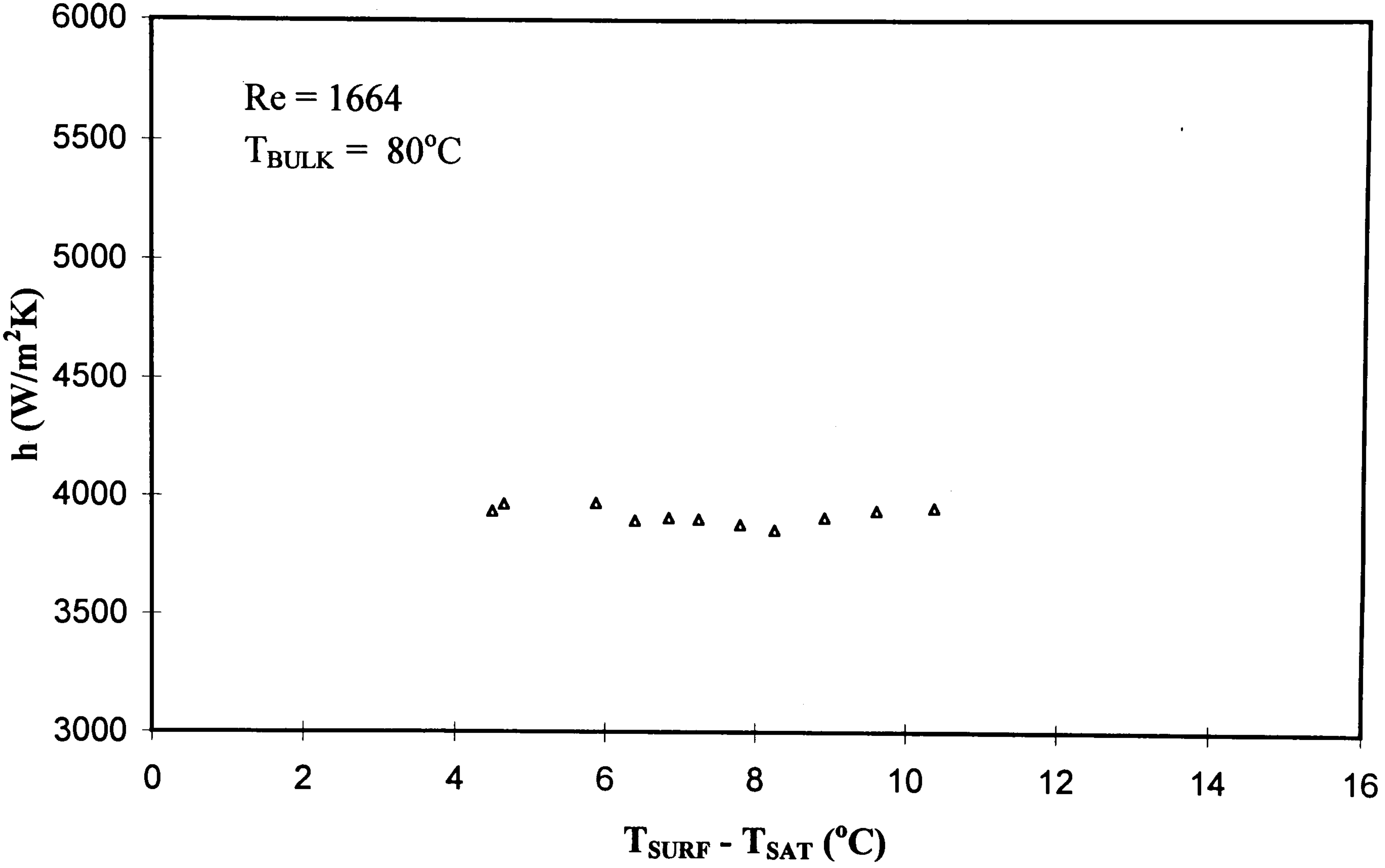

Figure 7.3 Experimentally determined heat transfer coefficient in subcooled flow boiling for TBULK = 80° and Re = 1664.

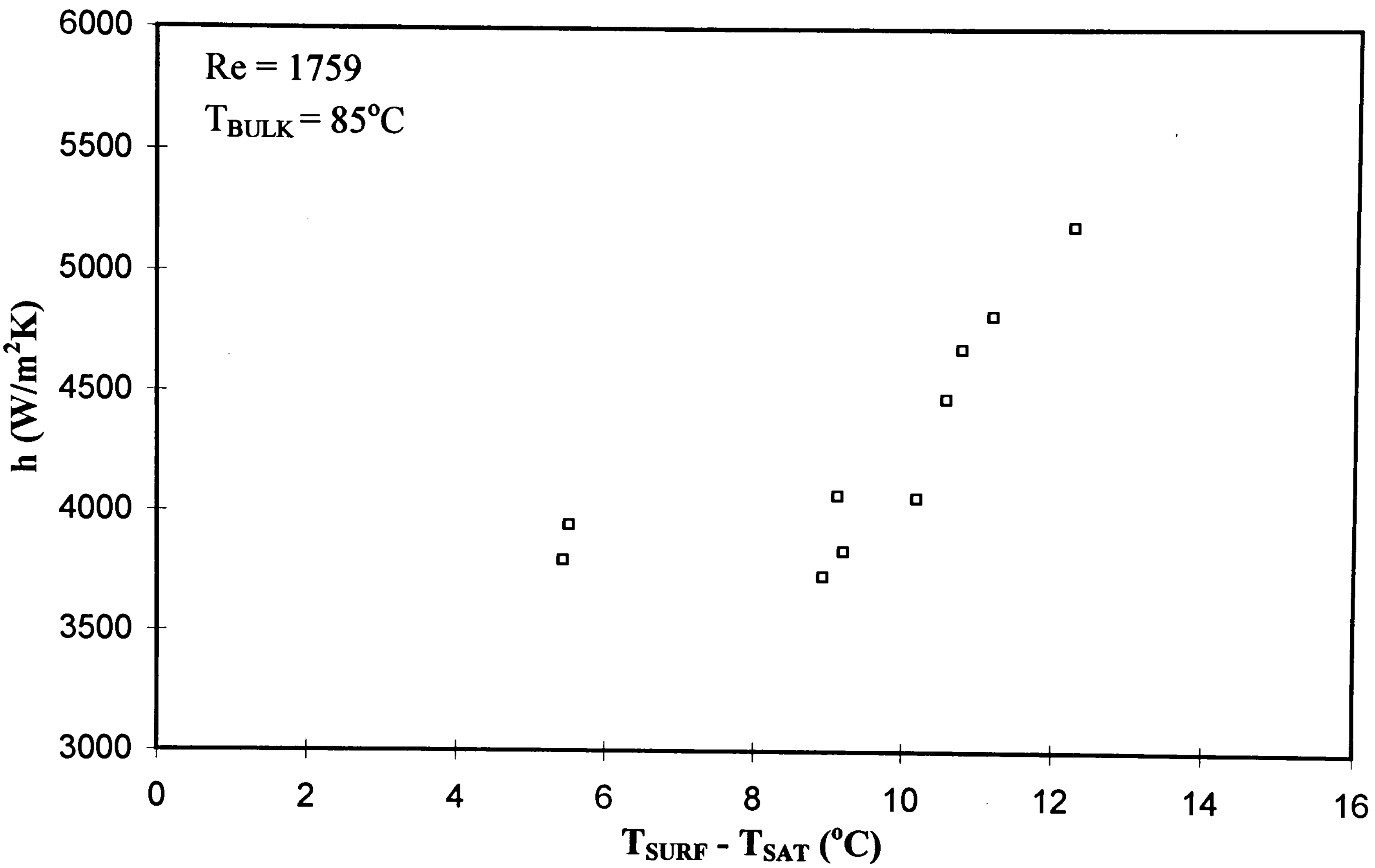

Figure 7.4 Experimentally determined heat transfer coefficient in subcooled flow boiling for TBULK = 85° and Re = 1759.

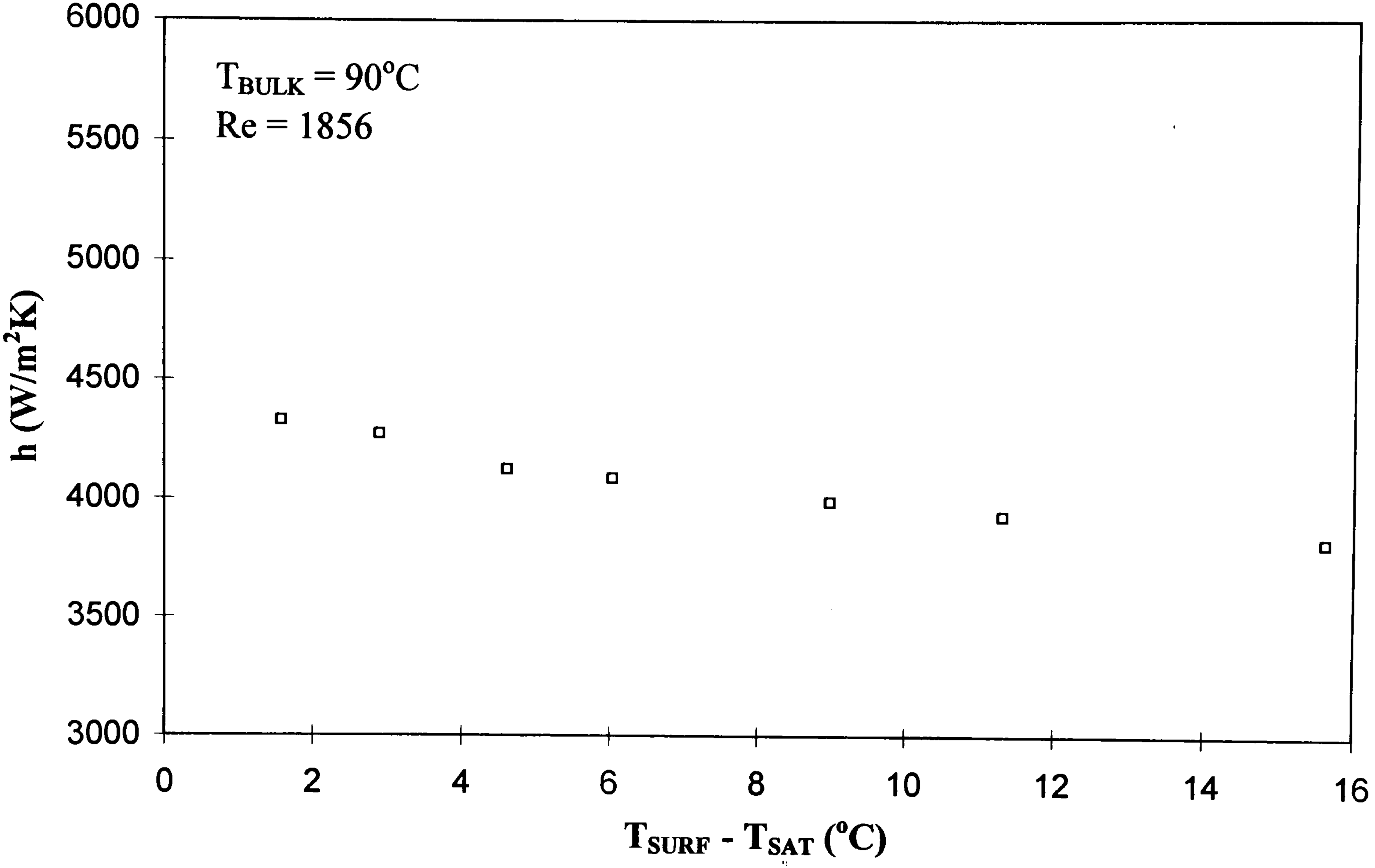

Figure 7.5 Experimentally determined heat transfer coefficient in subcooled flow boiling for TBULK = 90° and Re = 1856.

7.2 Experimentally Determined Nucleating Cavity Radii

In the previous section, the changes in the experimentally determined heat transfer coefficient were studied to identify the initiation of nucleation. In this section, visual techniques were used to identify the initiation of nucleation and measure the size of nucleating cavities.

In the following seven figures (Figs 7.6 - 7.12), the radii of nucleating cavities are plotted versus the corresponding wall superheat values. The bulk temperature of water for these figures varied from 60 to 80°C with Reynolds number in the range of 1447 to 5643, depending on flow rate and bulk water temperature. The axis for the seven plots were again kept the same for ease in comparison. Also included in these plots are the minimum and maximum radius criteria curves for the three different models discussed in the literature review (Eq. 3.37, 3.38, and 3.40), as well as the proposed stagnation/truncated model that was developed in Chapter 5 (Eq. 5.9). The addition of these curves will allow for a direct comparison between the experimental data and the four bubble nucleation criteria models.

Figures 7.6 through 7.8 shows the active cavities for a constant bulk temperature of water equal to 60°C and three flow rates corresponding to Re = 2840, 3801, and 5068. In Fig 7.6, data was taken at three heater steady state conditions corresponding to wall superheats of approximately 5, 6, and 9°C. For each condition multiple active cavities were seen and recorded using the high-speed camera. Later using a normal VCR, the images recorded at high-speed could be played back at a much slower rate allowing for cavity radii measurements (see section 4.2 on Experimental Procedure). For this flow rate a wide range of active cavities, 5 - 14 μm radii, were observed at wall superheats in the range of approximately 6 - 8 °C.

In Fig. 7.7 the data was taken for Re = 3801. The observed nucleating cavity radii were much smaller than those presented in Fig 7.6, and over a much smaller range, 2.5 - 6μm. For these cavities the wall superheat was over a wide range, approximately 3 - 7 °C, similar to the superheat of nucleating cavities in Fig 7.6. As the flow rate was increased further, Re = 5068 (Fig 7.8), the observed nucleation cavity radii seemed to become even smaller, in the range of 2 - 4 μm, while the required wall super heat tended to increase to between 9 and 10 °C.

The four curves corresponding to the different bubble nucleation models (Hsu (1962), Bergles and Rohsenow (1964), Davis and Anderson (1966) and the proposed stagnation/truncated model) predicted the allowable range of maximum and minimum cavity radius at a given wall superheat. Therefore, if an experimental data point lay above the curve, it was within the predicted range, but if the point lay below the curve it would be outside of the predicted range. A few general comments about the different models with respect to each other are that all four models predict almost an identically vertical curve for $r_{c,min}$ (the left portion of the curves) at high superheats, but start to vary noticeably as the superheat is decreased. In the region of $r_{c,max}$ (the right portion of the curves) the curves flatten and all four models vary significantly. As seen in all seven of the plots, because of the different bubble geometry assumptions, the predicted region of active cavities is consistently different for each model. In almost every plot Davis and Anderson's model predicts the most confined region while Bergles and Rohsenow's model allows for the largest region of active cavities.

For Fig. 7.8 all four models worked equally well in predicting the range of active cavities, all data points were within the predicted range of all four models. However, in Figs 7.6 and 7.7 this was not the case. In both cases the majority of the data falls outside of the predicted range for Hsu's and Davis and Anderson's models. About half the data points in each figure falls in the predicted range of the proposed stagnation/truncated model, while almost all of the experimental data falls within the range predicted by Bergles and Rohsenow's model.

The data presented in Figs. 7.9 and 7.10 were taken at the same flow rate, but different bulk temperature. In both figures the observed active cavities are much larger than those shown in the two previous figures. In Fig. 7.9 four active cavities in the range of 11 to 16 μm were observed at a relatively high superheat, approximately 12 °C. These four data points fall in the predicted range of all four bubble nucleation models.

For the data in Fig. 7.10 the bulk water temperature was slightly higher than that in Fig. 7.9, 75 °C as opposed to 70 °C. The cavity radius sizes were generally the same as those nucleating in slightly cooler bulk water, but the wall superheat was considerably lower, in the range of 4 to 8° C. From the plot it can be seen that for this experimental data Bergles and Rohsenow's model works well in predicting the range of nucleating cavities. The proposed model also does a good job, with most data points falling within the predicted range, and two data points lying just outside.

Figure 7.11 shows data with a bulk temperature of 75°C, the same as the data shown in Fig. 7.10, only at a much higher flow rate, Re =5643. For this flow condition only one heater steady state condition was recorded for which active cavities could be observed. This condition corresponded to a wall superheat of about 9°C. As seen in the plot, a large range of cavities were active. Again, in this figure Bergles and Rohsenow's model works well in predicting the range of nucleating cavities, while only two points lie outside of the range predicted by the proposed model.

In Figure 7.12 two sets of cavity radius data corresponding to Reynolds numbers of 1664 and 1779 and a bulk water temperature of 80 °C are presented. The flow rate for the two data sets was not too far apart. The data in this figure was quite scattered. For the data set with the slightly higher flow rate, the active cavity radii fell in the range of 1 - 16 μm with wall superheats between 3 and 13 °C. For the slightly lower flow rate, the data was located over a smaller range. The active cavity radii varied between 4 and 8 μm, while the wall superheat was between 4 and 10 °C. In Fig 7.12 all four models worked well in predicting a range for nucleating, while Bergles and Rohsenow's and the proposed stagnation/truncated models seemed to work the best.

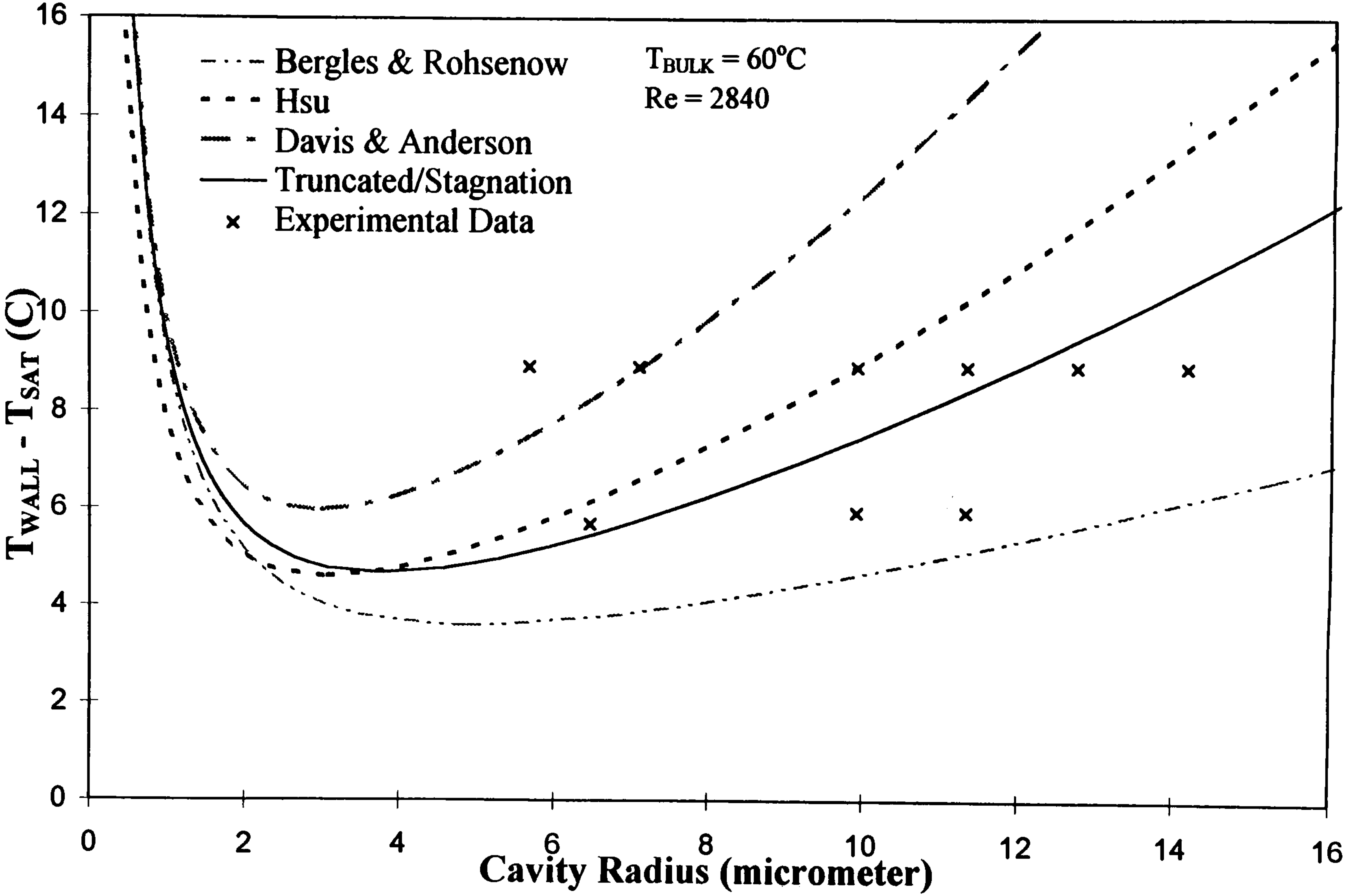

Figure 7.6 Criteria for Onset of Nucleate Boiling for $T_{BULK} = 60°C$ and Re = 2840.

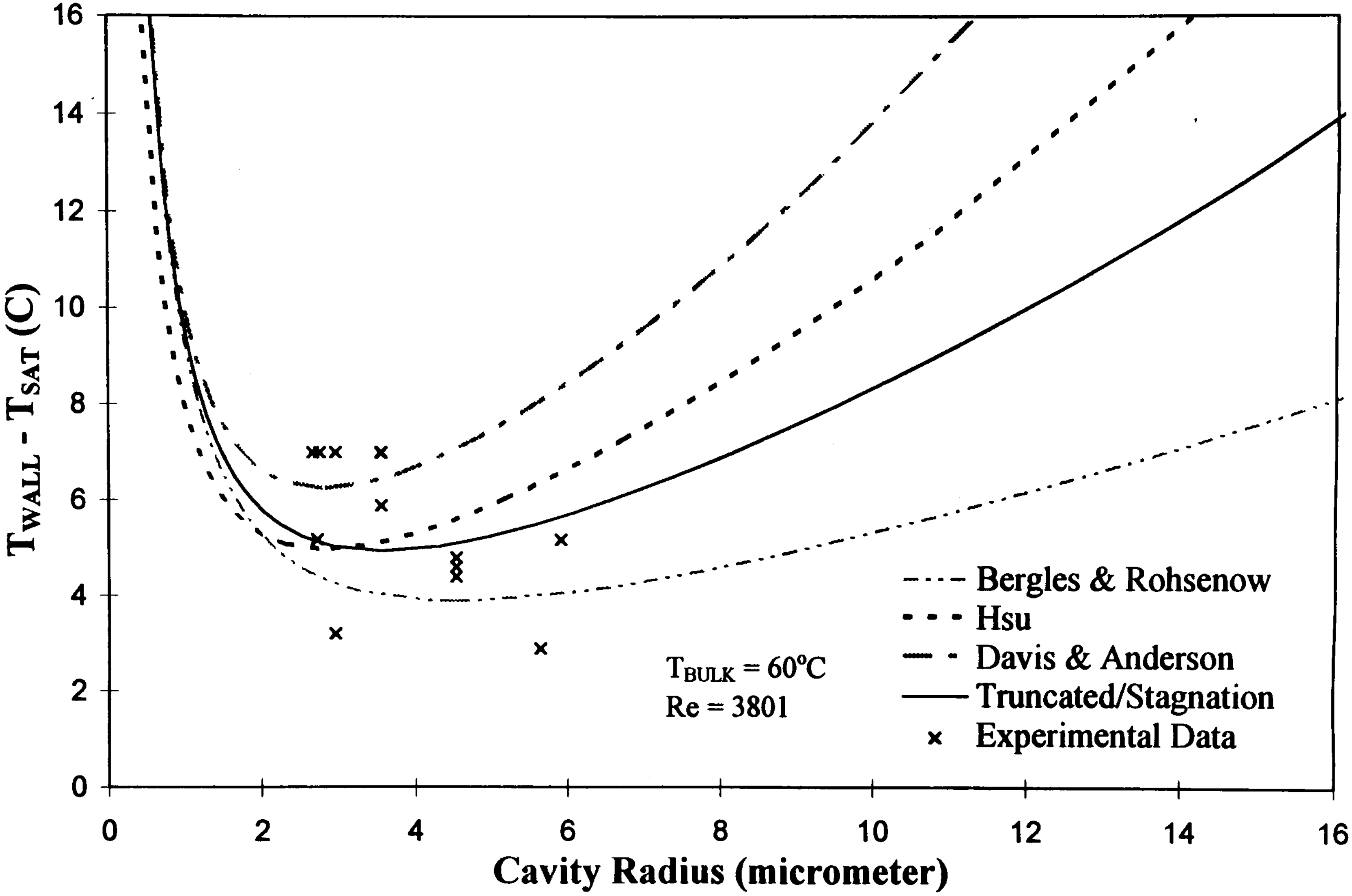

Figure 7.7 Criteria for Onset of Nucleate Boiling for T_{BULK} = 60°C and Re = 3801.

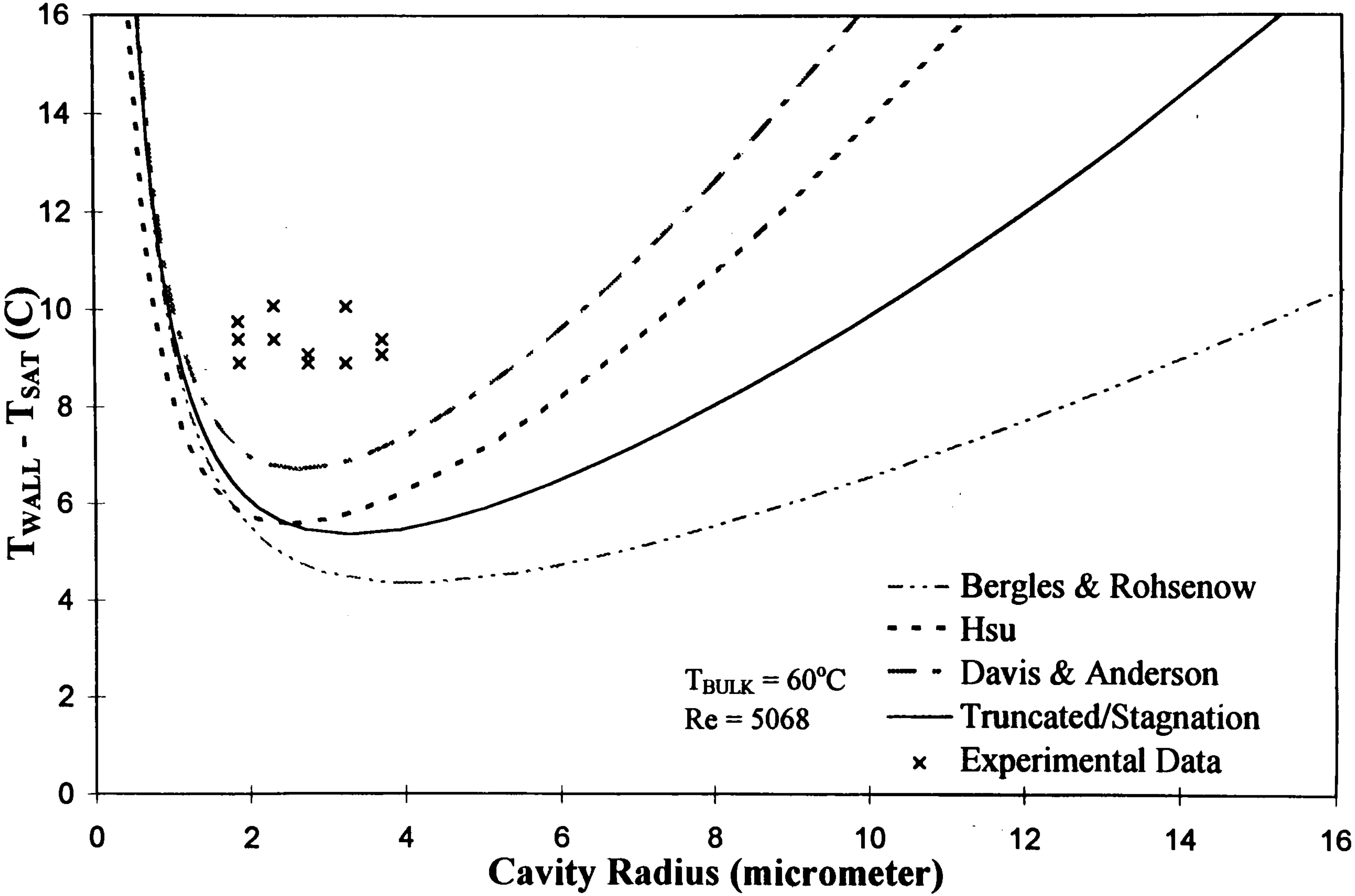

Figure 7.8 Criteria for Onset of Nucleate Boiling for T_{BULK} = 60°C and Re = 5068.

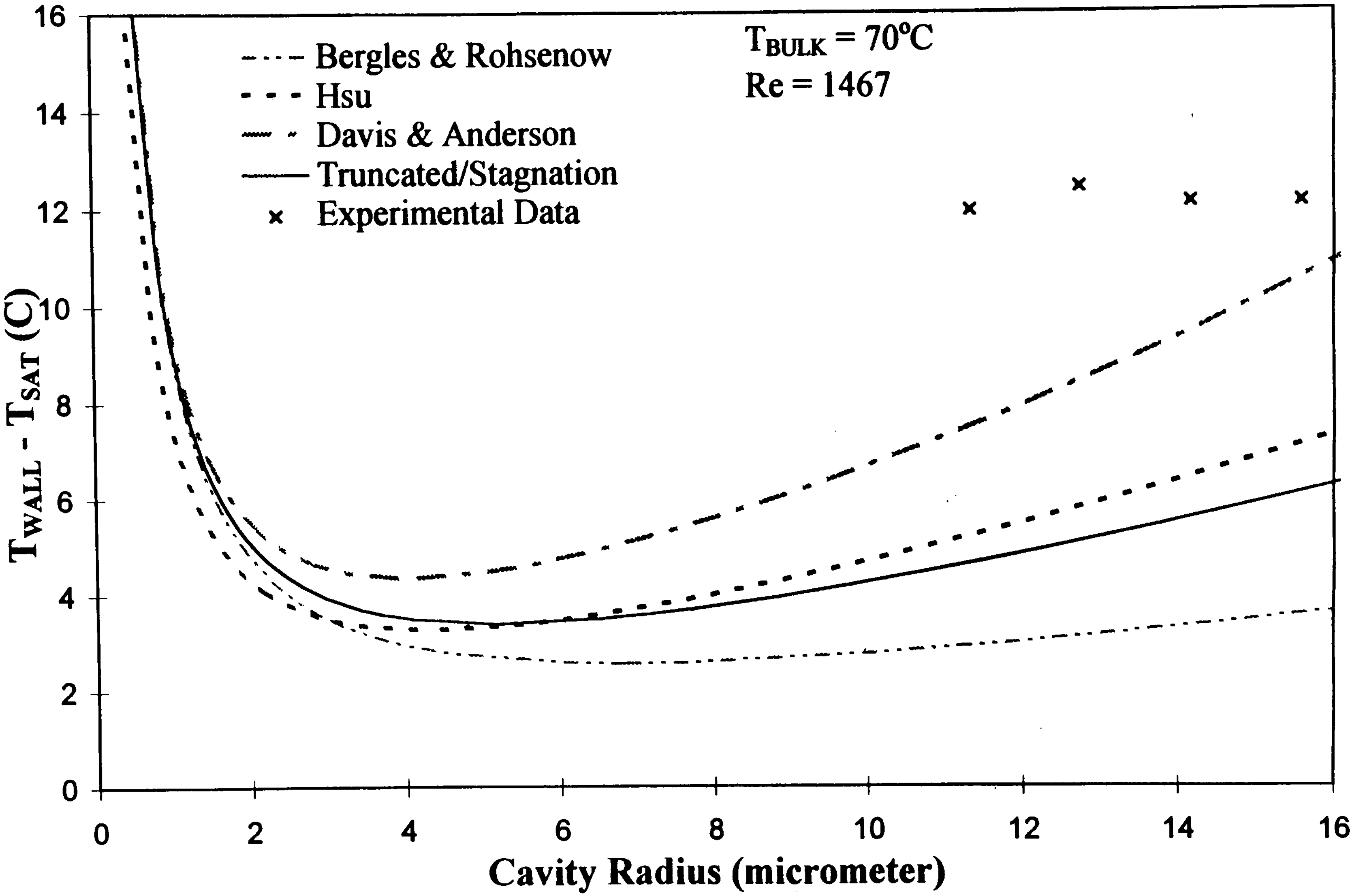

Figure 7.9 Criteria for Onset of Nucleate Boiling for T_{BULK} = 70°C and Re = 1467.

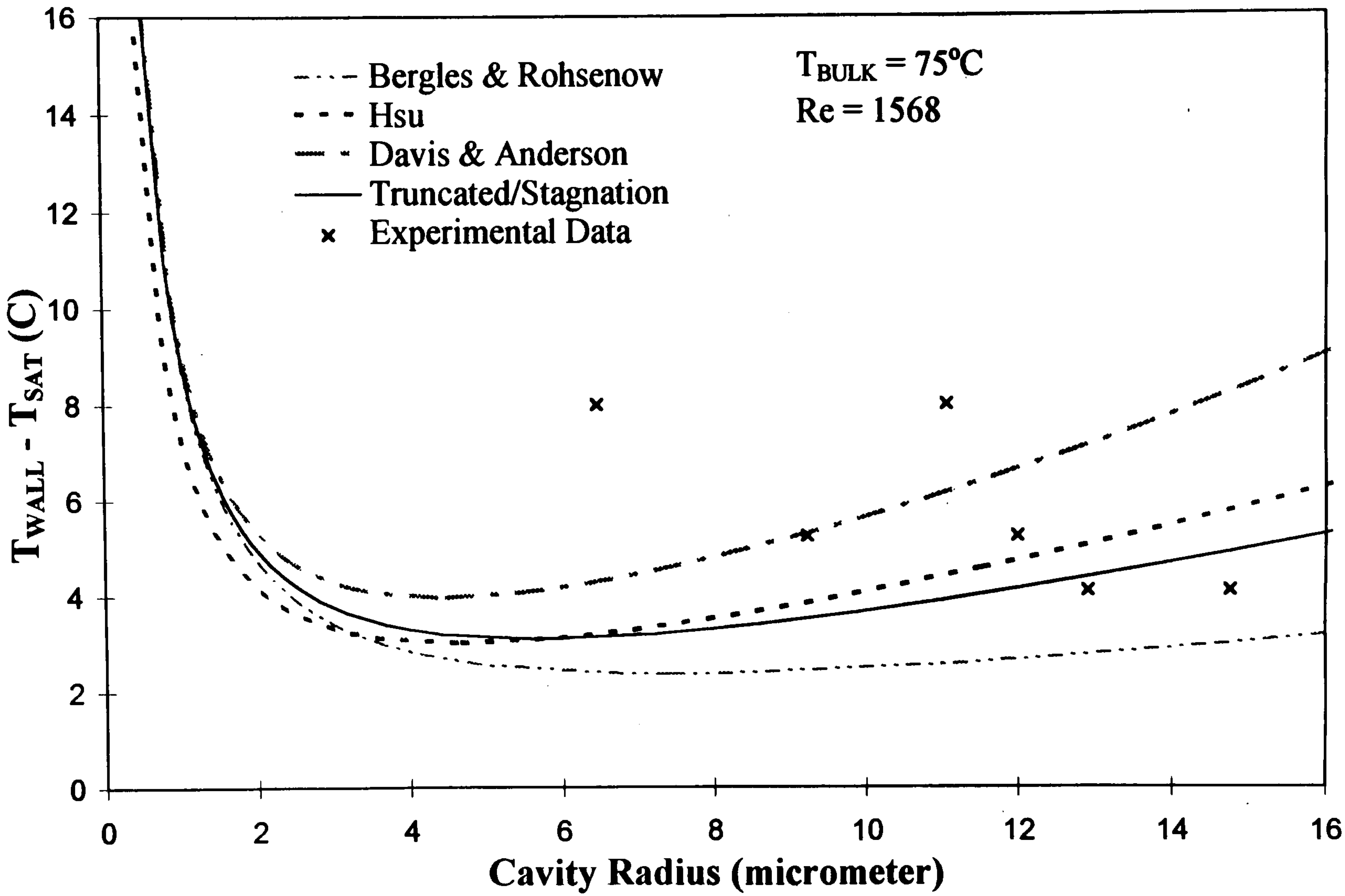

Figure 7.10 Criteria for Onset of Nucleate Boiling for T_{BULK} = 75°C and Re = 1568.

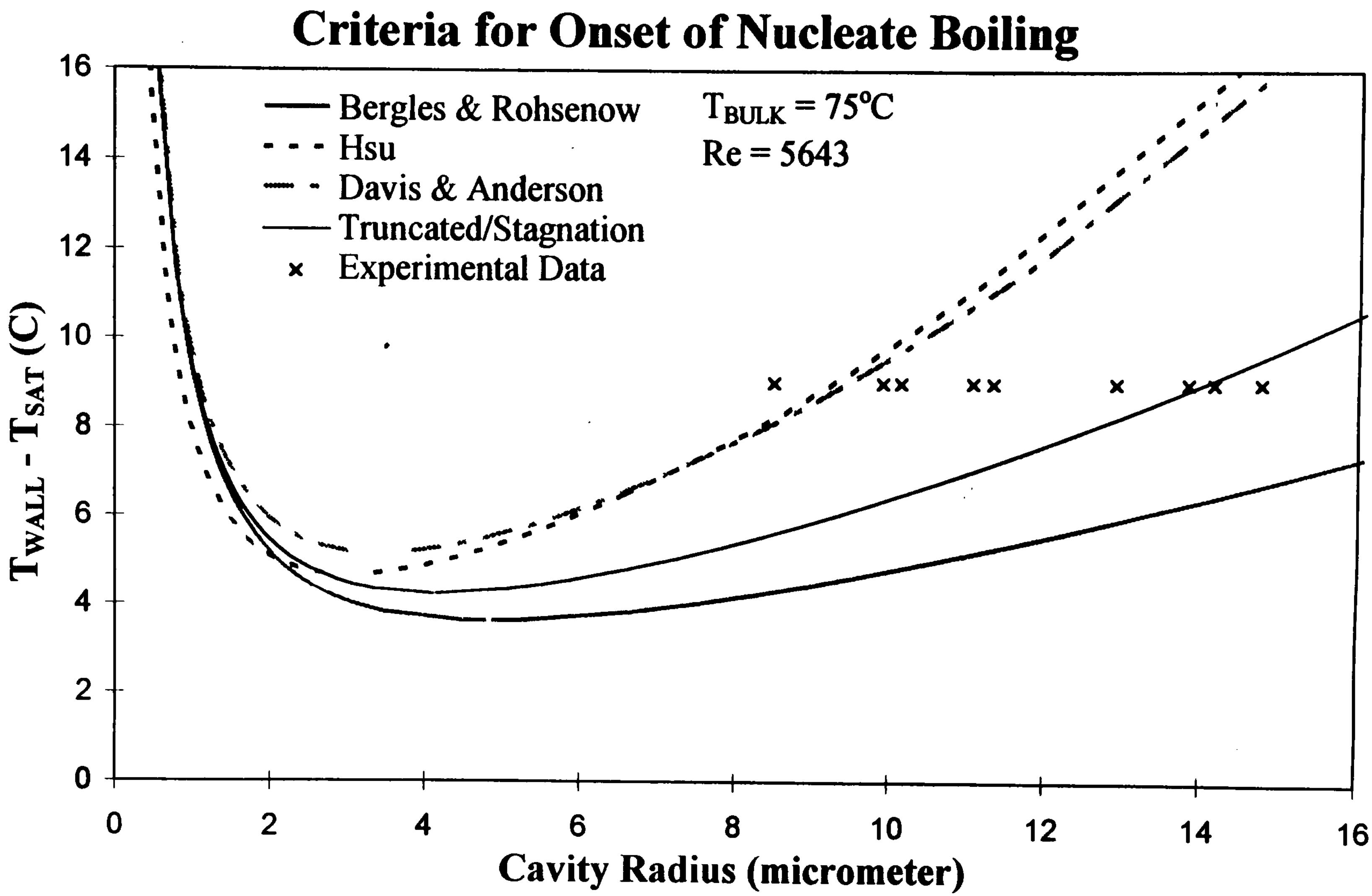

Figure 7.11 Criteria for Onset of Nucleate Boiling for T_{BULK} = 75°C and Re = 5643.

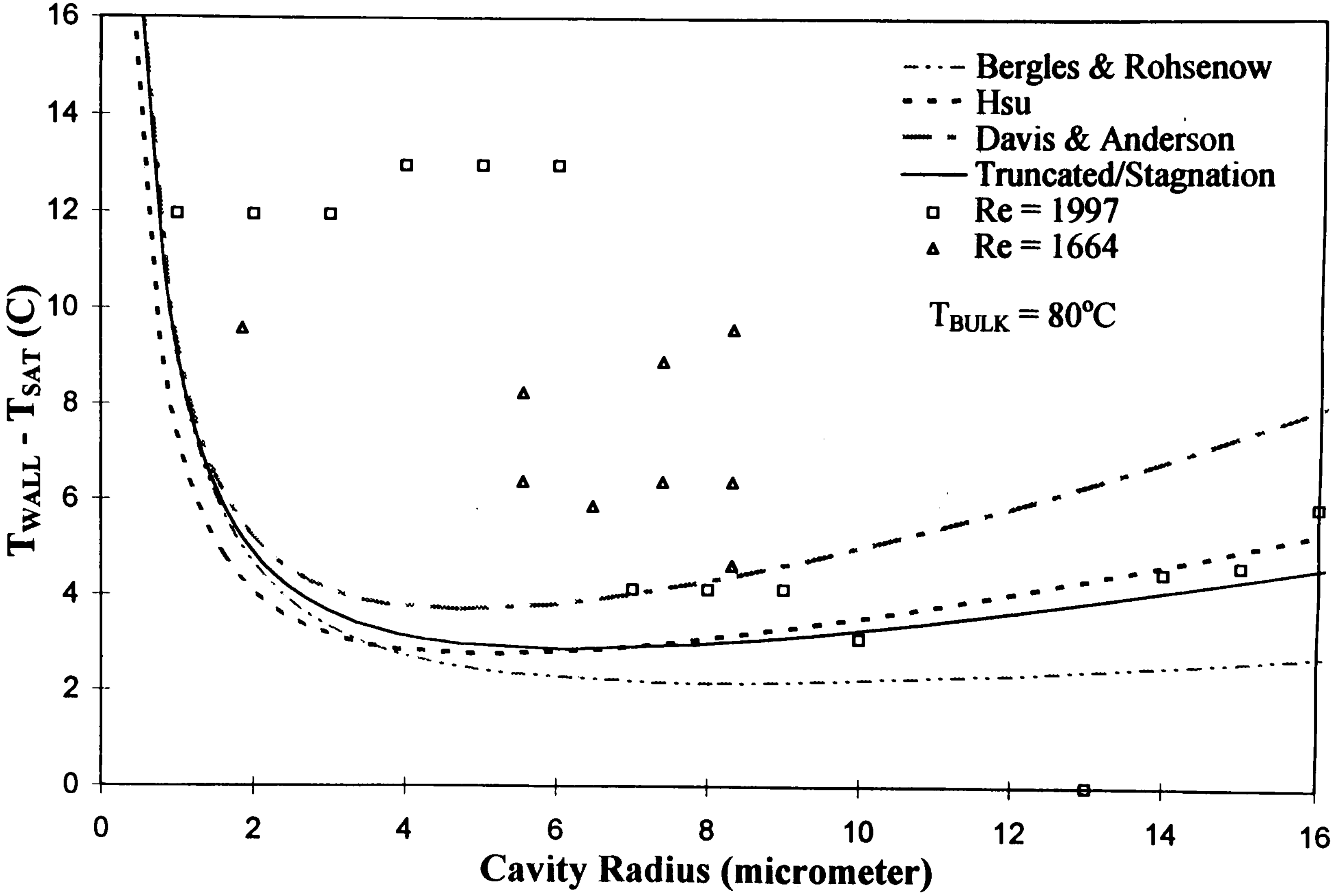

Figure 7.12 Criteria for Onset of Nucleate Boiling for T_{BULK} = 80°C and Re = 1664-1997.

7.3 Summary of Results

In section 7.1 the changes in the experimentally determined heat transfer coefficient were studied to identify the initiation of nucleation. From this investigation a trend between the flow rate and wall superheat required for the onset of nucleate boiling was observed. In this trend increasing flow rate required a smaller superheat to activate cavities, as shown previously in Table 7.1. An explanation to this trend is well illustrated in Fig 7.13. As the flow rate of the bulk fluid increases the bubble size tends to decrease (see Mizo (1995). For a bigger bubble, the height of the stagnation streamline, y_s, will be higher than that for the smaller bubble. As shown in Fig 7.13, in order to have the linear temperature profiles intersect the line representing the saturation temperature, T_{SAT}, at a height of y_s, the wall temperature corresponding to the big bubble must be greater than that for the smaller bubble. This then results in a higher required superheat (T_w-T_{SAT}) for the bigger bubble, or lower bulk fluid flow rate.

In section 7.2 the initiation of nucleation was studied visually, and the experimentally determined data for active cavities was compared with the four bubble nucleation models discussed earlier.

An overall summary for the four bubble nucleation models was that Bergles and Rohsenow's model predicted a range of active cavity radii that almost always included the experimental data. The proposed stagnation/truncated model also worked well in predicting a cavity radii range that included the experimental data, with the exception of Figs 7.6 and 7.7. The other two model, Hsu (1962) and Davis and Anderson (1966), predicted smaller regions of possible active cavity radii, and thus were less successful in including the experimental data within their predicted range.

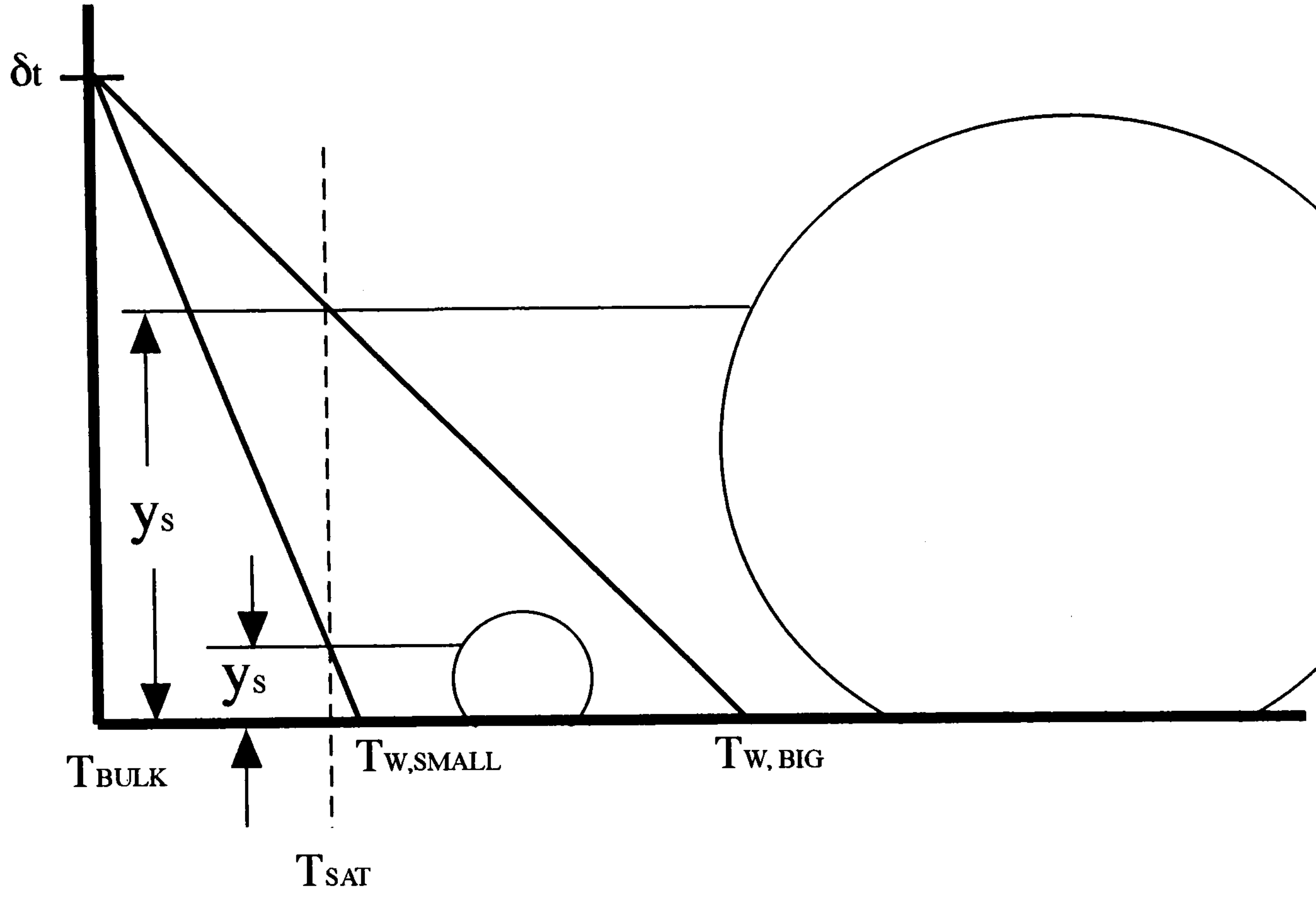

Figure 7.13 Illustration of the effect of bubble height on required superheat for the onset of nucleation.

An important goal of the current work was to show that by developing a model which incorporated geometric characteristics of actual bubbles seen in the experimental investigation the required criteria for the onset of nucleate boiling could be predicted more accurately. In part this goal has been met, the proposed model predicts a range in which most of the experimental data falls An important point that should be made is that this model is based on the thermal boundary layer thickness, δ_t, and the bubble contact angle, β, which varies for each bubble and corresponding thermal-flow condition. The curves included in Figs. 7.6-7.12 are based on the average β and δ_t for many bubbles and a given flow rate. Most likely, if an individual cavity and the associated nucleating bubble with corresponding β and δ_t were used instead of averaged values, the model would be even more accurate. However, it would be unrealistic and impractical to make separate plots for each individual data point. Therefore, the average values were used instead.

8. REFERENCES

Bankoff, S.G., 1957, Ebullition from solid surfaces in the absence of pre-existing gaseous phase, *Trans. ASME,* vol. 79, pp. 735-740.

Bergles, A.E, and Rohsenow, W.M., 1964, "The Determination of Forced-Convection Surface Boiling Heat Transfer," Journal of Heat Transfer, Vol. 86, pp. 365-372.

Brock, J.R. and Baird, R.B., Surface Tension and the Principle of Corresponding States, *AIChE J.*, vol. 1 pp 174-184, 1955.

Carey, V.P., 1992, Liquid-Vapor Phase Change Phenomen, Taylor & Francis, Bristol, PA.

Cooper, M.G., Mori, K., and Stone, C.R., 1983, "Behavior of Vapor Bubbles Growing at a Wall with Forced Flow," *International Journal of Heat and Mass Transfer*, Vol. 26, No. 10, pp. 1489-1507.

Davis, E.J.,and Anderson, G. H., 1966, "The incepience of Nucleate Boiling in Forced Convection Flow" A.I.Ch.E. Journal, Vol. 12, pp. 774-780

Hsu, Y.Y., 1962, "On the Size Range of Active Nucleation Cavities on a Heating Surface," Journal of Heat Transfer, Vol. 84, pp. 207-216.

Incropera, F.P., and Dewitt, D.P., 1990, Fundamentals of Heat and Mass Transfer, Third Edition, John Wiley and Sons, New York.

Jasper, J.J., The surface tension of pure liquid components, *J.Phys. Chem. Ref. Data*. vol. 4, pp 841-1010, 1972.

Kandlikar, S.G., 1994, "Measurement of Departure Bubble Diameter and Advancing and Receding Contact Angles in Subcooled Flow Boiling of Water," Paper presented at the joint ASME and ISME Conference, BARC, Bombay.

Kandlikar, S.G., 1992, "Bubble Behavior and Departure Bubble Diameter of Bubbles Generated over Nucleating Cavities in Flow Boiling," Paper presented at the Conference on Pool and External Flow Boiling, Santa Barbara.

Kandlikar, S.G., Mizo, V.R., and Cartwright, M.D., "Investigation of Bubble Departure Mechanism in Flow Boiling using High-speed Photography," Proceedings of International Conference on Convective Flow Boiling, ASME Foundation Conference, Banff, Canada, April 30-May 5.

Kandlikar, S.G., 1990, "A Mechanistic Model for Flow Boiling Heat Transfer," Paper presented at the 1990 ASME Winter Annual Meeting, Dallas, Nov., 1990.

Kandlikar, S.G., 1992,"Bubble Behavior and Departure Bubble Diameter of Bubbles Generated Over Nucleating Cavities in Flow Boiling," Pool and External Flow Boiling, Proceedings of The Engineering Foundation Conference on Pool and External Flow Boiling, March 22-27, ASME.

Kandlikar, S.G., Cartwright, M.D., and Mizo V.C., 1995, "A Photographic Study of Nucleation Characteristics of Cavities in Flow Boiling," Proceedings of International Conference on Convective Flow Boiling, ASME Foundation Conference, Banff, Canada, April 30-May 5.

Kandlikar, S.G., and Stumm B.J., 1993, "A Control Volume Approach for Investigating Forces on a Departing Bubble under Subcooled Flow Boiling," ASME National Heat Transfer Conference, Colorado Springs. Also accepted for publication in Journal of Heat Transfer.

Kenning, D. B. R. and Cooper, M. G., 1966,"Flow patterns near nuclei and the the initiation of boiling during forced convection heat transfer," Paper 11 presented at the Symposium on Boiling Heat Transfer in Steam Generating UNits and Heat Exchangers held in Manchester, IMechE (London), pp 15-16.

Lorenz, J.J., Mikic, B.B., and Rohsenow, W. M., 1974, " The Effects of Surface Condition on

Boiling Characteristics," Proc. Fifth Int. Heat Transfer Conf., vol. IV, pp. 35-39

Mizo, V.R., 1995, "Investigation of Bubble Departure Mechanism in Flow Boiling using High-speed Photography," Masters Thesis, Mechanical Engineering Dept., RIT

Nukiyama, S., 1934, "The Maximum and Minimum Values of Heat q Transmitted from Metal Surface to Boiling Water under Atmospheric Pressure," Journal of Society of Mechanical Engineers (Japan), Vol. 37, pp. 367-374, 553-554.

Plateau. Static experimentale et therorique des Liquides soumis aux seules Forces moleculaires. 1873.

Pohlhausen, E., 1921, Der Warmeaustauch Zwishen Festen Korpern und Flussigkeiten mit kleiner Treibung und Warmeleitung, *Z. Angew. Math. Mech.*, vol 1, pp. 115-121.

APPENDIX A

A.1 Surface Tension - Definition and Experimental Results

The fundamental of liquid surfaces is that they tend to contract to the smallest possible area. This tendency is shown in the spherical form of small drops of liquid, in the tension exerted by soap films as they tend to become lass extended, and in many other properties of liquid surfaces. Plateau (1873) had undertaken a prolonged study of the forms assumed by the liquid surfaces, under conditions when the disturbing effect of gravity is absent; he showed that the surfaces always assume a curvature such that, if R_1 and R_2 are the principal radii of curvature at any point,

$$1/R_1 + 1/R_2 = \text{constant}. \tag{A.1}$$

It is a geometrical fact that surfaces for which the relation (A.1) holds are surfaces of minimum area.

The simplest properties of molecules in liquids suffice to account for this tendency of the surface to contract. Molecules are small objects, possessing definite size and shape, in all states of matter; in all fluids they are free to move relative to one another, and in liquids they are kept close to each other by the cohesion forces between them. Liquids are thus distinguished from solids by their fluidity, that is, the freedom of the molecules to move. They are distinguished from gases by the fact that the attraction between the molecules restrains the motion sufficiently to prevent more than a small portion of the molecules escaping into vapor. Translatory and rotary motions go on within the liquid with considerable freedom.

In the interior each molecule is surrounded by others on every side. Therefore, it is subject to attraction in all directions. On the average, over period of time, long compared to the molecular vibrations, the attraction on any molecule is uniform in all directions. At the surface, however, conditions are entirely different. Molecules at the surface are attracted inwards, and to each side by its neighbors, but there is no outward attraction to balance the inward pull, because there are very few molecules outside. Hence, every surface molecule is subject to a strong inward attraction, perpendicular to the surface.

This inward attraction causes the surface to diminish in area, because the surface molecules are continually moving inwards more rapidly than the others move outwards to take their places. the number of molecules in the surface is therefore continually diminishing and the contraction of the surface continues until the maximum possible number of molecules are in the interior, i.e. until the surface is the smallest possible for a given volume, subject to the external conditions or forces acting on the drop.

The fact that a liquid surface contracts spontaneously shows that there is free energy associated with it, that work must be done to extend the surface. The origin of this work, in terms of the molecules, is that when the surface is extended molecules must be brought from then interior to the surface against the inward attractive forces. Work must be done against these inward attractive forces for each molecule that is brought to the surface. Since the molecules have a definite size, there will always be a definite number of them in the surface. Provided the surface is of the same nature and structure everywhere, the work done in extending it will be definite.

This free energy in the surface is of fundamental importance. A vast number of problems relating to the equilibrium of the surface can be solved without knowing more than the magnitude of this free energy. In the solution of such problems, a mathematical device is almost invariably employed to simplify the calculations; it is to substitute for the surface free energy a hypothetical tension, acting in all directions parallel to the surface, equal to the free surface energy. This is what is generally known as the *surface tension.* It is always mathematically possible to replace a free energy per unit area of surface by a tension acting parallel to the surface. Such a surface tension has the same dimension as a surface energy (mass/time^2) and it must have the same numerical magnitude.

This substitution of a tension for a free energy per unit area is the converse of the mathematical method of 'virtual work' often used in statics. There the calculations are often simplified by considering the energy changes involved in a slight displacement of the system, adding all together, and finally equating of the energy changes to zero, to obtain the condition of equilibrium. In systems involving liquid surfaces, the equilibrium could be obtained by adding up the changes in surface energy in the various surfaces whose area is altered during displacement. It is, however, simpler to pay no attention to these changes in area directly, but to consider the surfaces which depend solely on the existence of this free surface energy. Surface free energy, due to the inward pull on the molecules on the surface, is the fundamental property of surfaces. Surface tension can be simply taken as its equivalent.

Surface tension values are influenced by two important factors. These two factors are fluid temperature and presence of contaminants.

A.1.1 Influence of Temperature on Surface Tension

The kinetic agitation of the molecules and the tendency of the molecules to fly outwards increases as the temperature rises; consequently the net inward pull may be expected to become less, even if the real cohesion remains unchanged by the temperature. In fact, the surface tension almost invariably decreases with rising temperature, the only known exceptions being with a few substances over a restricted range of temperature. As temperature rises towards the critical, the restraining force on the surface molecules diminishes and vapor pressure increases: when the critical temperature is met the surface tension vanishes all together. "Negative surface tension" is impossible for a liquid: it would only occur when the liquid temperature rises above its critical temperature, where the liquid can not exist.

The temperature dependency of surface tension is often the basis for interpolation schemes and curve-fit equations used to predict the variation of surface tension with temperature. For example, the surface tension of water can be computed from the correlation:

$$\sigma = 235.8(1-T_{sat}/T_c)^{1.256}[1-0.625(1- T_{sat}/T_c)] \qquad \text{(A. 2)}$$

where both T_{sat} and T_c are in Kelvin and σ is in millinewtons per meter.

In the case of most liquids the relationship between surface tension and temperature is nearly linear. Jasper (1972) fit a linear relationship of the form

$$\sigma = C_0 - C_1T \qquad \text{(A.3)}$$

to surface tension data for a wide variety of pure liquids over a given temperature range, where T is in degree Celsius. Table 1 (Carey 1992) lists the constants C_0 and C_1 for a variety of different liquids. Figure A.1 shows the variation of surface tension with temperature based on equations (A.2) and (A.3) in the temperature range of 0-100°C.

where T_b is the normal boiling temperature of the liquid (at atmospheric pressure).

Using Eqs. A.4 and A.6 together, it is possible to estimate the variation of surface tension with temperature from critical data and the normal boiling point. This method works good for a wide variety of simple organic compounds, but is not intended for light molecules, highly polar inorganic substances, or associated substances such as alcohols and liquid metals.

A.1.2 Effects of Contamination on Surface Tension

The second major factor affecting surface tension is the presence of one or more substances dissolved in the fluid. From thermodynamic analysis of the liquid-vapor interfacial region for a binary mixture, in which A is a solute exhibiting ideal mixture behavior in solvent B, it can be shown that the surface excess mass of species A is related to the variation of σ with concentration as

$$\Gamma_A = -(x_A/RT)(\partial\sigma/\partial x_A)_T \qquad (A.7)$$

In this equation, x_A is the concentration of the solute species A.

Some surface-active materials are so highly enriched at the interface that they are termed surface agent or surfactants. Since they concentrate so highly at the interface, the presence of material of this type even in very low concentrations may significantly alter the interfacial tension.

Equation A.7 may also be interpreted in a converse manner, such that A accumulates at the interface, so that $\Gamma_A > 0$; then $(\partial\sigma/\partial x_A)$ is negative and the presence of the surface-active material decreases the surface tension. This is the case with a typical

A.1.3 Classification of the methods of measuring surface tension:

Surface tension measurement techniques can be classified into two categories: static and dynamic methods. The static method measures the tension of practically stationary surfaces which have been formed for an appreciable time, and depend on one of two principles. The most accurate depend on pressure difference set up on the two sides of a curved surface possessing surface tension; these include the capillary height method with its many variations, the maximum bubble pressure method, the drop-volume method, and the method of sessile drop.

A.1.3.1 Static Methods -Capillary height Method

Capillarity occurs when a free surface of liquid in a small tubes or porous media will rise or fall satisfying the Young-Laplace equation:

$$P_{II} = P_{inside} - P_{outside} = 2\sigma/r \qquad \text{(A.8)}$$

Consider a small tube of radius r_i shown in Figure A.3. The tube contains liquid with a free surface, and is in contact with an extensive pool of liquid. The liquid is assumed to meet the wall at an angle $\theta < 90°$. When $r_i << L_c$, where L_c is defined as follows,

$$[2\sigma(1 - \sin\theta)/((\rho_l - \rho_v)g)]^{1/2} \qquad \text{(A.9)}$$

and the radius of curvature of the interface is approximately uniform and equal to $r_i/\cos\theta$. For small radius of curvature in the meniscus, the Young-Laplace equation requires large jumps in pressure across the interface. This difference supports a large column of liquid against gravity.

The equipment used to perform this method was quite simple a
3.810 mm diameter glass tube, an accurate scale, and a water conta
temperature bath was used to increase the water temperature up to 70°
the meniscus in the tube, and the angle of contact were measured and
(A.12) the surface temperature of the water was determined.

- Results

The obtained surface tension values corresponding to the respectiv
were plotted on Figure A.1. A very good fit with the actual correlation was
the majority of the points falling in the +/- 5% accuracy bend.

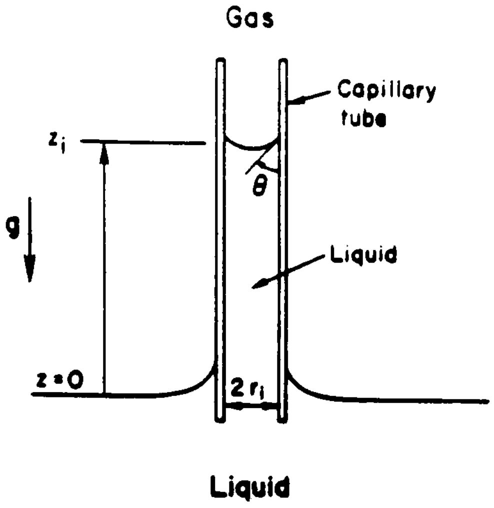

Figure A.3. Rise of a wetting liquid in a capillary tube

Combining the Young -Laplace equation with the hydrostatic pressure variance in the fluid, the condition for equilibrium is:

$$P_I - P_{II} = (\rho_l - \rho_v)gz_i = 2\sigma \cos \theta / r_i \tag{A.10}$$

This equation can be solved for the equilibrium height of the liquid column, z_i:

$$z_i = 2\sigma \cos \theta / (\rho_l - \rho_v) g r_i \tag{A.11}$$

or the surface tension, σ :

$$\sigma = r_i z_i (\rho_l - \rho_v) g / 2 \cos\theta \tag{A.12}$$

Knowing this, the surface tension of a liquid can be easily determined using basic experimental methods. In this case a piece of glass tube, container of water and an accurate measurement scale is all that was needed to make accurate readings of the surface tension. Depending on the accuracy of the measurements, the value for surface tension can be found within 1 to 5% of the actual value.

- Apparatus and Procedure

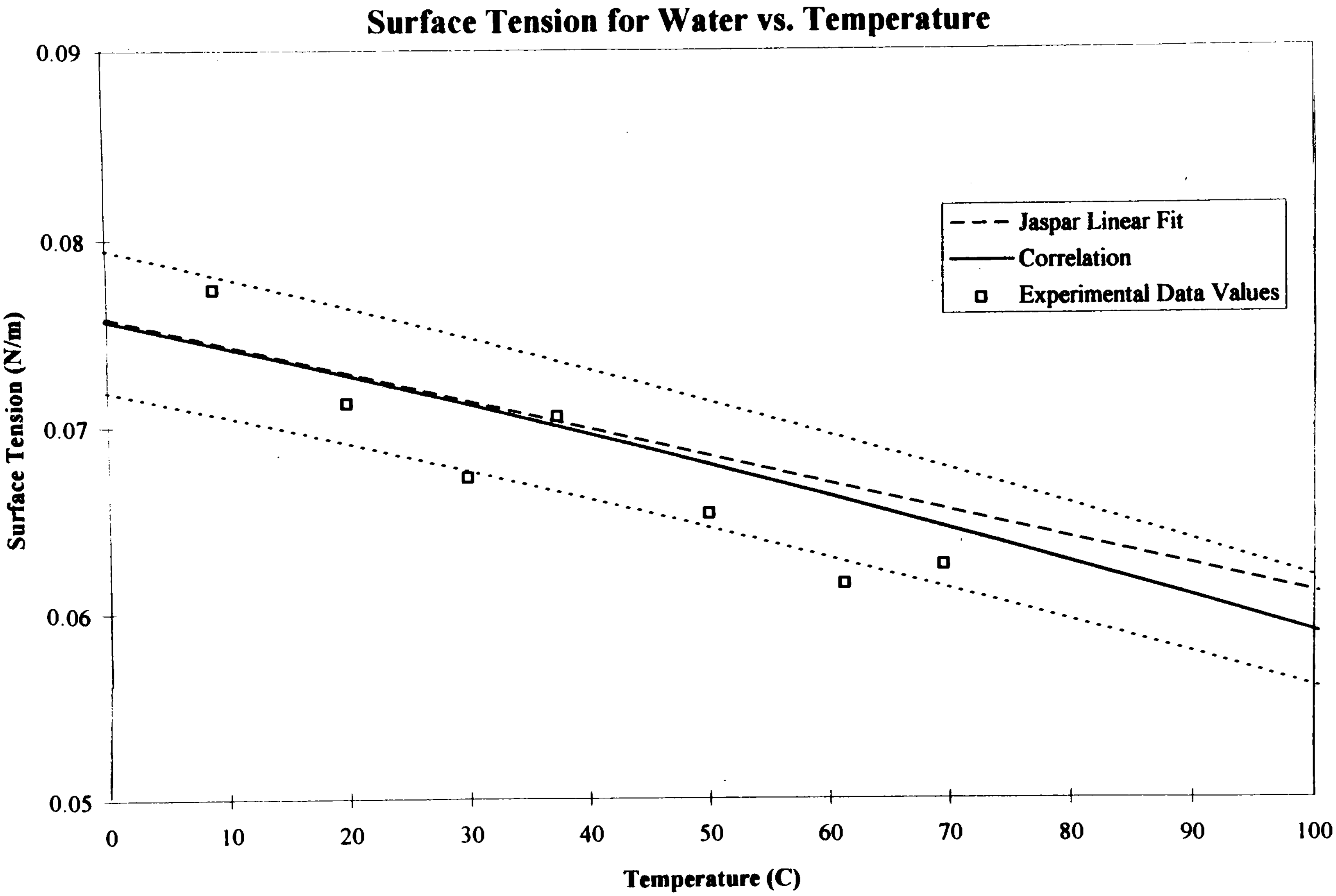

Figure A.1 Surface Tension Experimental Data Results

Appendix B

Example Spread-sheet of Bubble Nucleation Heater Model Resistor Values

Velocity 10%, Water Temperature 80 C

Resistor (series)	Value (K/W)	k (W/mK)	h (W/m^2K)	r2 (m)	r1 (m)	L (m)	Desription
R10	0.3202	135	0	0	0.0047	0.00300	Conduction (vertical) within heater (Section D)
R20	0.3122	135	0	0	0.0047	0.00293	Conduction (vertical) within heater (Section D-C)
R30	0.3042	135	0	0	0.0047	0.00285	Conduction (vertical) within heater (Section C)
R40	0.2743	135	0	0	0.0047	0.00257	Conduction (vertical) within heater (Section C-B)
R50	0.2444	135	0	0	0.0047	0.00229	Conduction (vertical) within heater (Section B)
R60	0.2039	135	0	0	0.0047	0.00191	Conduction (vertical) within heater (Section B-A)
R70	0.1633	135	0	0	0.0047	0.00153	Conduction (vertical) within heater (Section A)
R80	7.3896	0	1950	0	0.0047	0.00000	Convection from heater to water
R90	5643.7923	0	2	0	0.00470	0.00300	Convection (radial) from heater to air (Section D)
R100	3960.5560	0	3	0	0.00470	0.00285	Convection (radial) from heater to air (Section C)
R110	4929.0763	0	3	0	0.00470	0.00229	Convection (radial) from heater to air (Section B)
R120	297.65	0.24	0	0.00934	0.00470	0.00153	Conduction (radial) within Torlon (Section A)
R130	0.9432	0	1950	0.01397	0.00470	0.00000	Convection from Torlon to water
R140	272.63	0.240	0	0.02540	0.00787	0.00285	Conduction (radial) within Torlon (Section C)
R150	166.18	0.240	0	0.01397	0.00787	0.00229	Conduction (radial) within Torlon (Section B)
R160	11.72	0.240	0	0.01397	0.00470	0.00153	Conduction (vertical) within Torlon (Section A)
R170	174.50	0.240	0	0.01397	0.00934	0.00153	Conduction (radial) within Torlon (Section A)
R180	281.70	0.060	0	0.03493	0.02540	0.00300	Conduction (radial) within insulation (Section D)
R190	296.53	0.060	0	0.03493	0.02540	0.00285	Conduction (radial) within insulation (Section C)
R200	0.4136	154	0	0.03493	0.01397	0.00229	Conduction (radial) within Aluminum (Section B)
R210	0.6190	154	0	0.03493	0.01397	0.00153	Conduction (radial) within Aluminum (Section A)
R220	19.9842	0	15	0.00000	0.03493	0.01520	Convection (radial) from insulation to air(sur) (Section D)
R230	106.582	0	15	0.00000	0.03493	0.00285	Convection (radial) from insulation to air(sur) (Section C)

APPENDIX C

Temperature Distributions
Actual Data vs. ThermoNet Model

Velocity	10%
Temperature	80C

	Position UP Along Heater (mm)	**Actual Data (C)**	**T-Net (C)**	**%-Diff.**
T7	0.00	145.20	145.20	[redacted]
T8	15.20	132.30	132.43	[redacted]
T9	30.40	119.50	119.52	[redacted]
T10	40.60	110.90	110.90	[redacted]
Tsurf *	45.20	108.27	107.24	[redacted]

* ——▶ Tsurf for "Actual" is a predicted value from the original 9-node T-Net model. Therefore, the new T-Net value is more accurate.

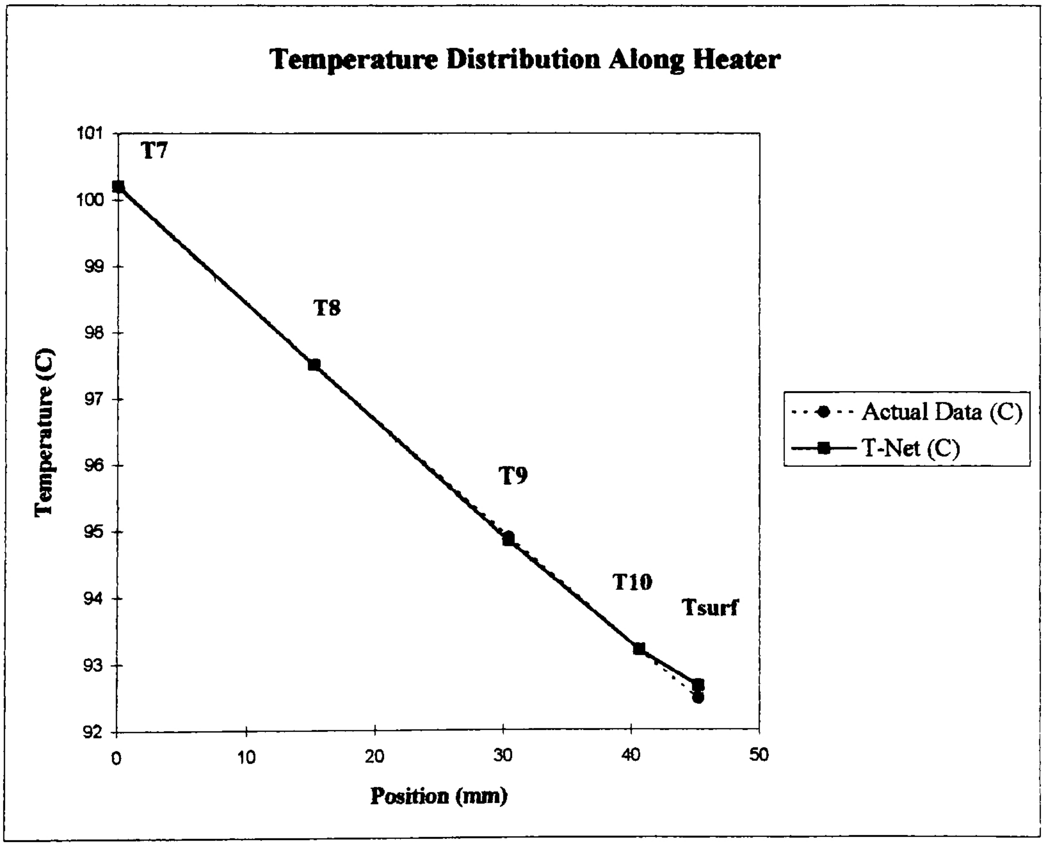

Temperature Distribution

Actual Data vs. Thermonet Model

Velocity	40%
Temperature	60

	Position UP Along Heater (mm)	Actual Data (C)	T-Net (C)	Difference
T7	0.00	252.40	252.40	[redacted]
T8	15.20	205.10	204.73	[redacted]
T9	30.40	156.30	156.18	[redacted]
T10	40.60	123.50	123.50	[redacted]
Tsurf *	45.20	110.52	109.35	[redacted]

* → Tsurf for "Actual" is a predicted value from the original 9-node T-Net model. Therefore, the new T-Net value is more accurate.

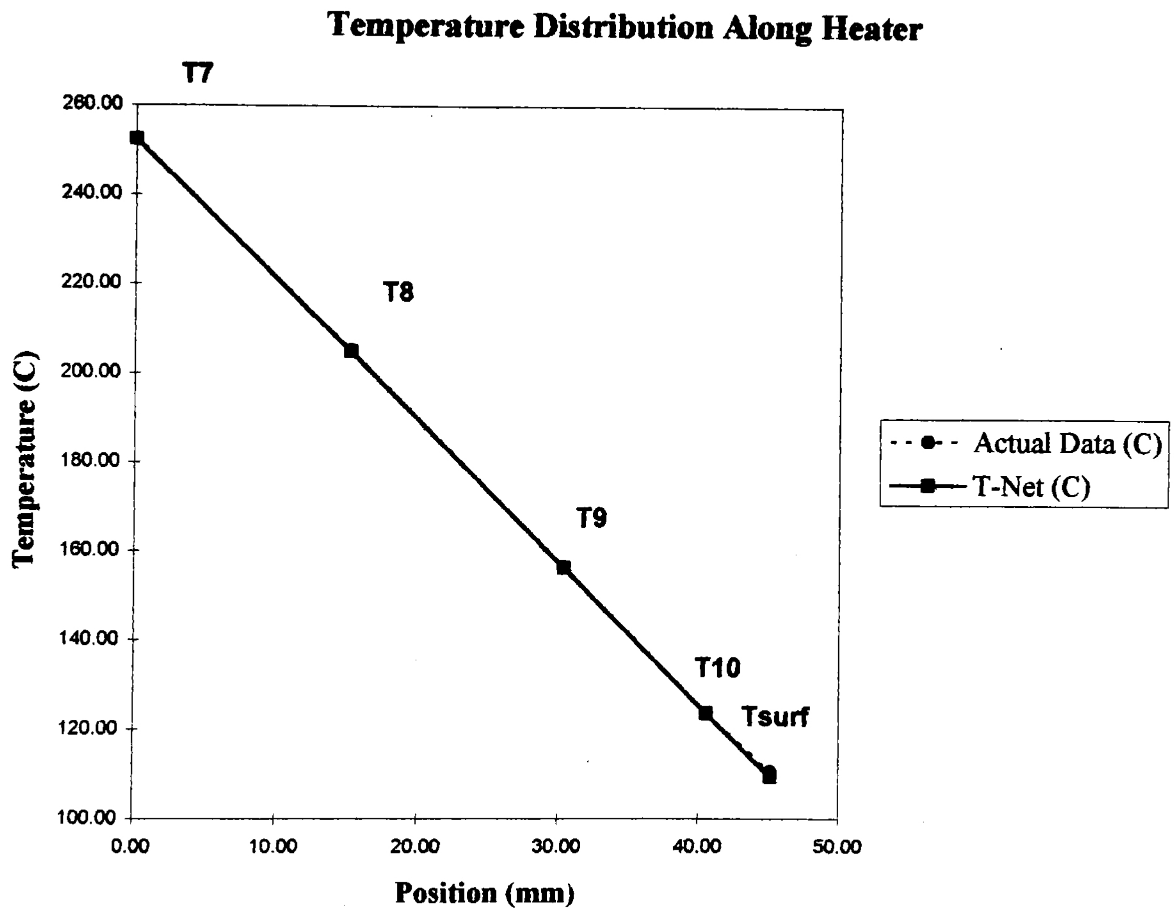

Figure C.2

Appendix D

Experiment Data Sheet #

Date:

Velocity:

Water Temperature:

Voltage (V):							
Current (A):							
T7 (°C)							
T8 (°C)							
T9 (°C)							
T10 (°C)							
Tsurf (°C)							
Heat Flux (W)							
Magnification:							
Departure Diameter:							
Cavity Diameter (in):							
Tape Location:							

Appendix E

% Flow = 28
Re = 3548
Mag. = 140

Diam, measure	Rad (microns)	Beta
22	62.4	40
24	68.0	39
21	59.5	43
22	62.4	42
25	70.9	44

% Flow = 38
Re = 4815
Mag. = 140

Diam, measure	Rad (microns)	Beta
18	51.0	52
19	53.9	50
19	53.9	51
22	62.4	50
14	39.7	48

% Flow = 30
Re = 3801
Mag. = 140

Diam, measure	Rad (microns	Beta
40	113.4	43
32	90.7	43
14	39.7	45
17	48.2	41
23	65.2	41
26	73.7	40
25	70.9	40
32	90.7	39
38	107.7	42
17	48.2	45
20	56.7	43
38	107.7	41
28	79.4	43
23	65.2	40
30	85.0	44
30	85.0	40
54	153.1	46
18	51.0	41
40	113.4	43

% Flow = 34
Re = 4308
Mag. = 140

Diam, measure	Rad (microns)	Beta
25	70.9	48
12	34.0	45
27	76.5	46
18	51.0	44
13	36.9	45
24	68.0	41
22	62.4	42
36	102.1	44
29	82.2	46
32	90.7	46
12	34.0	42
11	31.2	44
19	53.9	43
24	68.0	43

β avgerage	Re
40.4	2027
41.0	2534
41.6	3548
42.1	3801
44.2	4308
50.2	4815

% Flow = 16
Re = 2027
Mag. = 70

Diam, measure	Rad (microns)	Beta
23	130.4	39
19	107.7	39
32	181.4	43
10	56.7	41
9	51.0	42
20	113.4	43
10	56.7	39
21	119.1	40
30	170.1	39
31	175.8	40
17	96.4	39

% Flow = 20
Re = 2534
Mag. = 70

Diam, measure	Rad (microns)	Beta
31	175.8	44
32	181.4	41
30	170.1	41
32	181.4	40
14	79.4	42
17	96.4	39
23	130.4	41
21	119.1	41
22	124.7	39
29	164.4	42